Title
Laser sintering and ablation process for flexible transparent conducting electrodes

Author
Paeng, Dongwoo

Publication Date
2016

Peer reviewed|Thesis/dissertation

Laser sintering and ablation process for flexible transparent conducting electrodes

By
Dongwoo Paeng

A dissertation submitted in partial satisfaction of the
requirements for the degree of
Doctor of Philosophy
in
Engineering – Mechanical Engineering
in the
Graduate Division
of the
University of California, Berkeley

Committee in charge:

Professor Costas P. Grigoropoulos, Chair
Professor Liwei Lin
Professor Junqiao Wu

Fall 2016

Laser sintering and ablation process for flexible transparent conducting electrodes

By
Dongwoo Paeng

Abstract
Laser sintering and ablation process for flexible transparent conducting electrodes

by
Dongwoo Paeng
Doctor of Philosophy in Engineering - Mechanical Engineering
University of California, Berkeley
Professor Costas P. Grigoropoulos, Chair

Recently, flexible electronics have received the attention of many researchers. Among the various fascinating and actively investigated applications of flexible electronics, flexible optoelectronics, such as touchscreen panels (TSPs), organic light-emitting diodes, and organic thin-film transistors, is one of the most aggressively developing research fields. Flexible optoelectronics are often connected by flexible transparent conducting electrodes (FTCEs). FTCEs are considered indispensable components in optoelectronic devices. Researchers are looking for novel materials and processes that enable high transparency and low resistance. Indium tin oxide is the material most widely used in creating FTCEs, as it offers good optoelectronic performance (transmittance (T): > 80%; sheet resistance (R_s): ≈ 15 Ω sq^{-1}) for flexible electronics. However, due to its several intrinsic drawbacks, including its brittleness, high cost of materials, slow rate of deposition, and large amounts of material waste, many researchers are investigating alternative materials and processes.

In this regard, the laser sintering of metals or metal oxide nanoparticles and the patterning of ultra-thin metal film by pulsed laser ablation have attracted much attention due to the characteristics of nanoparticles and ultra-thin film as well as the low-cost facile fabrication capabilities of lasers. Nanoparticles have two distinct thermal and optical characteristics that make them suitable for flexible electronics applications: melting temperature depression and surface plasmon resonance. Furthermore, since lasers offer a facile way of confining optical energy in spatial and time domains, the direct delivery of this confined optical energy into the target materials is a powerful and promising mean of realizing high-performance FTCEs. However, accurate control of the light-matter interactions based on thorough understanding of their optical and thermal properties plays a pivotal role for the successful fabrication of FTCEs using lasers.

First, based on fundamental studies of the thermal and optical properties of silver nanoparticles, I investigated the effect of the wavelength of the laser on the electrical properties and surface morphology of laser-sintered nanoparticle thin films. Scanning electron microscopy images and *ex-situ* resistivity measurements show that photo-thermal sintering significantly alters the surface morphology and electrical properties of the film depending on the processing parameters (i.e., laser wavelength, laser intensity, and scanning speed). The examination of the optical and thermal properties of the thin film of as-deposited silver nanoparticles, in conjunction with the scanning electron microscopy images taken from the laser-sintered lines, enables elucidation on how the wavelength of the processing laser modulates the optical response of the thin film of silver nanoparticles (and, therefore, how it affects the thermal response). Further, *in-situ* optical probing was performed to analyze and compare the characteristic coalescence timescales of silver nanoparticles.

Second, I synthesized a nickel oxide (NiO) nanoparticles as a cheap substitute for silver nanoparticles and demonstrated successful laser reductive sintering of this system. High-resolution nickel (Ni) patterns were generated from NiO nanoparticle thin films by continuous-wave (CW) laser irradiation. By the laser reductive sintering of NiO nanoparticles, I developed a high-transmittance (> 87%), electrically conductive panel for TSPs that is very robust to mechanical bending and adhesion. Furthermore, the mechanisms of photophysical reductive sintering upon the irradiation of a CW laser on NiO nanoparticle thin films were studied by modulating the power density and illumination time of the laser. Protons produced due to the high-temperature decomposition of the solvent present in the NiO nanoparticle ink, oxygen vacancies in the NiO nanoparticles, and electronic excitation by laser irradiation in the NiO nanoparticles all affect the early stages of the reductive sintering process. Once NiO nanoparticles are reduced to Ni by laser irradiation, they begin to coalesce, forming a conductive material. *In-situ* optical and electrical measurements were taken during the reductive sintering process to monitor the transient evolution of the process.

Finally, low-cost Cu FTCEs were fabricated using 532 nm nanosecond laser ablation under ambient conditions. The fabricated Cu FTCEs have excellent optoelectronic characteristics (T: 83%; R_s = 17.48 Ω sq^{-1}) and mechanical durability. The potential application of Cu FTCEs in flexible optoelectronic devices was successfully demonstrated by the fabrication of TSPs using Cu FTCEs. Furthermore, we employed diffractive optics for laser beam shaping. We successfully demonstrated the optoelectrical characteristics of the percolative regime by decreasing the areal density. Time-resolved imaging using nanosecond-laser irradiation showed transient dewetting and ablation dynamics with three different thicknesses of the thin film of silver nanoparticles.

Thus, these various outcomes from my studies and experiments on the fabrication of FTCEs using lasers open opportunities for the fabrication of optoelectronic devices with flexible platforms.

The surpassing worth of knowing Christ Jesus my Lord
- Philippians 3:8

ACKNOWLEDGEMENTS

First of all, thank you God for always being with me and giving me the strength to finish this 4-years of journey.

I cannot express enough thanks to my research advisor, Professor Costas P. Grigoropoulos for his trust, sound discussion. Without him, I could not have started and completed my Ph.D. degree. His guidance helped me in all the time of research and writing of this dissertation. Professor Liwei Lin in department of mechanical engineering and professor Junqiao Wu in department of materials science and engineering at UC Berkeley are both dissertation committees. They always encouraged me with warm and kind words, and I appreciate their valuable advice on this dissertation.

I also thank all the previous and current colleagues at UC Berkeley: Dr. Daeho Lee, Dr. Eunpa Kim, Dr. Jae-hyuck Yoo, Dr. Junyeob Yeo, Dr. Sukjoon Hong, Dr. Hyuk-jun Kwon, Dr. Sangmo Koo, Dongfeng Qi, Letian Wang, Yoonsoo Rho and Meng Shi.

I deeply thank Youngkwon Paeng, Yeonok Kwon, Changbae Park and Sunboon Lee who are my parents and parents-in-law, giving birth, characteristics, and capabilities to me. That is originally how I can be here, and their support in my entire life was priceless. I deeply appreciate Youmi Park who is a talented mom, and I could concentrate on my research owing to her assist. My lovely two sons, Jiho and Harry, are an infinite source of my positive energy. All my family members have always been a big part of my life. I dedicate this dissertation to them.

Finally, I appreciate my brothers in the Gracepoint fellowship church for walking together with me and for encouraging me to stay always in the light.

Table of Contents

LIST OF FIGURES

LIST OF TABLES

LIST OF EQUATIONS

Chapter 1. Introduction

Recently, there has been great interest in fabricating flexible electronics. And lots of materials are tested for this purpose. In addition, various nanomorphologies have been developed, including nanowires, nanoflowers, nanobelts, nanowalls, and nanoparticles of materials.[1-7] These efforts aim to enhance device performance by designing properties that fully exploit the size effect. In particular, nanoparticles are widely used due to easy handling, controlled deposition, and the high-resolution patterning attainable under ambient conditions when combined with various reduction and/or sintering techniques.[8-12] For these reasons, several studies have utilized metal or metal oxide nanoparticles to fabricate semiconducting or conducting electrodes.[13-17] A nanoparticle is defined as a particle of gel of any shape with an equivalent diameter of approximately 1 to 100 nm, as shown in **Figure 1.1**. Nanoparticles have two interesting characteristics due to their augmented surface to volume ratio: Thermodynamic size effect and surface plasmon resonance(SPR).

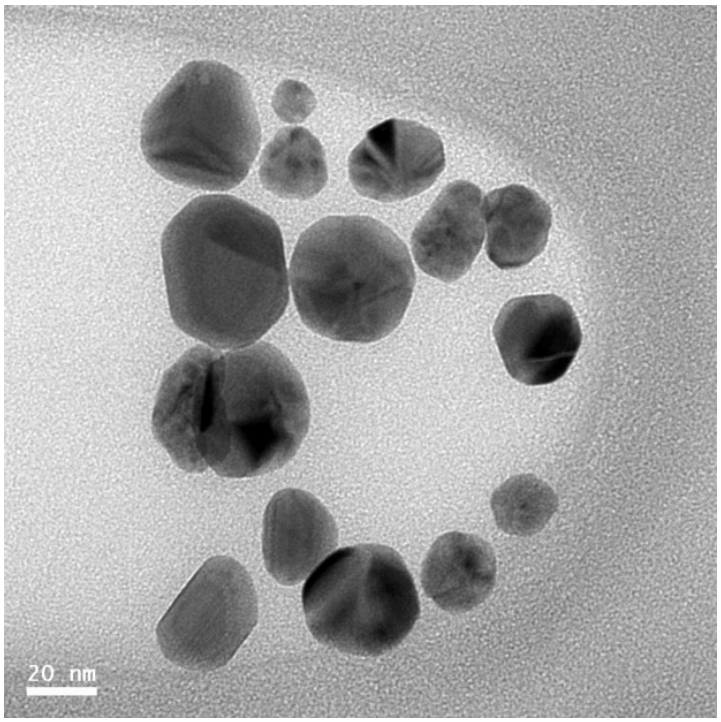

Figure 1.2 TEM image of silver nanoparticle synthesized by the polyol process

When the physical size of the material approaches to the nanoscale, many physical properties, such as thermal and optical properties, change rapidly. The property that makes nanoparticle a promising material in optoelectronics applications is their melting temperature depression, which is also often called as the thermodynamic size effect.[18] As the dimensions of a material decrease towards the atomic scale, the melting temperature is depressed. A change in the melting temperature also occurs due to the augmented surface to volume ratio compared to the bulk

material. For example, 2–3-nm gold nanoparticles begin to melt around 130–140 °C. When compared to the melting temperature of bulk gold (1,063 °C), the melting temperature is much lower, and its range is compatible with the glass transition temperature of plastic substrates.

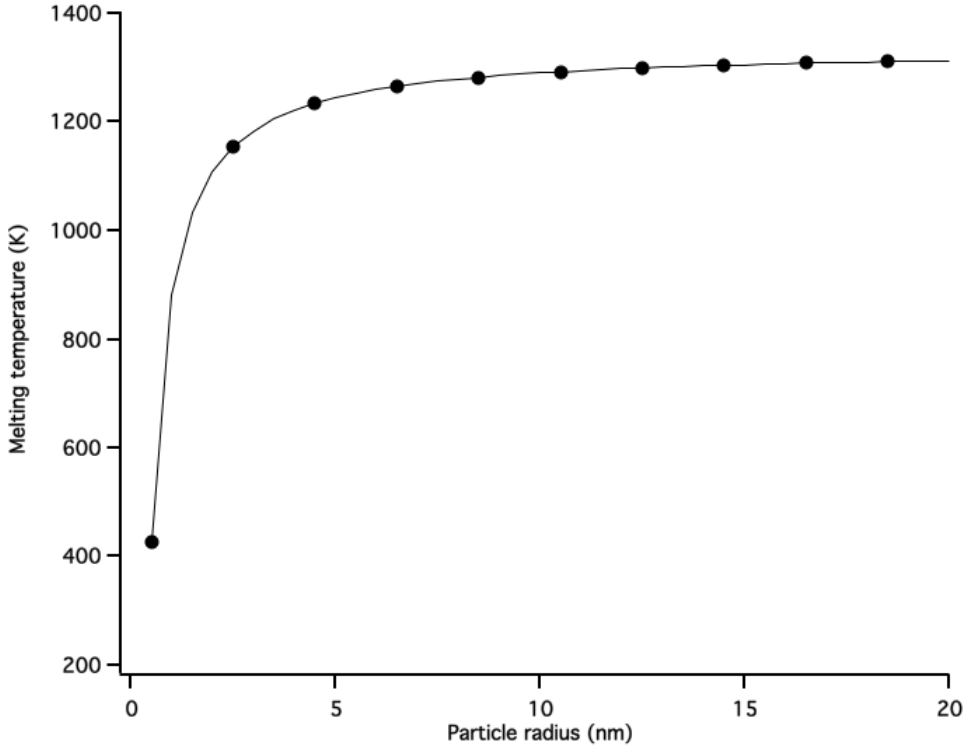

Figure 1.2 Simulated melting temperature depression of gold nanoparticle

Melting can be defined and observed in three ways; 1) The disappearance of the state of order in the solid. 2) The sharp variation of evaporation rate. 3) The sudden change in the particle shape. *Buffat et al*. experimentally observed the thermodynamic size effect (Melting temperature depression) of nanoparticle.[18] The thermodynamic relationship between the particle radius and the melting temperature using the Gibbs–Duhem relationship (-VdP + SdT + mdμ = 0, where V, P, S, T, m, and μ represent volume, pressure, entropy, temperature, mass, and chemical potential, respectively). For the first approximation, the normalized melting temperature can be expressed as follows,[18]

Equation 1.1 Thermodynamic size effect

$$1-\Theta=\frac{2}{L\rho_s r_s}\left[r_s-r_l\left(\frac{\rho_s}{\rho_l}\right)^{2/3}\right]$$

where Θ, L, ρ_s, ρ_l, r_s, r_l represent the normalized temperature with respect to the melting temperature of the bulk material, latent heat of fusion, density of solid material, density of liquid, and radius of solid and radius of liquid that has equivalent mass with solid, respectively. The results of the simulation are shown in **Figure 1.2**.

When electromagnetic (EM) waves are incident on the bulk material, the incident EM wave experiences three different phenomena, as shown in **Figure 1.3**: reflection, propagation, and transmission. However, for the material with dimensions much smaller than the wavelength of the EM wave, especially when the material is a metal with a high density of free electrons, free electrons collectively oscillate by the propagation of the electric field through the material; then, they dissipate the energy of the EM wave by the electron-electron or electron-phonon collisional process, as depicted in **Figure 1.3**. This process is called SPR. SPR is strongly dependent on the wavelength of EM waves. Metallic nanoparticles, which usually have smaller diameters than the wavelength of visible light, show strong SPR. Therefore, by choosing the appropriate processing laser wavelength, where maximum absorption happens, we can effectively deposit optical energy to the metallic nanoparticle thin film, which will then turn into thermal energy through EM wave absorption. Thus, it is essential to study the optical properties of nanoparticles; their importance will be discussed further in **Chapter 2**.

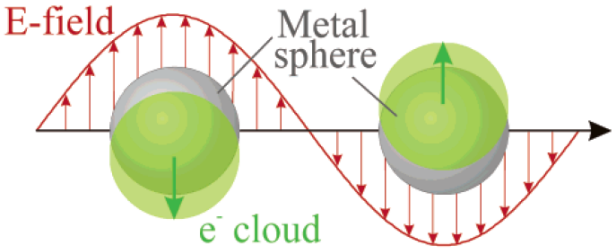

Figure 1.3 Schematics of surface plasmon resonance (image from *Kelly et al.*[19])

The printing or coating of nanoparticles following low-temperature thermal treatment has been shown to have substantial promise in low-cost electronic fabrication. The general fabrication process of laser sintering for flexible electronics is shown in **Figure 1.4**.[20] On the plastic substrate, we deposited the metallic nanoparticle through various deposition techniques, such as inkjet printing, spin coating, slot die coating, etc., and then we applied the laser to selectively sinter the nanoparticle. Finally, we washed the unsintered section. According to Yeo et al.,[20] employing laser irradiation to selectively sinter nanoparticles and to define micron and sub-micron features has demonstrated advantages in terms of meeting both performance and cost requirements.

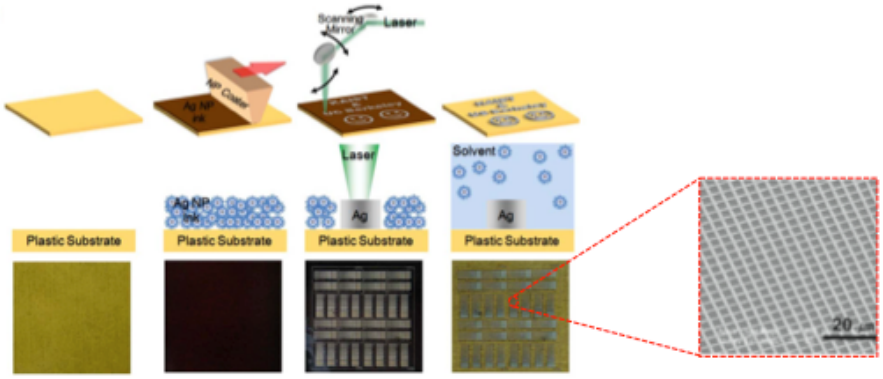

Figure 1.4 Schematics of laser sintering of silver nanoparticle process(image from *Yeo et al.*[20] and inset picture(red dashed box) is from *Son et al.*[21])

Chapter 2. Silver nanoparticle sintering with CW laser

2.1 Overview

To meet the increasing demand for the large area and low-cost fabrication of FTCEs, many researchers have focused on photolithography-free, non-vacuum and solution-processable routes. Screen-printing,[22, 23] inkjet printing[24-26] and nanoimprinting[27, 28] are commonly employed methods for this purpose. Utilizing nanomaterials, low-temperature thermal treatment compatible to flexible substrates can be achieved by taking advantage of the significant melting temperature depression due to the thermodynamic size effect.[18] Laser sintering of deposited functional nanoparticle (NP) ink is a promising method since it enables the writing of micron and even sub-micron conductive patterns. Recently, *Lee et al.* fabricated high-resolution nickel (Ni) patterns from the laser induced reductive sintering of nickel oxide (NiO) NPs and could demonstrate a touch screen panel (TSP) for display application.[17] Furthermore, approximately 400 nm-thick metal patterns were written by the femtosecond laser sintering of silver (Ag) NP thin films by limiting the heat diffusion through the Ag NP thin films.[21] Laser-induced photo-thermal sintering of metal nanoparticles requires control of the interaction between the laser beam and the nanoparticle material. Furthermore, understanding the optical and thermal properties of the NPs is crucial for determining the mechanism of electrical property change after laser sintering. Optical properties of NP thin films have been utilized to investigate the evolution of the sintering process. Characteristic time scales of coalescence of Ag NPs by 514.5 nm Ar-ion continuous wave (CW) laser irradiation were investigated by probing the surface plasmon resonance (SPR) peak change during sintering.

Furthermore, the resistivity change of Cu NP thin films upon laser irradiation was correlated with the spectral reflectivity change.[15] Recent studies focused on the complex mechanisms of the laser-induced reductive sintering of ultra-small NiO NPs. However, not much attention has been given to the effect of the wavelength of the processing laser on the electrical properties and morphology changes upon laser sintering. Clearly, the spectral variation of the Ag NP thin film optical properties that is strongly influenced by the SPR must be accounted for. *Katsuhiro et al.* qualitatively discussed the wavelength effect on Ag NP ink using 4 different lasers (Nd: YAG laser: 1064 nm, Laser diode (LD): 980 nm, green laser: 532 nm, Ar-ion laser: 488 nm).[29] I studied the laser wavelength effect on the electrical properties and surface morphology changes of laser-sintered silver nanoparticle thin films. Thermogravimetric analysis (TGA) and differential scanning calorimetry (DSC) were performed to evaluate the sintering temperature of Ag NP inks. The Maxwell-Garnett effective medium theory was also applied to approximate the thermal conductivity of Ag NP thin films. The spectral complex dielectric function, reflectivity and absorption coefficient of pristine and sintered Ag NP thin films were obtained by spectroscopic ellipsometry. Three lasers at different wavelengths (near ultraviolet (NUV): 405 nm, green: 514.5 nm, near infrared (NIR): 817 nm) were irradiated on the Ag NP thin films at varying intensities and scanning speeds. *Ex-situ* resistivity measurements and scanning electron microscopy (SEM) images combined with thermal analysis based on the optical penetration depths of the different wavelength lasers were carried out to explain deviations in the resistivity measurements and surface morphologies.

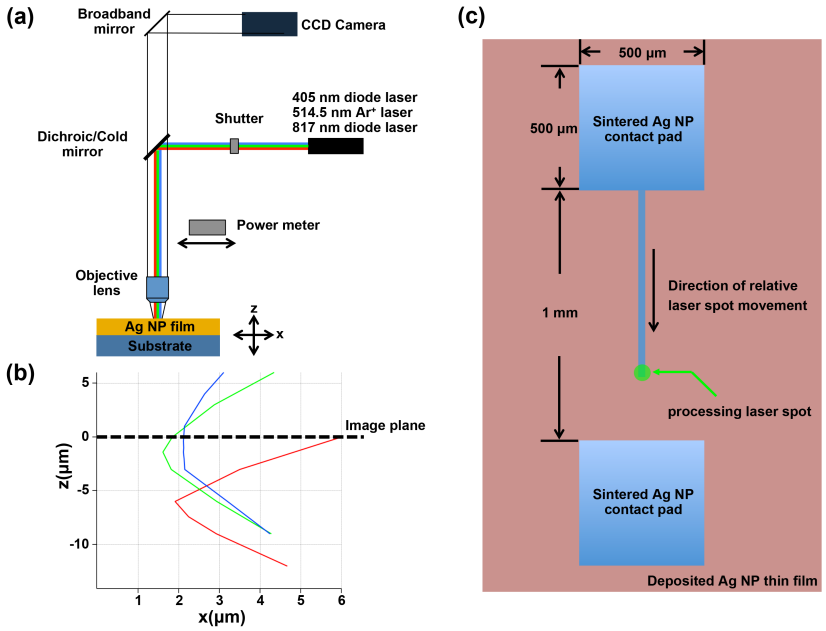

Figure 2.1 (a) Experimetal set-up for the laser sintering experiment. Three different wavelengths of 405 nm, 514.5 nm and 817 nm. Laser with 817 nm wavelength is reflected by the cold mirror. (b) Beam configuration from the knife-edge method for the laser with three different wavelengths. (c) Schematics of patterns for the resistivity measurement.

This study used commercially available Ag NP inks (NPS-JL, Harima Chemicals, Inc., 5 ~ 12 nm in diameter, 7 nm mean diameter, specific gravity: 1.4 ~ 1.8, metal contents: 52 ~ 57 wt. %) without further purification. 1 mm-thick soda lime glass was used as the substrate. This substrate was cleaned sequentially with acetone, ethanol and DI water before the spin coating of the Ag NP inks to remove residual organics and contaminations. After oxygen-plasma treatment to enhance the adhesion, uniform Ag NP thin films of 170 nm thickness were deposited by spin coating Ag NP inks at 2000 rpm for 15 min. The spin coated Ag NP thin film was placed on a computer-controlled *x*, *y*, *z* stage.

Lasers of three different wavelengths from NUV to NIR (NUV: 405 nm diode laser, green: 514.5 nm Ar-ion laser, NIR: 817 nm diode laser) were employed in this study. **Figure 2.1(a)** shows the configuration of the optical apparatus and the beam path. The laser beams were focused at normal incidence onto the sample by a single 20× infinity corrected, long working distance objective lens of 0.42 numerical aperture (N.A.). The focal length through the lens varied with respect to the transmitted laser beam wavelength due to the spectral dependence of the lens material refractive index. Thus, to accurately position the samples on the focal plane, beam diameter measurement with the knife-edge method was also performed as shown in **Figure. 2.1(b)**. **Figure 2.1(c)** illustrates the schematics of patterns for the *ex-situ* resistivity measurements. For this purpose, 500 × 500 μm^2 contact pads were first patterned by laser sintering the Ag NP thin films. The distance between the pads was fixed at 1 mm. Single lines were patterned using different laser intensities and scanning speed (2, 5, 10, 20, 40 mm/s) in order to measure the resistivity. All patterns were cleaned with tetradecane ($(CH_3(CH_2)_{12}CH_3)$) after laser sintering to remove residuals and un-sintered Ag NP ink. SEM images were taken to measure accurately the line width and record the surface morphology. Confocal microscopy was

employed to measure the thickness. The resistance was measured with a semiconductor analyzer. Based on these data, the resistivity, ρ, was calculated using the **equation**, $\rho=R\times w\times t/l$, where R, w, t and l_t are the resistance, width, thickness and length of the single line electrode, respectively.

2.2 Thermal properties

Since laser sintering is a photo-thermal process, it is important to understand the thermal and optical properties of the Ag NP ink. **Figure 2.2(a)-(b)** shows the TGA and DSC measurement data. TGA measurement was conducted on a TA Instruments Q50 thermal analysis station under 20% O_2/Ar atmosphere. DSC measurement was performed on a Mettler Toledo DSC1 under N_2 atmosphere. Samples were heated up from 30 to 500 °C at a ramp rate of 10 °C/min for TGA and 2 °C/min for DSC. The nearly 50 % initial weight loss upon heating is ascribed to the evaporation of solvent and ligand removal, which is consistent with the wt.% of metal contents in the Ag NP inks.[20, 30, 31] The data yield the onset temperature of ligand loss, which is defined as the temperature at which the derivative of weight % (blue traces with triangle markers in **Figure 2.2(a)** signals the initial change in rate, due to ligand volatilization. The rate of weight % loss starts to increase rapidly around 88 °C, where the change rate of weight % is over 0.1 %/°C, which is consistent with the broad endothermic peak in the DSC data, which corresponds to the disordering or melting of the ligands that encompass the Ag NP.[32, 33] The strong and sharp endothermic response shown in DSC data at 129.89 °C is attributed to the sintering of Ag NP. Sintering of Ag NP begins at this temperature, followed by rapid weight loss due to ligand and solvent volatilization.[34]

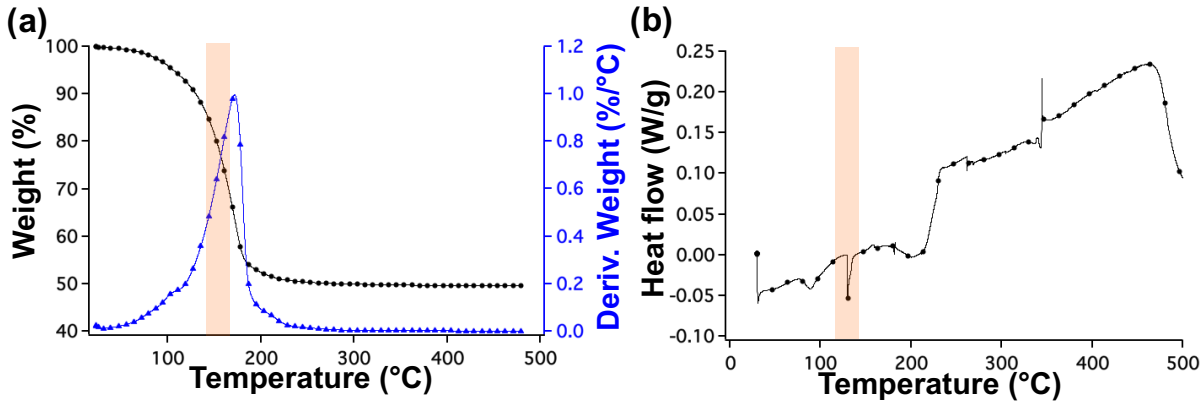

Figure 2.2 (a)TGA and (b) DSC data of Ag NP ink.

Another important property that has to be considered for the thermal analysis is the thermal conductivity of Ag NP thin films. Many researchers have investigated the modeling and experimental validation of effective thermal conductivities of metal nanoparticle suspensions.[35-37] The Maxwell-Garnett effective medium approximation (M-G EMA) considering the Kapitza resistance (interfacial thermal resistance) has been widely adopted for this purpose.[38, 39] For spherical-shaped nanoparticulate composites with interfacial thermal resistance, the following

equation was suggested,

Equation 2.1 Effective thermal conductivity including Kapitza resistance using MG-EMA

$$k_{eff} = k_m \frac{k_p(1+2R_k k_m / r_p) + 2k_m + 2\phi[k_p(1-R_k k_m / r_p) - k_m]}{k_p(1+2R_k k_m / r_p) + 2k_m - \phi[k_p(1-R_k k_m / r_p) - k_m]}$$

where k_{eff}, k_m, k_p, R_k, r_p, f represent the effective thermal conductivity of Ag NP ink to be calculated, the thermal conductivity of solvent (Tetradecane ($CH_3(CH_2)_{12}CH_3$): 0.14 W/(m•K)), the thermal conductivity of bulk silver (429 W/(m•K)), Kapitza resistance (10^{-7} ~ 10^{-8} m^2•K/W for the metal nanoparticle),[40] the radius of the particle (3.5 nm), and the volume fraction of particle (0.6 ~ 0.8), respectively. The calculated effective thermal conductivity of the pristine Ag NP inks, k_{eff}, is 0.1 ~ 0.17 W/(m•K), which is comparable to the thermal conductivity values from other references. However, during the laser irradiation on the Ag NP thin film, the thermal conductivity rapidly increases as the coalescence of the Ag NP starts. Recently, the transient thermal conductivity during the laser irradiation on Ag NP inks was estimated using the Wiedemann-Franz law (W-F law), $k = L \cdot \sigma \cdot T$, which correlates the thermal conductivity with the electrical conductivity, where k, L, σ and T represent the thermal conductivity, Lorenz number for silver (2.37×10^{-8} W•Ω/K^2 @ 100 °C), electrical conductivity and temperature, respectively.[41]

Equation 2.2 Estimated thermal conductivity by Wiedemann-Franz law

$$k = L \cdot \sigma \cdot T$$

By applying the W-F law, estimated thermal conductivities of Ag NP films sintered with the three different wavelengths at room temperature (300 K) were 126 W/(m•K), 136 W/(m•K) and 80 W/(m•K), respectively. **Table 2.1** summarizes the estimated thermal conductivities with electrical conductivities used in the calculation. Thermal diffusivity, $D = k/\rho_d C_p$, taking into account the estimated thermal conductivity and other parameters from bulk silver (density (ρ_d): 10.49×10^3 kg/m^3, specific heat capacity (C_p): 240 J/(kg•K)), can be calculated as 6.75×10^{-8} m^2/s (Bulk silver: 1.66×10^{-4} m^2/s)

Table 2.1 Estimation of thermal conductivities of pristine and sintered Ag NP thin films

	Pristine	NUV laser	Green laser	NIR laser
Electrical conductivity (S/m)	-	1.76×10^7	1.89×10^7	1.12×10^7
Thermal conductivity (W/(m•K))	0.1 ~ 0.17	126	136	80
Sintering condition	-	90 mW	100 mW	70 mW
(Laser power, scanning speed)	-	2 mm/s	2mm/s	2 mm/s
Estimation method	MG EMA		W-F law	

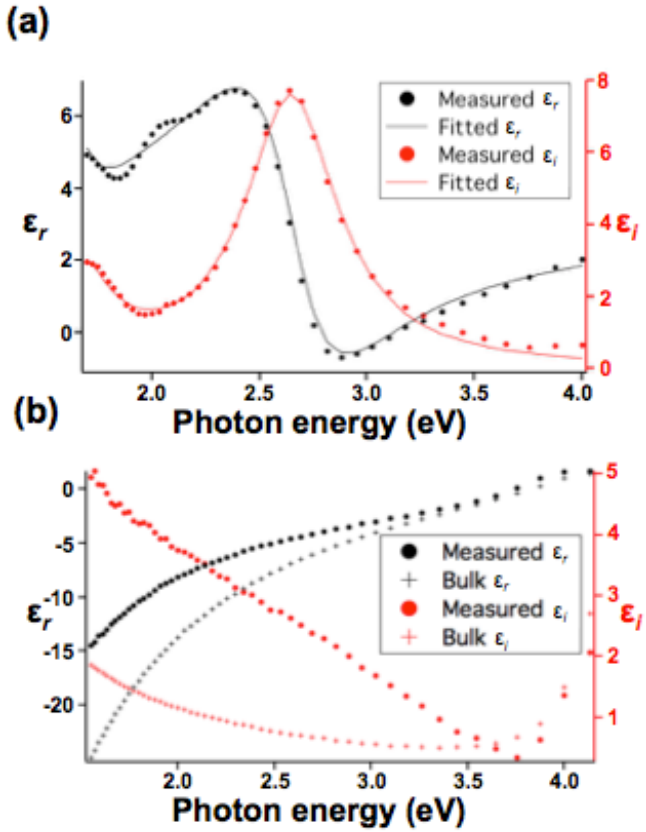

Figure 2.3 Complex dielectric function for the (a) pristine Ag NP thin film and their two Lorentz model fitting results and (b) thermally sintered (150°C for 20 minutes on hot plate) Ag NP film and comparison with those of bulk Ag

2.3 Optical properties

Optical properties of Ag NP thin films were characterized by spectroscopic ellipsometry. **Figure 2.3(a)** shows the real and imaginary parts of the measured dielectric function, $\varepsilon = \varepsilon_r + j\varepsilon_i$, of the pristine Ag NP thin film and their fitting using the two oscillator Lorentz model. For pristine Ag NP thin film, the movement of the free electrons is spatially confined within the nanoparticles, which results in the distinct surface plasmon resonance (SPR) contribution.[19, 42] The two Lorentz oscillator model of the dielectric function is given below:

Equation 2.3 two Lorentz oscillator model

$$\varepsilon(E) = \varepsilon_\infty + \sum_{n=1}^{2} \frac{A_n}{E_n^2 - E^2 - j\Gamma_n E}$$

where ε_∞, A_n, E_n and Γ_n are the dielectric function at large photon energies, amplitudes, resonance energies and broadenings, correspondingly. **Table 2.2** summarizes the fitting parameters.

Table 2.2 Fitting results for the two Lorentz oscillator model

(Unit: eV)	Oscillator 1	Oscillator 2
A_n	3.26	1.25
E_n	2.66	1.67
Γ_n	0.53	0.36

Lorentz oscillator 1 originates from the SPR of silver nanoparticles and is located at 2.66 eV. Oscillator 2, which is located at 1.67 eV and has lower amplitude than that of oscillator 1, represents the plasmon resonance due to the particle interaction.[43, 44] **Figure 2.3(b)** shows the real and complex parts of the measured dielectric function of the sintered Ag NP thin film. The as-deposited Ag NP thin film is thermally sintered at 150 °C for 20 minutes on a hot plate. The thermal sintering temperature of 150 °C was chosen since we observed that the sintering starts around ~ 130 °C from DSC data. The Lorentz oscillator influence disappears, establishing bulk-like optical response of silver with clear optical interband transitions of d-band electrons above ~ 4eV. It is worth noting that the deviation from the dielectric function of bulk silver is due to the uneven surface morphology and electron scattering at grain boundaries after sintering.[45]

Figure 2.4(a)-(b) shows the reflectivity and absorption coefficient of pristine and sintered Ag NP films. From the measured complex dielectric functions of pristine and sintered Ag NP thin films, complex refractive index, $n + jk$, was calculated based on the following equation,[46]

Equation 2.4 Complex refractive index calculated from complex dielectric function

$$n = \sqrt{\frac{\varepsilon_r + \sqrt{\varepsilon_r^2 + \varepsilon_i^2}}{2}}, k = \sqrt{\frac{-\varepsilon_r + \sqrt{\varepsilon_r^2 + \varepsilon_i^2}}{2}}$$

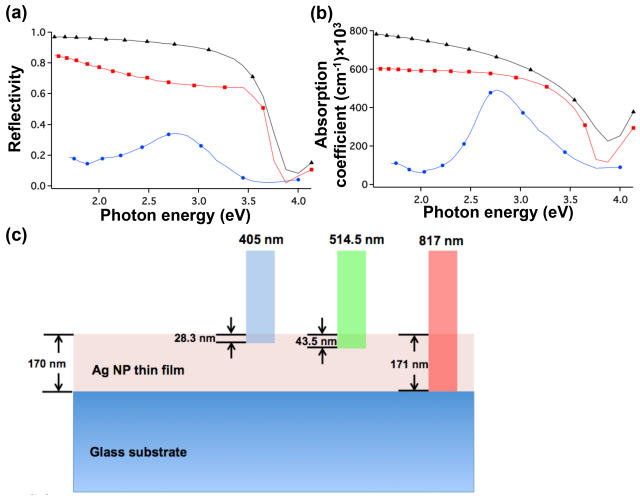

Figure 2.4 (a) Reflectivity and (b) absorption coefficient calculated from the complex dielectric functions (blue circle: Pristine Ag NP thin film, red square: thermally sintered Ag NP thin film, black triangle: bulk Ag). (c) Optical penetration depth at the wavelengths of three processing laser and thickness of the pristine Ag NP thin film.

By applying thin film optics,[47] the reflectivity at normal incidence and the absorption coefficient, $\alpha=4\pi k/\lambda$, were obtained. Both the reflectivity and the absorption coefficient of pristine Ag films show maxima at ~ 2.76 eV (450 nm) due to SPR. As previously mentioned, once sintered, the SPR peak fades away and bulk behavior emerges, although both the reflectivity and absorption coefficient were slightly smaller than the bulk counterparts.

2.4 Processing laser wavelength effect on surface morphologies

Variation of the optical response of the pristine Ag NP thin films causes temperature field deviations, leading to resistivity and surface morphology differences. The quasi-static (i.e. fixed with respect to the laser beam axis) temperature field induced by scanning CW laser irradiation depends on specimen and processing parameters including the scanning speed, v, and optical properties such as reflectivity, $R(\lambda,T)$, and absorption coefficient, $\alpha(\lambda,T)$, that are functions of wavelength, λ, and temperature, T. Even though analytical solutions for the temperature field can be derived using a Green's function method for the solution of the heat conduction equation,[48] they are not particularly useful in the present problem since all optical and thermal parameters, including reflectivity, absorption coefficient, thermal conductivity and thermal diffusivity are functions of temperature and additionally, they drastically change during the sintering process. **Figure 2.4(c)** shows the thin film configuration and l_{opt} for the three different wavelengths. The optical penetration depth of the NUV and the green laser is laser light are 28.3 nm and 43.5 nm, and in both cases much that smaller than the thickness of as-deposited Ag NP thin film, l_t, of ~ 170 nm. In contrast, the optical penetration depth of NIR laser is 171 nm, i.e. nearly the same as the film thickness. In this case, volumetric heat generation across the film due to the absorption of laser light has to be considered. For the NUV and green laser, which have a shallow optical penetration depth (28.3 and 43.5 nm), the top layer is instantaneously heated by direct laser light absorption. Once this top layer is sintered, the reflectivity increases abruptly, and the absorbed laser light energy diminishes. The underlying Ag NPs are then sintered by vertical heat diffusion across the film. On the other hand, for the NIR laser, where the absorption of laser light energy is volumetric (the optical penetration depth of 171 nm is comparable to the thickness of the film), the film is nearly isothermal in the vertical direction. These differences in the heat conduction mechanism and temperature field are responsible for the substantial departures of the surface morphologies after sintering.

2.4.1 Surface morphology

Figure 2.5 shows high magnification SEM images of the center areas of sintered Ag NP lines irradiated with NUV laser with different laser powers (10, 25, 50, 70 and 90 mW) and scanning speeds. Neck formation between the nanoparticles was observed even at the low laser power of 10 mW that suffices to initiate sintering by removing residual solvents and ligands surrounding the nanoparticles.[49] As the laser power increased, the grain size became larger, due to NP coalescence.[50] Surface melting was evident above the laser power of 25 mW. Since l_{opt} is 28.3 nm for the 405 nm laser, which is 17 % of the thickness of the pristine Ag NP thin film and the estimated thermal conductivity of Ag NP ink is around 0.1 ~ 0.17 W/(m K), laser light energy is efficiently absorbed on the surface of the Ag NP thin film and most of the energy is dissipated by transverse and vertical heat conduction. Flake-like ripples are noticed on the sintered Ag NP surface at higher power where surface melting occurs.[51, 52] **Figure 2.6** shows high magnification SEM images of the Ag NP thin film irradiated with green laser at different laser powers (10, 20,

40, 80 and100 mW) and scanning speeds. Unlike the sintering results by NUV laser, no ripple structures were found. Furthermore, surface melting features are observed even at the lower laser power of 10 mW. Large grain solidified structures should have lower resistivity than small grained ones due to diminished electron scattering.[53] It is therefore expected that the resistivity at 10 mW is much lower for the green laser than the NUV laser, which is confirmed by resistivity measurements. As mentioned earlier, once the sintering of the surface layer happened, the underlying layer sintering progressed by vertical heat conduction, albeit driven by reduced laser light absorption, in turn yielding partial sintering of Ag NPs with smaller grains. Through the open pores or cracks on the top surface melting layer, we can observe the smaller grains and partially sintered features of the underlying layer. **Figure 2.7** displays high magnification SEM images of the Ag NP thin film irradiated with NIR laser with different laser powers (10, 20, 35, 50, 70 mW) and scanning speeds. These images revealed quite different surface morphology characteristics compared to the NUV or green laser. Surface melting was not evident even at the higher laser power of 70 mW. It is recalled that surface melting morphologies were observed for NUV and green laser at that laser power. As discussed earlier, l_{opt} at 817 nm is nearly the same as the thickness of the Ag NP thin film. Deviations of the temperature field induced by the NIR laser versus the NUV and green laser are due to the different absorption profile and heat conduction mechanism. The NIR laser light is volumetrically absorbed across the thin film and sinters a narrow vertical column but the absorbed power cannot sustain lateral sintering. In contrast, for the NUV and green laser, light is absorbed on the top surface, sintering a thin layer first. Sintering is then extended by transverse and vertical heat conduction. At the laser power of 10 mW, minimal sintering (neck growth) of densely packed nanoparticles was observed; for the scanning speeds of 20 and 40 mm/s, the written line patterns even detached upon washing. There is no substantial difference in surface morphologies obtained by varying the scanning speed from 2 to 20 mm/s at all laser powers, with the exception of 40 mm/s where the porosity increased for both the NUV and green laser. At higher speeds, the material ahead of the laser spot does not experience significant heating, since the temperature field has an exponential dependence on speed ($T \propto \exp(-vr/D)$), where v is the scanning speed, r the distance from the laser spot center and D the thermal diffusivity. High scanning speed causes slower temperature rise and lower peak temperature.[54] This trend is marked by the characteristic speed, $v^*(v) = vw_O/D$, where w_O is the beam waist. If $v^* >> 1$, the maximum temperature occurs in the wake of the scanning laser beam. For scanning velocities of 40 mm/s, v^* (40 mm/s) = 1.2, while v^*(20 mm/s) = 0.6. Trapped solvent and ligand ahead of the laser spot may not evaporate until the temperature reaches the evaporation/volatilization temperature (the TGA/DSC data, show that ligand loss/volatilization starts around 88 °C). Once it reaches the evaporation/volatilization temperature, explosive removal of trapped solvent and ligands could happen. Thus, it is expected that the delayed temperature rise at the scanning speed of 40 mm/s causes lagged release of trapped solvent and ligands and generation of large pores.

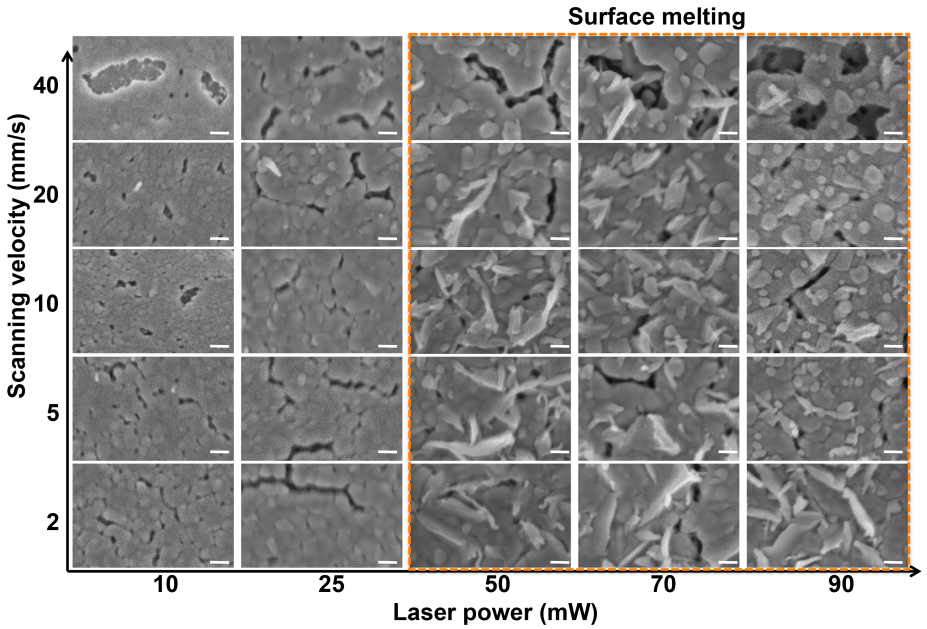

Figure 2.5 High magnification SEM images of sintered Ag NP thin film. Processing laser: 405 nm NUV laser with varying laser power and scanning speed. (Scale bar: 100 nm)

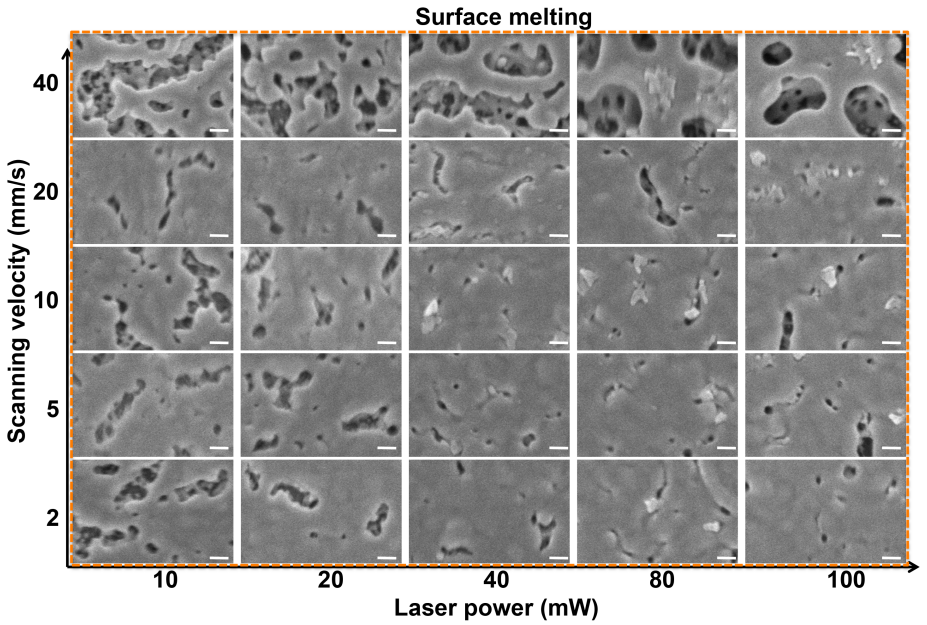

Figure 2.6 High magnification SEM images of sintered Ag NP thin film. Processing laser: 514.5 nm green laser with varying laser power and scanning speed. (Scale bar: 100 nm)

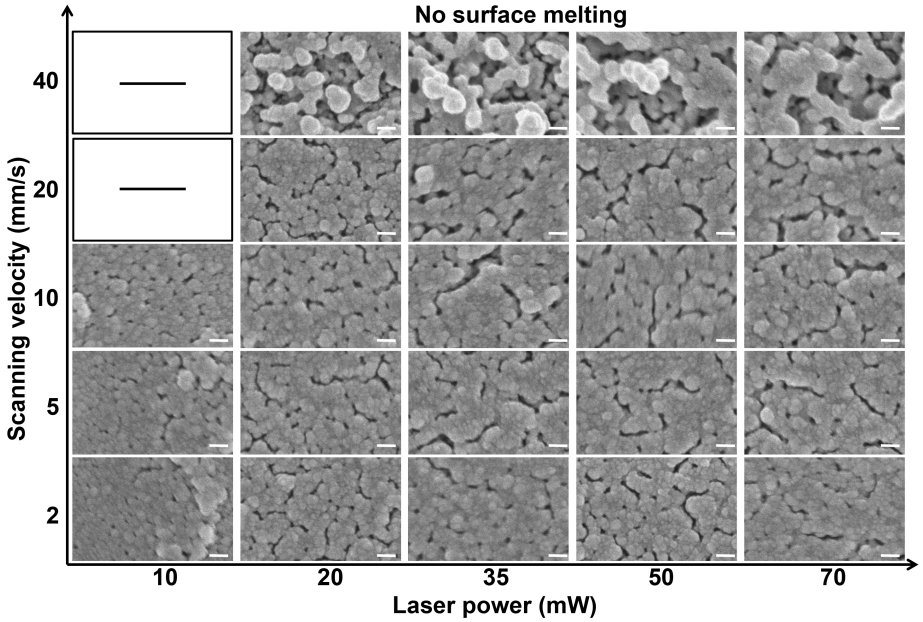

Figure 2.7 High magnification SEM images of sintered Ag NP thin film. Processing laser: 817 nm NIR laser with varying laser power and scanning speed. (Scale bar: 100 nm)

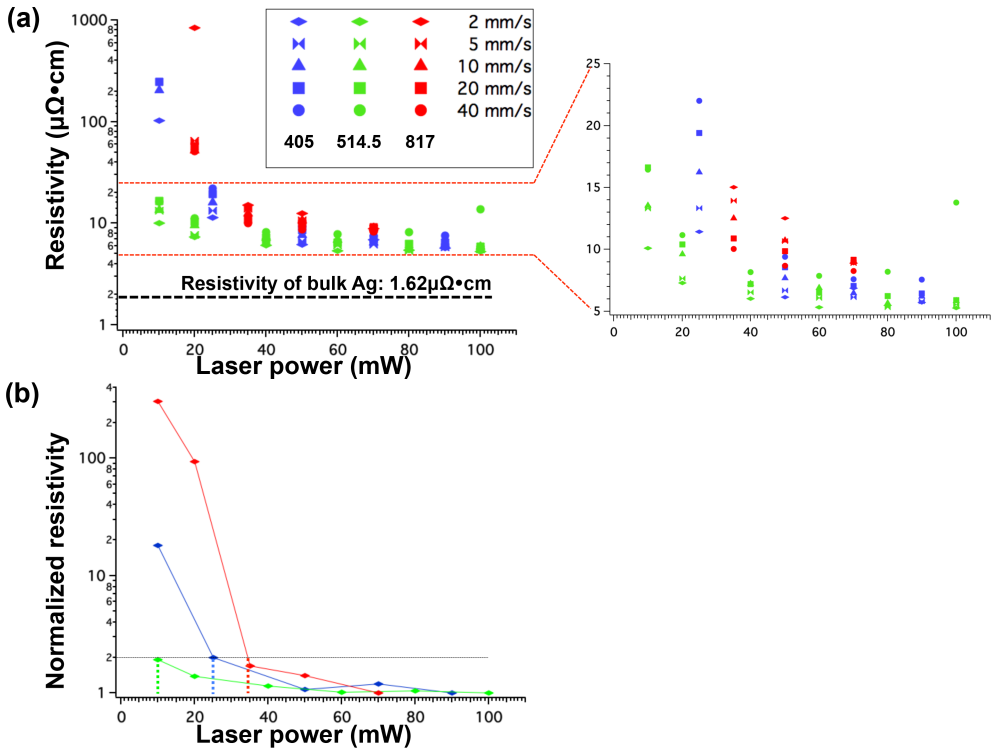

Figure 2.8 (a) Resistivity measurement results. (b) Normalized resistivities at scanning speed of 2 mm/s. Vertical colored line represents the threshold laser power, where normalized resistivity is below 2 and shows convergent behavior (blue: 405 nm NUV laser, green: 514.5 nm green laser, red: 817 nm NIR laser)

2.4.2 Resistivity

Figure 2.8(a) shows that the measured resistivity decreased asymptotically as the laser power increased. This trend can be explained via various sintering models.[55] It is noted that *Ko et al.* studied the nanoparticle neck growth mechanisms upon laser irradiation. Molecular dynamics (MD) simulations show that sintering is initiated by lattice and surface diffusion with negligible neck growth.[56] Thus, at low laser power, the grain size and the effective contact area for the percolation network formed after laser irradiation are small. Consequently, sintered films with low laser power have high resistivity due to electron scattering at the small sized grain boundaries. After the initial stage of sintering, significant neck growth can be expected due to the grain boundary and volume diffusion. At this stage, the neck between the particles thickens and the increased grain size and effective contact area lead to rapid resistivity decrease. Among the three different wavelengths of the processing laser, the green (514.5 nm) laser yields the best results in terms of resistivity.

Table 2.3 summarizes the minimum resistivities obtained at the three wavelengths. The green laser yields the lowest resistivity of 5.28 μΩ•cm at 100 mW with scanning speed of 2 mm/s, which is about 3 times higher than the resistivity of bulk silver. Furthermore, the resistivity reaches an asymptotic minimum at lower laser power in the case of green laser compared to the NUV or NIR laser. **Figure 2.8(b)** shows the normalized resistivities of three different lasers at a fixed scanning speed of 2 mm/s. All values are normalized with respect to the resistivity value obtained at the highest available laser power (NUV: 90 mW, green: 100 mW, NIR: 70 mW). We can define the threshold laser power, P_{th}, where the normalized resistivity is below 2. For the green laser, P_{th} is ~8 mW, while 25 mW and 34 mW for the NUV and NIR laser, respectively. This is also consistent with the resistivity measurement results since the green laser shows the minimum resistivity and NIR laser maximum resistivity.

Table 2.3 Minimum resistivity of Ag NP thin film sintered with three different lasers

Wavelength (nm)	405	514.5	817	Bulk
Resistivity (μΩ•cm)	5.7	5.28	8.9	1.62
Sintering condition (Laser power, scanning speed)	90 mW, 2 mm/s	100 mW, 2mm/s	70 mW, 2 mm/s	-

2.4.3 Sintered pattern width

Figure 2.9(a) shows the sintered line width as a function of laser power for each laser that reveals an increasing trend with higher laser power and a decrease with longer processing laser wavelength. The line width variation is attributed to the sintering threshold and different heat conduction mechanism in each laser. The former can be explained in terms of the difference in absorption of the laser light energy as shown in **Figure 2.9(c)** that depicts the laser light intensity absorbed on the surface of Ag NP thin film for the NUV, green and NIR laser normalized by the

NUV laser energy intensity. The volumetric laser energy generation in the material is given by the following equation,

Equation 2.5 Volumetric laser energy absorbed in the material

$$Q_{ab}(x,y,z,t) = (1-R)I(x,y,t)\alpha e^{-\alpha z}$$

where $Q_{ab}(x,y,z,t)$, $I(x,y,t)$, R, α are absorbed laser light power (W/m^3), incident laser light intensity (W/m^2), reflectivity and absorption coefficient, respectively. Assuming that $I(x,y,t)$ is the same for the three laser beams, $Q_{ab}(x,y,z,t)$ is proportional to (1-R) and α as shown in **Equation 2.5**. The volumetric source by the NUV laser exceeds that by the green or NIR laser at the same laser intensity due to the larger absorption coefficient in the pristine Ag NP thin film. As mentioned earlier, the NUV and green laser sinter a surface layer first and then drive the sintering transversely and vertically by heat conduction, while the NIR laser sinters a narrower vertical column wherein the energy absorption is not sufficient to expand the lateral sintering through the entire Ag NP thin film. This analysis suggests that the laser induced sintering of Ag NP thin film is fundamentally a photo-thermal process. By taking the laser dwell time, τ ($\tau = 2w_o/v$), as a characteristic time scale, we can estimate the thermal penetration depth, l_{th} ($l_{th} \approx (D\tau)^{1/2}$). The thermal diffusivity, D, employed for the calculation of thermal penetration depth was taken 6.75×10^{-8} m^2/s based on the previous evaluation of the thermal conductivity of the pristine Ag NP thin film. For the minimum dwell time of 100 μs at scanning speed of 40 mm/s, l_{th} = 2.6 μm, which is much thicker than the film thickness but still comparable to the beam waist, w_o. Therefore, the energy absorbed during the laser irradiation is confined in the vicinity of the focused region for the high scanning velocities. At lower scanning speeds, on the other hand, it is expected that laser light energy deposited on the focus region can effectively diffuse outwards. Smaller line width is therefore expected for the faster scanning speeds. For the scanning speed of 2 mm/s, the laser dwell time is 2ms, i.e. τ = 2 ms. In this case, l_{th} is calculated as 11.6 μm. However, there is no correlation between scanning speed and sintered line width as shown in **Figure 2.9(b)**. This is possibly due to lower heat dissipation in the lateral direction than the expected according to the above arguments. As mentioned earlier, absorbed laser light energy is dissipated by three-dimensional heat conduction. However, the thickness of Ag NP thin film is only 170 nm, which is much smaller than the beam diameter, and the estimated thermal conductivity of ~ 0.17 W/(mK) is substantially smaller than the thermal conductivity of soda lime glass (~ 0.9 W/(mK)). Furthermore, the thermal conductivity of sintered Ag NP lines estimated by applying the W-F law is by three orders of magnitude higher than the thermal conductivity of pristine Ag NP thin film. As a result, heat is preferentially and anisotropically conducted through the *sintered* Ag NP line and vertically through the glass substrate.

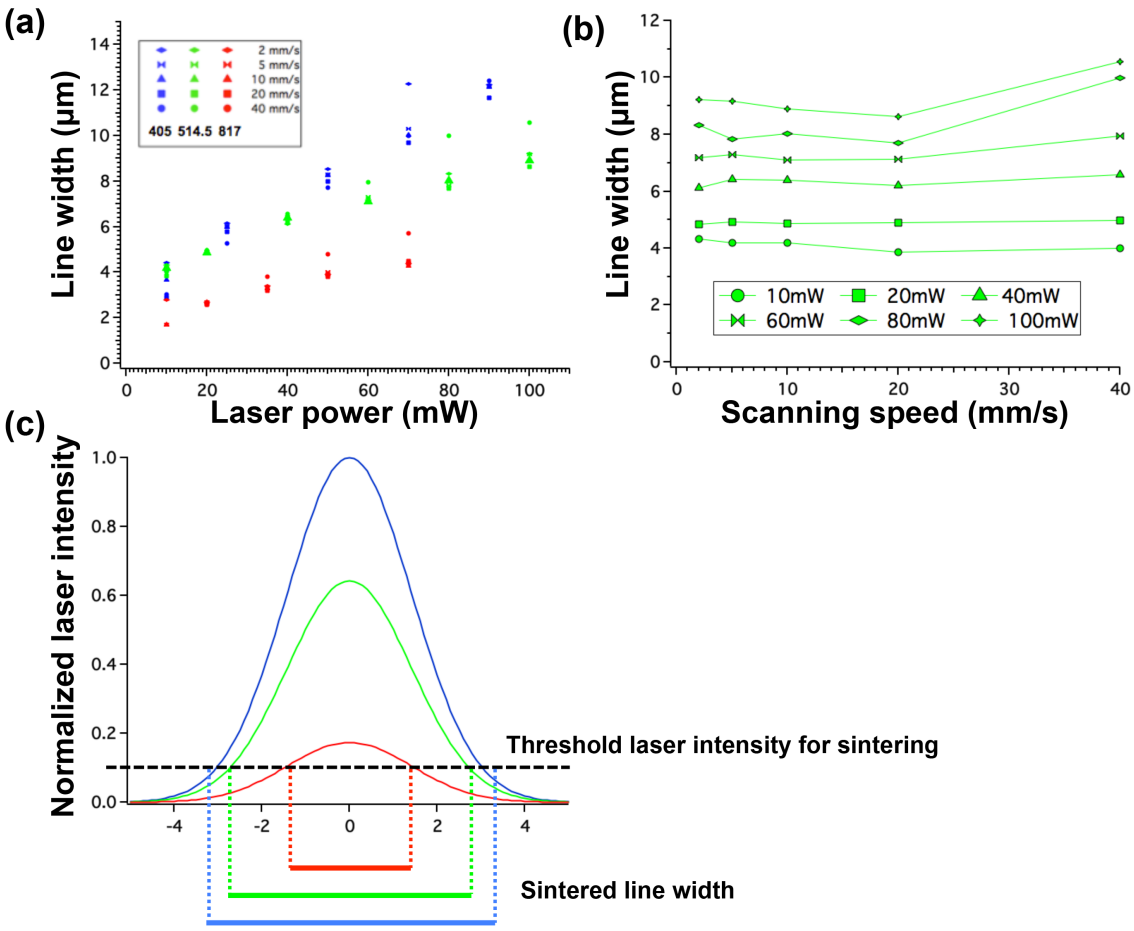

Figure 2.9 (a) Measured line width data of three different laser wavelengths with varying scanning speeds and laser power. (b) Dependence of line width on the scanning speeds for the green laser (wavelength: 514.5 nm) with different laser power (c) Normalized laser intensities at three different wavelengths absorbed on the surface of the Ag NP thin film and corresponding sintered line widths. Absorbed laser light intensities are normalized by the peak intensities of NUV laser. (blue: 405 nm NUV laser, green: 514.5 nm green laser, red: 817 nm NIR laser)

Chapter 3. Characteristic timescales of coalescence

3.1 Overview

Accurate control of the light-nanoparticle interaction plays a pivotal role in the laser induced sintering process and requires fundamental understanding of the dynamics of laser- induced sintering of functional nanomaterials. The coalescence characteristics of the metal ion nanocomposites differ from those of nanoparticle systems since: 1) the host polymer is cross-linked for the initial formation of seed metal atom clusters, 2) the metal atoms diffuse through the glassy polymer matrix resulting in coalescence.[57] *In-situ* optical probing techniques are widely used for observing and analyzing the picosecond and femtosecond dynamics of phonon-phonon, electron-phonon and electron-electron relaxation events. These techniques have been applied to investigate shape transformation, size reduction and phase transition of gold nanoparticle systems during laser irradiation.[58-60] The transient coalescence dynamics of supported gold nanoparticles upon nanosecond laser irradiation has been studied. However, few studies have focused on processing by CW laser, although it is extensively employed in the laser sintering of nanoparticle and nanocomposite thin films.[61] Recently, novel method based on spectral reflectivity measurement was developed to trace the resistivity change of Cu NP thin films while laser irradiation.[15] Even though sintering process evolution of nanoparticle can be measured by employing this method, particle formation and diffusion regime in nanocomposite thin films can hardly be defined with this reflectivity measurement technique. In this paper, we report characteristic time scales of polyvinylpyrrolidone-capped silver nanoparticle (Ag-PVP NP) and silver ion-doped polyvinylalchol nanocomposite (Ag-PVA NC) thin films while CW laser irradiation. By measuring the transient transmission signals through the thin films during laser irradiation, we quantitatively differentiate the Ag- PVA NC sintering process into three distinct regimes, corresponding to particle formation, diffusion and coalescence whose characteristic times are determined. These results are compared with the behavior of Ag-PVP NPs.

3.2 Silver ion doped nanocomposite and silver nanoparticle

Ag-PVA NCs were prepared following previous literature with slight modifications.[62] 0.5 M aqueous silver nitrate ($AgNO_3$, 99.9 %, Aldrich) solution and 4 wt% aqueous PVA (Mw = 31K, 99 % hydrolyzed, Aldrich) solution were prepared in each container, and then the two solutions were mixed together in a 1:1 volume ratio with vigorous stirring for 3 h. Ag- PVP NPs were synthesized from the polyol process.[63, 64] 5 ml of 67 wt% aqueous silver nitrate ($AgNO_3$, 99.9%, Aldrich) solution were quickly injected into 100 ml of fully dissolved 1 wt% PVP (Mw = 10k, Aldrich) in ethylene glycol (EG, 99%, JT Baker) that is preheated to 100 °C with vigorous stirring while kept at 100 °C. After 45 min of reaction, the solution was washed with acetone and centrifuged at 4000 rpm for 20 min. The precipitated Ag-PVP NPs are then dispersed in ethanol (> 99.8 %, Fluka) by 20 min of sonication. **Figure 3.1(a)** shows an illustration of coalescence procedures of Ag-PVA NC and Ag-PVP NP when irradiated by CW laser (Ar-ion laser, wavelength = 514.5 nm, beam diameter = 15 μm). In case of Ag-PVA NC, Ag^+ on in the polymer matrix is coordinated with PVA in a chelate structure.[65] Upon CW laser irradiation, reduction of Ag^+ ion into Ag atom occurs via oxidation of PVA, which causes cross-linking. The produced Ag atoms immediately form dimers, trimmers, etc. by the reduction. These very small metastable silver atom clusters act as seeds for bigger nanoparticles of a few nm in diameter.

Further laser irradiation induces sintering of nanoparticles by diffusion of the produced silver nanoparticles through the PVA polymer matrix. **Figure 3.1(b)** shows the conductive silver metal patterns after scanning Ag-PVA NC with a focused CW laser. After laser irradiation, fully sintered aggregates of silver nanoparticles and their agglomeration marks are generated at the center of the patterned line while partly or unsintered silver nanoparticles are produced at the edge of the line. This difference in morphology is due to the Gaussian nature of the laser beam profile. The reduction and growth of silver nanoparticles from Ag-PVA NCs induced by CW-laser irradiation are similar to the well-studied growth mechanism in metal nanoparticle synthesis.[66] On the other hand, laser-induced sintering of Ag-PVP NPs does not involve these processes as the PVP capping layer is thermally desorbed and adjacent nanoparticles sinter through neck formation driven by viscous flow, grain-boundary, surface and volume diffusion.[67]

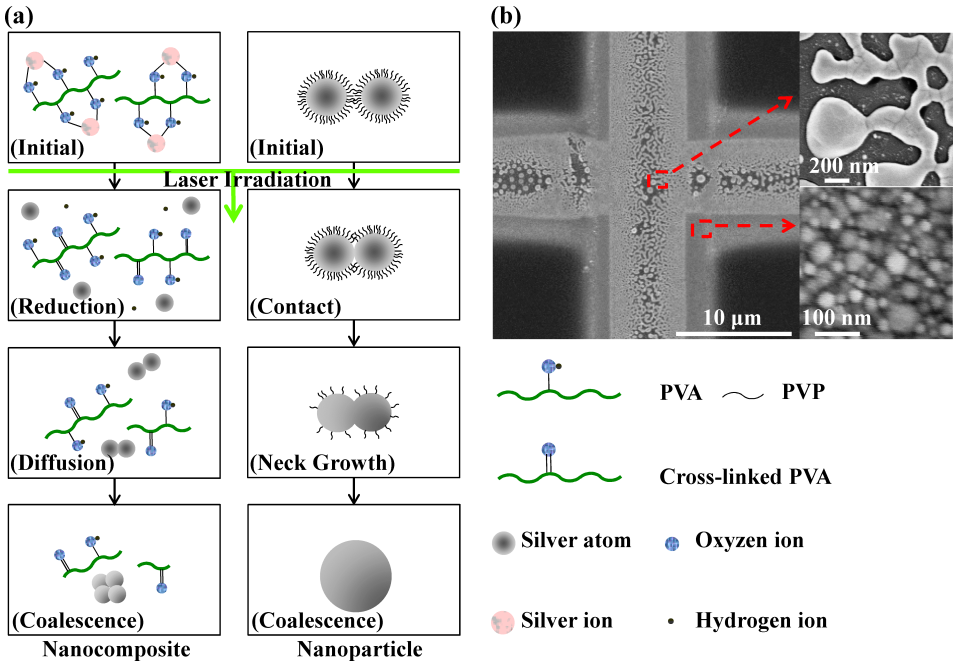

Figure 3.1 (a) Schematics of coalescence process of Ag-PVA NC and Ag-PVP NP upon laser irradiation. (b) SEM image after laser direct writing on Ag-PVA NC thin films

3.3 *In-situ* optical probing traces

To investigate the characteristic time scales for each stage and clarify the differences in sintering processes between Ag-PVP NPs and Ag-PVA NC, an optical probing study has been performed. **Figure 3.2(a)** illustrates the experimental setup and the laser beam configuration. Ag-PVP NP and Ag-PVA NC thin films were prepared by spin coating with spin speed of 1500 rpm for 60 sec on glass substrate. Thin films were then irradiated by the CW laser (Ar-ion laser, wavelength = 514.5 nm) focused by a 10× infinity corrected, non-achromatic long working distance objective lens at normal incidence. A beam splitter and two photodiodes were used to obtain the time-resolved signals. Transient transmission change during the irradiation by the processing laser was measured with each probing laser (633 nm He-Ne laser and 405 nm diode laser) focused by the same objective lens at normal incidence simultaneously. The processing laser signal and the transmission signal of the probing laser were detected by the photodiode 1

and photodiode 2 respectively and recorded simultaneously on the oscilloscope. Since the focal length through a non-achromatic objective lens is dependent on the wavelength of the incident laser beam due to the different refractive index for different wavelengths of light, beam diameter measurement with the knife-edge method was also performed to establish the position of the sample accurately. Measurement errors caused by the Gaussian beam characteristics of the processing beam were minimized by fully utilizing the non-achromatic characteristics of objective lens and adjusting the position of samples on the focal plane of probing laser so that the diameters of the probing and processing beams are 7 μm and 15 μm respectively. The inset in **Figure 3.2(a)** shows the configuration of laser beam and sample during the experiment. For the probing signals, as mentioned earlier, lasers with two different wavelengths were employed: 633 nm He-Ne laser and 405 nm diode laser. The 405 nm wavelength was chosen to detect silver nanoparticle formation and depletion, while the 633 nm wavelength could monitor the silver nanoparticle coalescence. **Figure 3.2(b)** shows extinction spectra of nanoparticle formation inside the Ag-PVA NC thin films measured by spectroscopy in the UV-Vis region when heated at 185 °C on a hot plate for 5 min, 10 min and 15 min, respectively. These results clearly show the peaks around ~ 420 nm which corresponds to the SPR peak of silver nanoparticles with diameter less than 30nm with spherical shapes. **Figure 3.2(c)** shows the extinction spectra of Ag-PVA NC thin films when heated at three different temperatures. A smaller SPR peak and higher transmittance are observed at the low temperature of 100 °C. After heating at 300 °C, the color of the Ag-PVA NC thin film changed drastically, which is attributed to the coalescence of the produced silver nanoparticles. The inset of **Figure 3.2(c)** is a corresponding scanning electron microscopy (SEM) image that clearly shows the agglomerated nanoparticle clusters. Extinction spectra of Ag- PVA thin films heated at 300 °C (**Figure 3.2(c)** black line) have a broad extinction peak centered at around ~600 nm and no SPR peak at 420nm. This peak is the unique feature of agglomerated silver nanoparticles that normally have much bigger size with spherical shapes. Therefore, one can readily detect the formation-depletion and coalescence of silver nanoparticles by the transmission signals at the 405 nm and 633 nm wavelengths, respectively.

3.3.1 Silver ion doped nanocomposite

Figure 3.3(a)-(b) displays the transient transmittance signal changes of Ag-PVA NC thin films at the 405 nm and 633 nm wavelengths during irradiation by the 514.5 nm CW laser at different power densities. **Figure 3.3(a)** shows the normalized transient transmittance signals probing with 405 nm wavelength that traces the formation of silver nanoparticles. A plateau stays through the early stage of laser the irradiation. During this plateau, absorbed light in Ag-PVA NC thin film is converted into heat and the temperature of the thin film increases. At low laser power density, the plateau (Δt_1) holds for tens of milliseconds as indicated in **Figure 3.3(a)**. Δt_1 decreases as the laser power density increases until reaching a minimum of ~ 2.6 ms at the laser power density of 156 kW/cm^2. After Δt_1, a rapid signal drop has been detected, attributed to the silver nanoparticle formation and the efficient extinction of the 405 nm wavelength by the SPR of the produced silver nanoparticles. Thus, Δt_2 in **Figure 3.3(a)** is the time required for the silver nanoparticle formation and is around ~1 ms, regardless of the laser power density and up to 156 kW/cm^2. **Figure 3.3(b)**, showing the transient transmission signals for the 633 nm wavelength probing laser, identifying the coalescence of the silver nanoparticles. These traces clearly have similar trends as **Figure 3.3(a)** in that they exhibit a plateau, Δt_3, that decreases with increasing processing laser power density, reaching a minimum of 98.5 ms at 156 kW/cm^2. The

diffusion time, defined as Δt_3 - (Δt_1 + Δt_2) has a minimum of 95.1 ms at 156 kW/cm^2. Δt_4 in **Figure 3.3(b)** indicates the characteristic coalescence time of generated silver nanoparticles by the laser irradiation showing a minimum of 9.6 ms at 156 kW/cm^2.

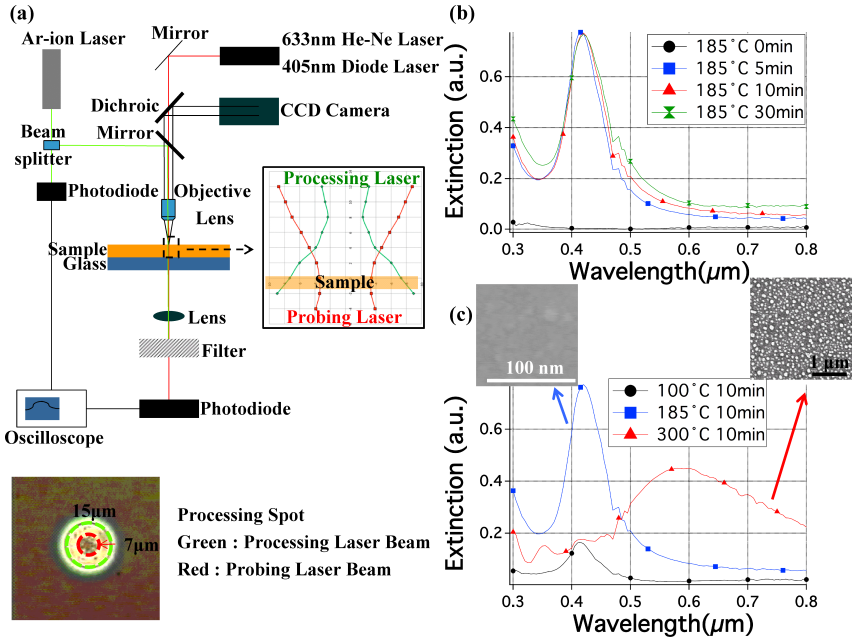

Figure 3.2 (a) Experimental set-up and beam configuration for the pump and probe study. (b) Extinction spectra of Ag-PVA NC thin films for different times of thermal sintering at 185°C. (c) Extinction spectra of Ag-PVA NC thin films with different thermal-sintering temperature with fixed time (10 min)

Over the laser power density of 198kW/cm^2, all three characteristic time scales exhibit anomalous trends. It is expected that boiling of the Ag-PVA NC at higher laser power might distort the transient transmission signals. The nanoparticle formation time scale is ~1 ms regardless of laser power density. Once the temperature of the film exceeds the cross-linking threshold, PVA silver ions can be easily converted to dimers or trimers of silver atoms. However, the diffusion and coalescence time scales depend upon the laser power density; 95.1 ms and 9.6 ms for diffusion and coalescence respectively at the optimized laser power density.

3.3.2 Silver nanoparticle

Figure 3.4(a)-(b) display the transmission traces of the Ag-PVP NP thin films. As noted earlier, neither the particle formation, nor the diffusion are relevant and therefore the relevant time scale for the Ag-PVP NPs is the coalescence time. The overall laser power densities required to process Ag-PVP NPs are much lower than those of Ag-PVA NCs as indicated in **Figure 3.4(a)-(b)**. **Figure 3.4(a)** shows the variation of the transmitted 405 nm wavelength probe beam signals with different laser power densities on Ag-PVP NP thin films. Upon turning on the 514.5 nm processing laser, nanoparticles readily start to agglomerate. As seen in **Figure 3.4(b)**, transmission signals show drops at an early stage. These drops are believed due to the increased fill factor of nanoparticles that is induced by the release of residual or trapped solvent. After the evaporation of solvents, rapid rise of the transmission signal is observed at processing laser power densities higher than 14 kW/cm^2. As seen in **Figure 3.4(b)**, the 633 nm wavelength

transient transmission signal at 14 kW/cm^2 also confirms no nanoparticle coalescence at this power density. At processing laser power densities exceeding 28 kW/cm^2, **Figure 3.4(a)** shows signal increase and **Figure 3.4(b)** decaying traces as we expected due to the depletion of nanoparticle by coalescence. The characteristic coalescence times Δt_5^{405} and Δt_5^{633} that are extracted from the transmission signals at 405 nm and 633 nm wavelength, respectively, are in reasonable agreement and around 10 ms.

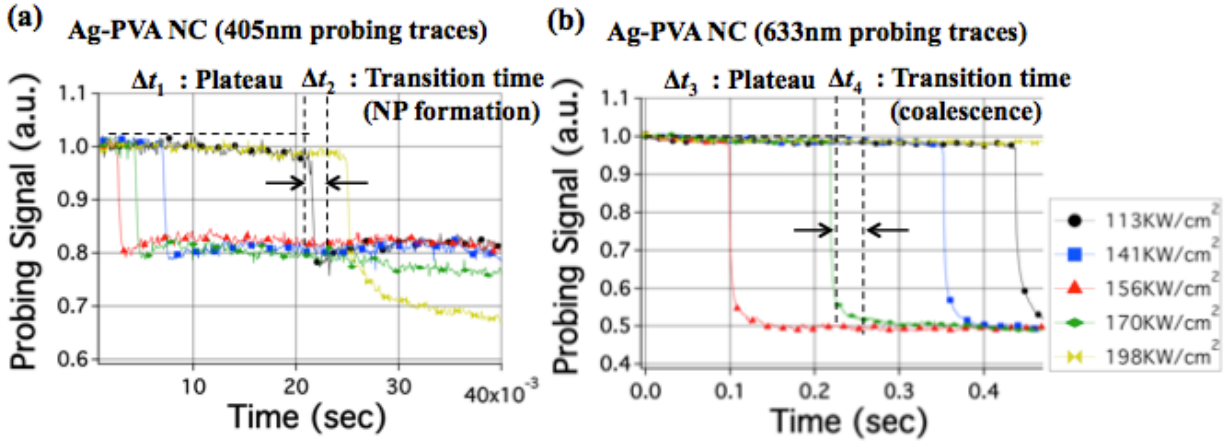

Figure 3.3 Time-resolved transmission traces upon CW laser irradiation at *t=0* with different probing wavelengths (405 nm, 633 nm) and different processing laser power densities on Ag-PVA NC. (a) Ag-PVA NC with 405 nm wavelength (b) Ag-PVA NC with 633 nm wavelength

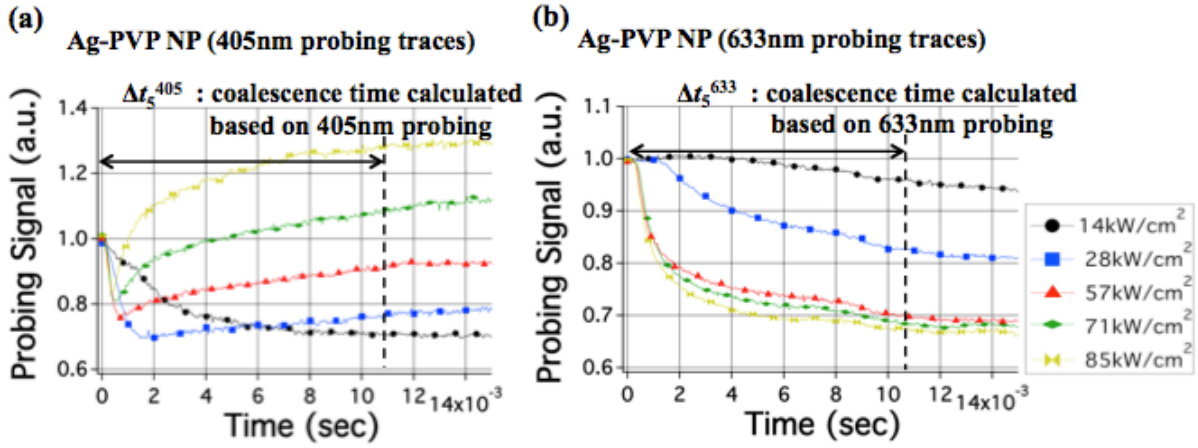

Figure 3.4 Time-resolved transmission traces upon CW laser irradiation at *t=0* with different probing wavelengths (405 nm, 633 nm) and different processing laser power densities on Ag-PVP NP. (a) Ag-PVP NP with 405 nm wavelength (b) Ag-PVP NP with 633 nm wavelength

Chapter 4. Nickel oxide nanoparticle CW laser reductive sintering

4.1 Overview

Nanoscale metal oxide materials such as zinc oxide (ZnO), titanium dioxide (TiO_2), iron (III) oxide (Fe_2O_3), tin dioxide (SnO_2), vanadium (III) oxide (V_2O_3), copper (II) oxide (CuO) and NiO have drawn considerable interest due to fascinating electronic, optical, and thermal properties.[68-70] Among these metal oxides, NiO is a promising material owing to its abundance on Earth and its usefulness in many industrial and research applications including supercapacitors,[71-74] batteries,[75, 76] catalysts,[77, 78] electrochromics,[79-81] p-type semiconducting materials,[82] resistive switching memories,[83] and sensors.[84-86]

Among these nano-morphologies, nanoparticles are widely used due to easy handling, controlled deposition and the high-resolution patterning attainable under ambient conditions when combined with various reduction and/or sintering techniques. For these reasons, several studies have utilized metal oxide nanoparticles to fabricate semiconducting or conducting electrodes. Optical reductive sintering techniques are emerging in this area, since they enable location selectivity as well as accurate temporal control of the process. For example, ZnO NPs were used as an n-type semiconducting material in a thin-film transistor (TFT) device using ultra violet (UV) laser-mediated sintering.[8] Furthermore, copper electrodes have been patterned from CuO NPs using a pulsed laser or intense flashlight.[9-12] However, even though highly conductive copper electrodes have been fabricated, the low oxidation potential energy of copper (0.34 eV) compared to that of other noble metals such as silver (0.799 eV) or gold (1.52 eV) causes degradation of electrical conductivity over time. The deterioration of the electrical performance is accelerated by the high surface-to-volume ratio of the copper agglomerates.[87, 88] To overcome these oxidation problems, electrodes were recently fabricated by flashlight sintering of Ni NPs.[89] More recently, *Lee et al.* introduced a facile route for the synthesis of crystalline NiO NPs and demonstrated a transparent touchscreen panel by laser-induced reduction and sintering of the NiO NP ink.[17] High-resolution Ni electrode patterns were achieved by a simple solution-processed route combined with laser direct writing (LDW) at ambient conditions. Previous studies of the reductive sintering of metal oxide NPs, including those mentioned above, revealed a different behavior of the electrical conductivity to that typically observed in the sintering of noble metal NPs, with the resistivity decrease usually occurring over a wide range of laser powers.[20] In contrast, processing of metal oxide NPs requires tighter control of laser power over a relatively narrow range in order for the final resistivity to be optimized. At laser powers below the optimum range, no reductive sintering reaction occurs and therefore resistivity remains very high. On the other hand, at laser powers exceeding the optimum, the resistivity rises exponentially due to reduced connectivity by islandization of melted NiO NP thin film that may be compounded by re-oxidation as the induced temperature rises.

Since bulk NiO is widely used in industry, its reduction mechanism has already been thoroughly investigated using several characterization techniques, including environmental transmission electron microscopy (TEM),[90] x-ray diffraction (XRD),[91] i*n-situ* time-resolved XRD and NEXAFS/EXAFS (Near Edge X-ray Absorption Fine Structure/Extended X-ray Absorption Fine Structure).[92] The reduction mechanism of NiO in a H_2 environment at high temperature has been described elsewhere as follows: oxygen vacancies increase the adsorption energy of H_2, which in turn lowers the energy barrier associated with the breaking of the H-H bond so that H atoms adsorbed at the vacancy sites easily diffuse into the NiO reaction centers.

Even though the kinetic model for the reduction of bulk NiO is well-established through these studies, direct application to the laser reductive sintering of NiO NPs is not straightforward due to several major differences: 1) the NiO NP size used in the experiments (bulk vs. nanoparticle), 2) the heat source (oven vs. laser), 3) the environment conditions (vacuum and H_2 flowing vs. ambient atmosphere), 4) the sequential reactions of reduction and sintering (i.e. pure reduction vs. reductive sintering). Hence, in order to achieve successful fabrication of electronic devices by laser reductive sintering of metal oxide NPs, a fundamental understanding of the kinetics of the reductive sintering process and precise control of the laser-metal oxide NP interactions is required.

4.2 Experiments

4.2.1 NiO Synthesis

The NiO NP inks were synthesized following the methods used in previous reports with slight modifications. All chemicals were purchased from Sigma Aldrich and used as received. In atmospheric conditions, 514 mg of nickel (II) acetylacetonate ($C_{10}H_{14}NiO_4$) was mixed with 30 ml of oleylamine ($C_{18}H_{37}N$) and 0.64 ml of oleic acid ($C_{18}H_{34}O_2$). This mixture was then heated to 110 °C and stirred vigorously for 1.5 h to remove the moisture and oxygen dissolved in the solution. The solution was then cooled down to 90 °C whereupon a mixture of 0.678 ml borane triethylamine complex ($(C_2H_5)_3NBH_3$) solvated in 4 ml of oleylamine was injected into the solution. The solution was kept at 90 °C for 1 h with vigorous stirring and then cooled down to room temperature. Then 60 ml of ethanol ($(C_2H_6)O$) was added to the solution, followed by centrifugation at 3000-4000 rpm for 15 min. After discarding the solvents, the NiO NPs with average size of ~ 3.7 nm were precipitated at the bottom of the centrifuge tube were further washed and centrifuged with ethanol to thoroughly remove all organic residuals. The NPs collected were dispersed in toluene (C_7H_8) by sonication for 1 h.

4.2.2 Thin film deposition and characterization

Oxygen-plasma-treated 1 mm thick soda lime glass was used as the substrate in this study. Uniform NiO thin films were fabricated by spin coating with the NiO NP ink. Spinning at 2000 rpm for 60s yielded ~230 nm film thickness. Initial thickness of the NiO thin film spin-coated on the soda lime glass is 230 nm. After the reductive sintering by laser, glossy Ni pattern with thickness ~ 40 nm can be achieved. Thickness shrinkage is around 83%. For the high resolution SEM (scanning electron microscopy) imaging and the resistivity calculation, the line width was measured by LEO 1550 Schottky field emission SEM, the thickness was measured by Olympus LEXT OLS3000 3D laser confocal microscope and the resistance measurements were performed HP 4155A semiconductor analyzer. Energy-dispersive x-ray spectrometry (EDS) was performed using FEI quanta 3D field emission gun scanning electron microscope with the X-MaxN silicon drift EDS detector (size: 20mm^2) from Oxford instruments. Raman spectra were acquired at room temperature from the Renishaw inVia confocal Raman microscope using 488 nm Ar-ion laser as exciting source. The laser beam was focused on a ~1 μm spot, using a 50× objective. To measure the absorption coefficient and transmittance, the Sopra GESP broadband variable angle ellipsometry was employed. Finally, the *ex-situ* heating experiments with different gas/gas mixture atmospheres (Ar/forming gas) were performed with a quartz tube furnace at 450 °C for 1 h. And for TEM analysis, As-synthesized NiO NPs were drop cast from toluene onto ultrathin

carbon films on holey carbon supports (Ted Pella #01824). High-resolution TEM imaging and elemental mapping by EDS was performed using an FEI Titan electron microscope operated at 300kV and an FEI Super-X quadrature EDS detector. *In-situ* heating experiments were performed using a Gatan 652 heating holder.

4.2.3 Laser processing

Figure 4.2 shows a schematic of the laser direct writing (LDW) setup. The spin coated NiO thin film was mounted on the computer-controlled x, y, z stage. To induce reductive sintering reactions in the NiO NPs, a 514.5 nm Ar-ion continuous wave (CW) laser beam with a Gaussian beam profile (beam diameter at $1/e^2$ = 4.7 μm) was employed. To write Ni patterns and acquire electrical and optical properties, the NiO thin film was reduced and/or sintered by laser irradiation through a 10× infinity-corrected objective lens at different laser powers and at a fixed (10 mm/s) scanning speed. As the scanning speed increases, the required laser power also increases. In addition, at higher scanning speed, increased time for acceleration and deceleration of the mechanical stage requires bigger experimental samples or more care is required to precisely control the experimental parameters. At lower scanning speed, the processing time gets longer and more subtle laser power control is required. Overall, 10 mm/s was chosen as an effective scanning speed for the experiment considering our current set-up. To produce a Ni-dot matrix pattern, a 2× infinity-corrected lens was utilized. In this case, the Gaussian spatial distribution of the irradiated beam could generate varying morphologies across a single spot. The laser power density and illumination time range were adjusted to avoid thermal damage to the thin films.

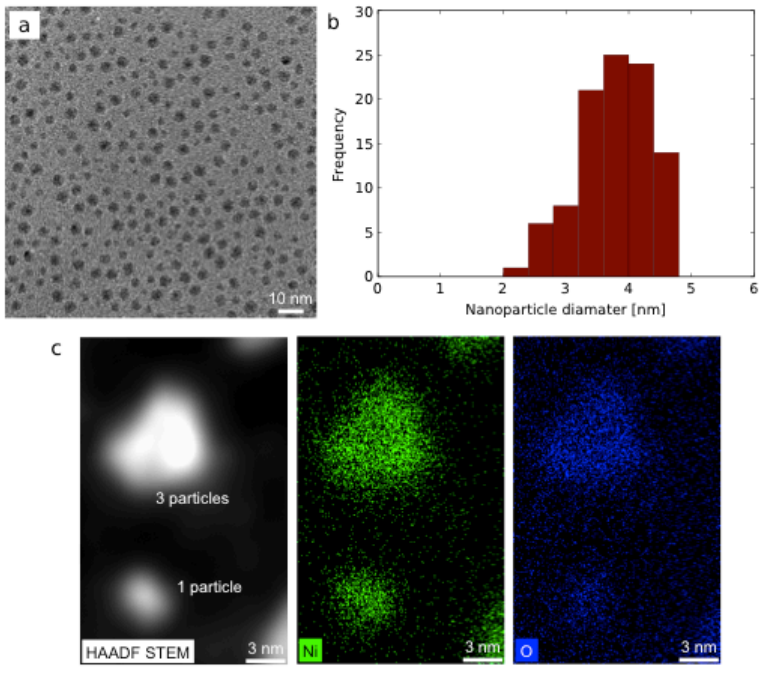

Figure 4.1 (a) TEM image of NiO nanoparticles used in the nanoparticle size calculation. (b) Nanoparticle size distribution (ImageJ SW was used for the image processing and nanoparticle size calculation.) (c) High-Angle Annular Dark-Field (HAADF) Scanning Transmission Electron Microscopy (STEM) image of NiO nanoparticle and element mapping of NiO nanoparticle,

which clearly shows that structure of NiO NPs from our synthesis route is not Ni (core)-O (shell) structure.

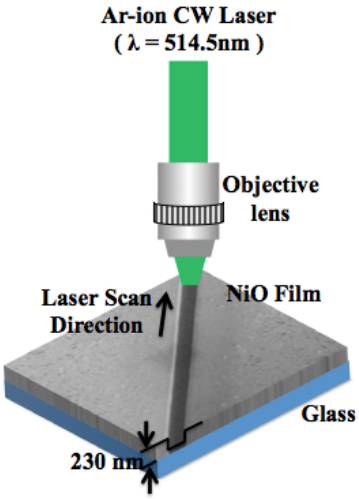

Figure 4.2 Schematics of laser processing set-up. Continuous Wave (CW) Ar-ion laser of 514.5 nm wavelength was utilized for the reductive sintering of NiO thin film.

4.2.4 Time scale measurements.

In-situ optical probing has been used for observing the coalescence of nanoparticles or nanocomposites. *Paeng et al.* exploited the transient variation of the surface plasmon resonance (SPR) peak of silver nanoparticles to accurately measure the coalescence timescale via a transmission configuration. Distinct reflectance changes occur during the reductive sintering reaction and in this study we extended the technique so that normal reflectance and electrical signals could be obtained simultaneously. **Figure 4.3** shows the configuration of the timescale measurement setup. A 633 nm CW He-Ne laser was used as the probe and two fast photodiodes detected the transmittance and normal reflectance changes. The 514.5 nm CW laser beam was used for processing and a mechanical shutter was positioned in front of the laser aperture to control the illumination time. The signal from the processing laser was also detected by fast photodiode. These three signals (normal reflectance, transmittance, processing laser) were recorded concurrently. The NiO thin film specimens were positioned at the focal plane of the probing laser. Conductive pads connected to the oscilloscope for electrical conductance signal measurement were fabricated by ablating the fluorine-doped tin oxide (FTO) glass using a femtosecond laser (amplified Ti:Sapphire laser, 800 nm center wavelength). The gap between the pads was as narrow as ~2 μm to minimize the thermo-capillary effect induced by the Gaussian intensity distribution of the processing beam.

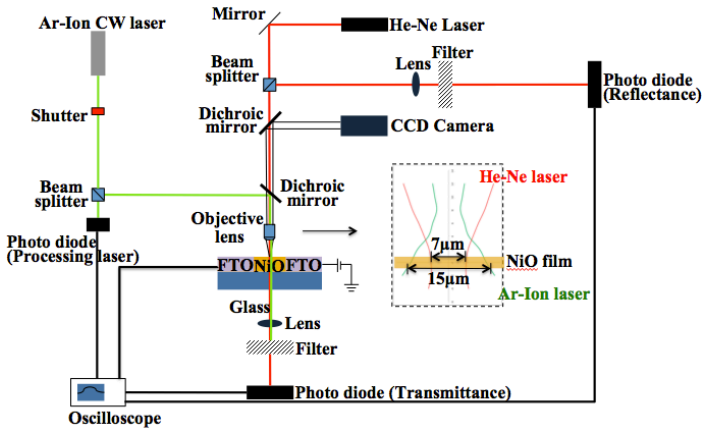

Figure 4.3 Schematics of time resolved transmittance, reflectance and electrical conductance measurement set-up. 633 nm CW He-Ne laser was employed to measure the transmittance and reflectance and 514.5 nm CW Ar-ion laser was used as a processing laser. The shutter has 0.25 ms opening time.

4.3 Band gap narrowing of NiO nanoparticle

Figure 4.4(a)-(b) shows high-resolution TEM images of as-synthesized NiO NPs supported on ultrathin carbon. NiO NPs of average diameter 3.7 nm were found. The NiO NPs exhibit a high degree of crystallinity (face-centered cubic sodium chloride structure) and do not show an amorphous shell. Elemental maps acquired by EDS are shown in **Figure 4.1(c)**. Important contributor to the reduction process is the presence of hydrogen molecules. **Figures 4.4(d)-(e)** show optical images of NiO thin films subjected to two different gases/gas mixtures (Ar and forming gas) respectively, at 450 °C for 1 h. It is important to note that this temperature can induce a direct transformation of NiO to Ni in a reducing atmosphere, since reduction in an H_2 environment generally occurs in the range of 250 - 350 °C.[92] In the Ar atmosphere, the 'translucent black' pristine NiO thin film seen in **Figure 4.4(c)** formed a 'transparent' NiO film, indicating no reduction without H_2. SEM image of Ar-annealed NiO films (SEM image inset in **Figure 4.4(d)**) also suggested no reduction or sintering of the NiO NPs. However, in the H_2 Atmosphere, the pristine NiO thin film transformed into a 'shiny' thin film. This highly reflective appearance signifies a metallic phase. The SEM image inset in **Figure 4.4(e)** indicates that reduction and sintering of the NiO NPs formed aggregates of Ni NPs in the H_2 environment, as also confirmed by sheet resistance measurements: H_2-annealed NiO thin films showed good sheet resistance, as low as 18.6 Ωsq^{-1}. Considering the thermodynamics of the system, the melting temperature of metal NPs is significantly depressed due to the high surface- to-volume ratio. For example, the melting temperature of a ~ 2 nm diameter gold NP is depressed to ~150 °C. Since bulk NiO has a significantly higher melting temperature (1955 °C) than bulk Ni (1455 °C), we postulated that reduction from the oxide (NiO) to metal (Ni) is essential for the subsequent sintering reaction at that temperature to occur. In order to test this hypothesis, we performed an *in-situ* heating experiment in a TEM. Under a high-vacuum environment, the NiO NP film was heated to 450°C for 1 h. **Figure 4.4(f)-(g)** show TEM images of the NiO NPs before and after heating at 450°C for 1 h, respectively. Unlike heating in an H_2 atmosphere, the NiO NPs did not coalesce and retained their shape and size. From these results we infer that the presence of H_2 is critical for reductive sintering reactions of NiO NPs and our proposed mechanism for reductive sintering involving reduction of the NiO NPs to Ni NPs followed by

sintering of the metallic NPs is supported. In a previous study we introduced laser-induced reductive sintering of NiO NP thin films under ambient conditions for the fabrication of Ni electrodes. The thin film composed of NiO NPs in residual toluene solvent was transformed to a Ni film by laser irradiation. Bulk heating of a NiO NP film under ambient conditions did not induce reduction, since toluene (boiling point 111 °C) evaporated before the system reached the temperature range required for reduction (250 °C - 350 °C). However, due to the selective and fast heating achieved by the laser, NiO reduction was achieved even under ambient conditions. Even though hydrogen molecules were not directly supplied, decomposition of the toluene molecules adsorbed on the laser-irradiated NiO NPs enabled reduction to occur. The following reactions are therefore suggested.

Equation 4.1 Chemical reaction of nickel oxide to nickel

$$C_6H_5CH_3 \rightarrow C_6H_5CH_2^- + H^+$$

$$NiO_{1-x} \xrightarrow{h\upsilon, K_BT} NiO_{1-x} + h^+ + e^-$$

$$NiO_{1-x} + 2H^+ + 2e^- \rightarrow Ni + H_2O$$

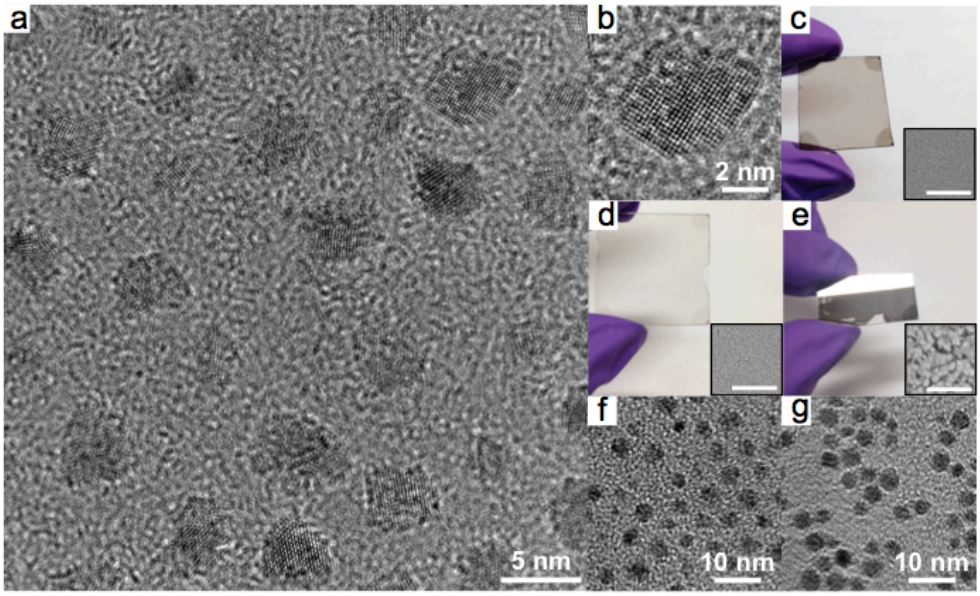

Figure 4.4 (a)-(b) High-resolution TEM image of NiO NPs supported on ultrathin carbon, (c) optical image of the as-deposited pristine NiO NP thin film, (d) optical image of NiO NP thin film annealed at 450 °C under Ar, and (e) under forming gas (H_2 + N_2) (insets for corresponding SEM images; scale bars 200 nm), (f) TEM image of NiO NPs before, and (g) after *in-situ* TEM heating for 1 h (high-vacuum environment).

The absorption coefficient, α, of the as-deposited NiO NP film was calculated as 0.81×10^4 cm^{-1} using the expression, $\alpha = 4\pi k/\lambda$, where k and λ are the imaginary part of the complex refractive index measured by ellipsometry and the wavelength of the laser, respectively. Since toluene is non-absorbing at the 514.5 nm wavelength, laser light is selectively absorbed by the NiO NP film inducing a fast temperature rise that is high enough to initiate pyrolytic

decomposition of toluene to anions and protons (**Equation 4.1**). The NiO NP film not only acts as a heat-absorbing material but also as an electron donor. Typically, bulk NiO is known as a p-type semiconducting material with a wide band gap. For a direct-transition-type semiconducting material, the optical band gap, E_g, can be calculated using the absorption coefficient and Tauc's equation:[93]

Equation 4.2 Tauc's equation

$$\alpha h\upsilon = A\left(h\upsilon - E_g\right)^n$$

where α, *h, v, and A* denote the absorption coefficient, Planck's constant, frequency of the photon and a constant, respectively. For a direct transition, the exponent *n* is 1⁄2. **Figure 4.6(b)** illustrates the relationship between $(\alpha h\nu)^2$ and $h\nu$ (the photon energy) for as-deposited pristine NiO. By fitting the linear part of the plot and extrapolating to the $h\nu$ axis, the optical band gap, E_g, can be derived. The NiO_{1-x} NPs from our synthesis route have a lower optical band gap (E_g = 2.28 eV) than the value reported elsewhere (> 3.4 eV),[94, 95] which we attribute to a higher density of oxygen vacancies in our samples.[96] With the reduced optical band gap, electrons in the valence band can easily be excited to the conduction band by the 514.5 nm laser irradiation. Furthermore, with the high oxygen vacancy density of synthesized non-stoichiometric NiO_{1-x} NPs, defect-level electrons can be photothermally excited to the conduction band.[97] These electrons (**Equation 4.1**), combined with the protons react with the NiO NPs to initiate reduction.

4.4 Kinetics of laser reductive sintering of NiO nanoparticle

To characterize the effect of laser power on the reductive sintering kinetics, as-deposited NiO NP films were subjected to laser irradiation at a scanning speed of 10 mm/s. **Figure 4.5(a)-(f)** show SEM images of the as-deposited pristine NiO thin film and of the film following irradiation using different laser power densities: 71 kW/cm^2, 89 kW/cm^2, 118 kW/cm^2, 153 kW/cm^2 and 249 kW/cm^2. While there was no coalescence up to 71 kW/cm^2, necking between adjacent nanoparticles appeared at the power density of 89 kW/cm^2, indicating that reductive sintering occurred. **Table 4.1** summarizes the resistivity, ρ, of Ni electrodes generated by laser irradiation of NiO NP thin films, calculated from the equation, $\rho = Rwt/l$, where *R*, *w*, *t* and *l* are the resistance, width, thickness and length of the single line electrode, respectively.

Table4.1 Resistivity of laser-irradiated (i.e. reduced) NiO NP and bulk Ni line patterns. XXX denotes the measurement limit of the semiconductor analyzer

Laser power density (kW/cm^2)	71	89	118	153	249	Bulk Ni
Resistivity (μΩcm)	XXX	111.9	91.2	65.3	107.8	6.99

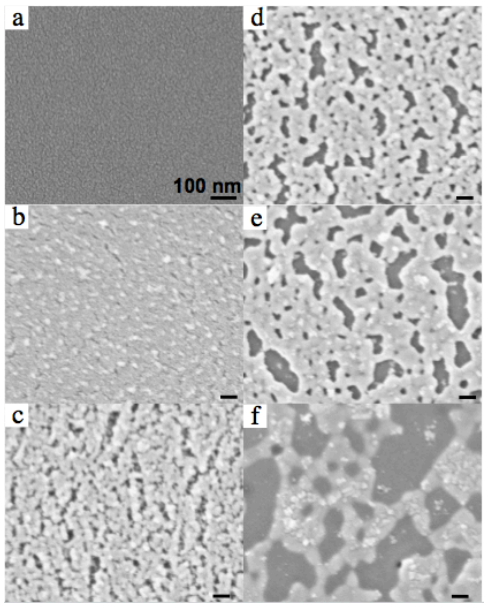

Figure 4.5 SEM images of NiO NP thin films showing different morphologies for various laser power densities at fixed scanning speed (10 mm/s). (a) Pristine NiO (before irradiation), (b) 71 kW/cm^2, (c) 89 kW/cm^2, (d) 118 kW/cm^2, (e) 153 kW/cm^2, and (f) 249 kW/cm^2

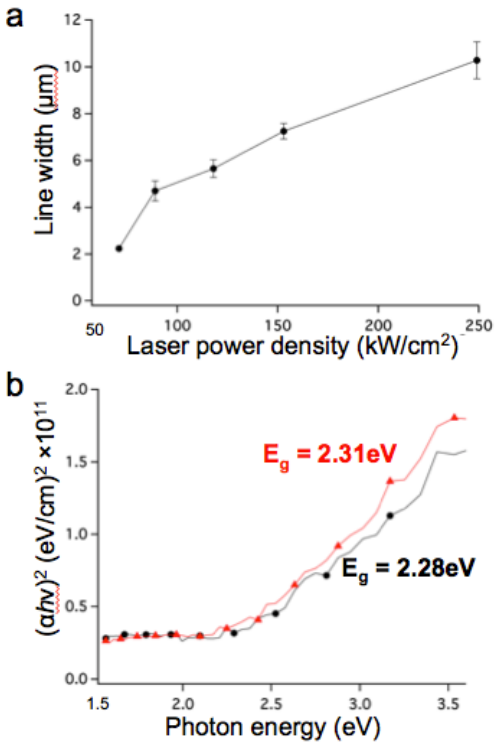

Figure 4.6 (a) Width of Ni line patterns produced using different laser power densities at fixed scanning speed (10 mm/s). (b) Tauc's plot of as-deposited pristine NiO thin films(●) and thin films irradiated using laser power density of 71 kW/cm^2 (▲)

Figure 4.6(a) shows the width of the Ni line patterns (measured by SEM) written by scanning the 4.7 μm diameter ($1/e^2$) Gaussian-profile laser beam as a function of laser power density, which was used to calculate the resistivity of Ni electrodes. The line width increased from 2.2 μm at 71 kW/cm^2 to 4.7 μm at 89 kW/cm^2. Since the reduction of NiO NPs to Ni NPs was initiated above 71 kW/cm^2, the enhanced absorption by the reduced Ni NPs in the central area of the laser beam increases the transverse conductive heat transfer, contributing to the line width increase observed at 89 kW/cm^2. Furthermore, at power densities exceeding 71 kW/cm^2, the reduced Ni NPs act as self-catalysts accelerating the reductive sintering by increased absorption and electron donation. These trends can be inferred from **Figure 4.8(a)-(b)** and **Figure 4.7**, which show the transmittance, absorption coefficients and Raman spectra, respectively, of the NiO NP thin films irradiated using the different laser power densities. A significant drop in transmittance and increase in the absorption coefficient are observed as the laser power density increases from 71 kW/cm^2 to 89 kW/cm^2. We note that two vibrational modes at ~570 cm^{-1} and ~ 1100 cm^{-1} corresponding to the first-order longitudinal optical phonon mode (1LO) and the second-order longitudinal optical phonon mode (2LO)[98, 99] are identified in the Raman spectrum of the pristine NiO thin films, whereas for perfect cubic-structured NiO the 1LO peak should not appear.[100] This indicates a high oxygen vacancy concentration in the pristine NiO film. Furthermore, the second-order magnon mode (2M) peak at 1400-1500 cm^{-1} was not observed in the pristine film, which we attribute to the decrease in spin correlation length for small nanoparticle sizes and the disorder induced by oxygen vacancies. At the low laser power density of 71 kW/cm^2, the absorption coefficient remained nearly the same as that of the pristine film, but the transmittance slightly increased due to the larger fill factor of the NiO NPs (a decrease in the thickness of the NiO NP films due to densification) induced by the release of trapped toluene and other residual organics. The transmittance increase can also be attributed to the diminished oxygen vacancy concentration. **Figure 4.6(b)** shows that the optical band gap of the thin film irradiated with 71 kW/cm^2 increased slightly from 2.28 eV to 2.31 eV, implying optical band gap broadening by depletion of the oxygen vacancies. However, at 89 kW/cm^2 the transmittance decreased drastically across the spectrum due to the absorption increase. These data are consistent with the line width measurements. In the Raman spectrum for the 89 kW/cm^2 laser power, the 1LO and 2LO peaks decreased. This depression of the 1LO and 2LO peaks is indicative of the reduction of the NiO NPs to Ni NPs at kW/cm^2, while the appearance of two carbon peaks, the D band at ~1370 cm^{-1} and the G band at ~1590 cm^{-1}, is attributed to toluene decomposition. The above results suggest that initiation of NiO NP reduction to Ni NPs requires a laser power density threshold, P_{th}, between 71 kW/cm^2 and 89 kW/cm^2. At 118 kW/cm^2, the 1LO and 2LO peaks in the Raman spectrum disappeared and the carbon phase peaks decreased. The lowest resistivity was achieved at the laser power density of 153 kW/cm^2, where the spectral transmittance and absorption coefficients were the lowest and highest, respectively. The Raman spectrum at this laser power density shows no NiO-related peaks, indicating completion of the reductive sintering process. Therefore, we conclude that 153 kW/cm^2 is near or at the optimum power level for the reductive sintering of the NiO NPs. At laser powers above the optimum power level, re-oxidation deteriorates the electrical conductivity. The re-appearance of the 2LO peak and decreased absorption coefficient at 249 kW/cm^2 also supports this postulation. Since reductive sintering involves a phase transition from metal oxide to metal, optical reflectance should in principle increase as the reductive sintering reaction occurs. However, absorption is much greater than scattering for NPs of size much smaller than the wavelength of visible light.[101]

Hence we can expect that the extinction by absorption in a reduced but still un- sintered NP film will be much more pronounced than any reflectance change. The reflectance increase becomes apparent once the size of the coalesced Ni NP agglomerates becomes comparable to the wavelength of light. These trends are observed in **Figure 4.8(c)**. The normal incidence reflectance, R_λ, as a function of wavelength, was calculated by invoking the following equation,

Equation 4.3 Normal incidence reflectance

$$R_\lambda = \frac{(n_\lambda - 1)^2 + k_\lambda^2}{(n_\lambda + 1)^2 + k_\lambda^2}$$

, where n_λ and k_λ are real and imaginary part of the complex refractive index of NiO NP thin film measured by ellipsometry, respectively. R_λ increases markedly at the laser power density of 89 kW/cm^2, where, as noted previously, sintering was observed. The increase persists until about 13 kW/cm^2, where the lowest resistivity was achieved, and thereafter drops as the film re-oxidizes.

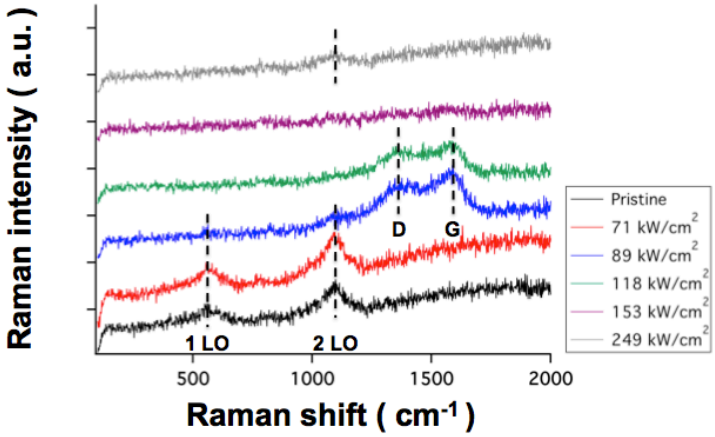

Figure 4.7 Raman spectra for NiO NP thin films fabricated by irradiation of pristine NiO thin films using different laser power densities with fixed laser scanning speed (10 mm/s).

We were able to distinguish four regimes during the laser irradiation of the NiO NP films: oxidation, reduction, sintering and re-oxidation. The reductive sintering kinetics should be revealed by tracking the temporal and spatial evolution of the phase transformation process. For this purpose, a 5×9 dot matrix was produced by stationary laser irradiation of a NiO NP thin film using different laser powers and exposure times, as shown in **Figure 4.9(a)**. As can be seen in the optical images, the center region of the dot exposed for 500 ms at 47 kW/cm^2 (labeled 2) became reflective, while the dot exposed for 200 ms at the same power (labeled 1) did not. As mentioned above, a sharp increase in reflectance signifies sintering. The corresponding SEM images in **Figure 4.9(b)** confirm that reductive sintering occurred by 500 ms. In contrast, no such morphological change is evident at 200 ms irradiation. The dot diameter produced for 47 kW/cm^2 increases as the irradiation time increases from 200 ms to 500 ms (**Figure 4.10**). However, for laser power densities exceeding 47 kW/cm^2, the required irradiation time for effective reductive sintering decreases substantially at 53 kW/cm^2, reductive sintering occurred after only 10 ms exposure. This discontinuity in the exposure times required for reductive

sintering at 47 kW/cm^2 versus 53 kW/cm^2 is consistent with a threshold-like behavior. SEM images of the dots produced at 65 kW/cm^2 (**Figure 4.9(b)**: labels 4 and 5) reveal morphologies different to those of sintered films, possibly due to re-oxidation.

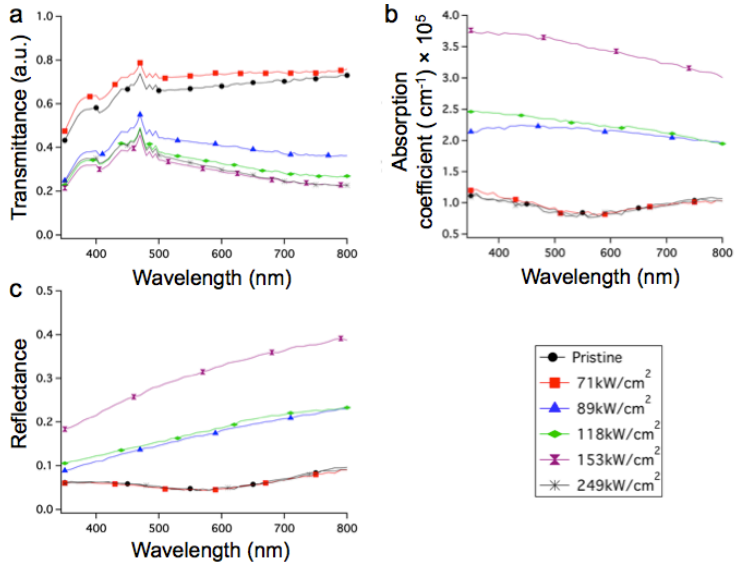

Figure 4.8 (a) Transmittance, (b) absorption coefficients, and (c) calculated normal reflectance of NiO NP thin films fabricated by irradiation of pristine NiO NP thin films using different laser power densities with fixed laser scanning speed (10 mm/s).

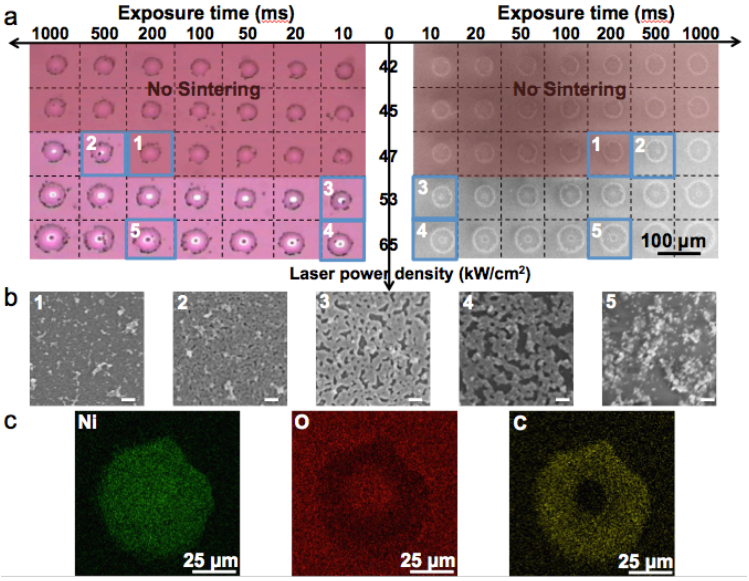

Figure 4.9 (a) Optical (left) and SEM (right) images of 5×9 dot matrix produced by stationary laser irradiation on NiO NP thin film using different laser power densities and exposure times. (b) Selected higher magnification SEM images of center region of the dots (corresponding to labeled SEM images in (a)). (Scale bar 200 nm). (c) SEM-EDS images of dot produced using laser power density of 65 kW/cm^2 and 1000 ms exposure.

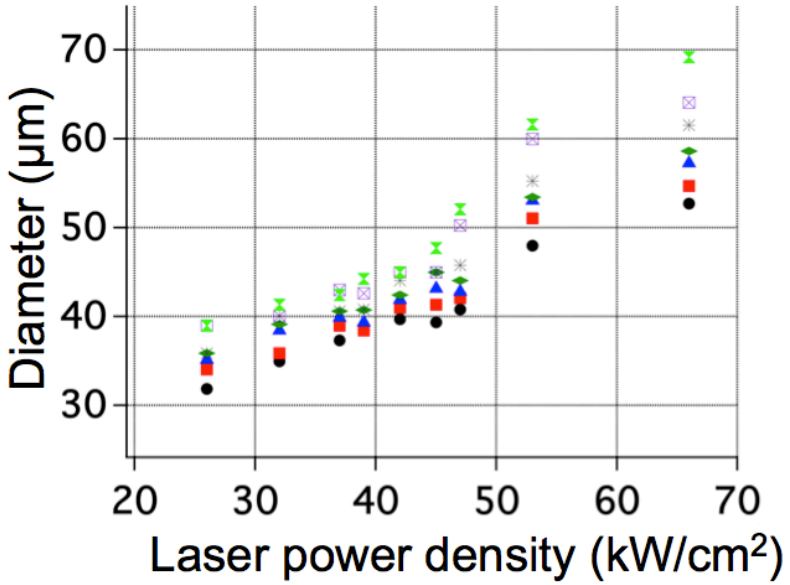

Figure 4.10 Measured diameter of fabricated dots (**Figure 4.9(a)**) with different laser power densities and different irradiation time. In **Figure 4.9(a)**, Optical and SEM images of dots at 26 kW/cm^2, 32 kW/cm^2, 37 kW/cm^2, 39 kW/cm^2 were not displayed. Different markers with different colors denote the exposure times. (10 ms: ● , 20 ms: ■ , 50 ms: ▲ , 100 ms: ◆, 200 ms: ✳ , 500 ms: ⧗, 1000 ms: ☒). The laser beam was non-moving.

Figure 4.11 shows Raman spectra measured at three different locations within the processed dot (center, rim, and edge). Corresponding SEM and optical images are also shown in order to correlate the Raman spectra with the morphological changes and optical characteristics. At 47 kW/cm^2 with an exposure time of 10 ms, both the 1LO and 2LO vibrational modes characteristic of the oxide phase appear and no necking signifying sintering can be found, even in the center region where maximum temperature is expected. At 53 kW/cm^2 and the same exposure time of 10 ms, Raman spectra taken from the rim and the edge region show the 1LO and 2LO vibrational modes. These modes are absent in the spectrum acquired from the center region, confirming conversion to Ni. The difference in the Raman spectra in radial direction is due to the Gaussian shape of the laser beam intensity profile. The SEM image for this laser power density also reveals sintering in the center region. In contrast, no or negligible sintering is observed in the rim and edge regions. At the higher laser power density of 65 kW/cm^2 and an extended exposure time of 1000 ms, a decrease in the normal reflectance induced by re-oxidation is detected in the center region (optical image in **Figure 4.11(c)**). Raman spectra from this region also show the NiO 2LO vibrational mode. However, the rim region shows shiny features in the optical image and well-defined necking morphologies. The Raman spectrum taken at this rim region also verifies that the film underwent reductive sintering. SEM- EDS data for the dot written at 65 kW/cm^2 with an exposure time of 1000 ms are shown in **Figure 4.9(c)** and confirm that the center region is re-oxidized while the circular rim region is reduced and sintered without undergoing oxidation. Additionally, trace carbon produced by the evaporation and decomposition of toluene is detected in the circular rim region.

Table 4.2 Characteristics of NiO NP thin films irradiated using different laser power densities for the four reaction regimes of the phase transformation process.

Laser power density	P_{low}	P_{th}	P_{opt}	P_{high}
Reaction	Oxidation / densification	Reduction wo. sintering	Sintering	Re-oxidation
Electrical conductance	-	↑	Max	↓
Transmittance	↑	↓	Min	↑
Normal reflectance	↓	↑	Max	↓

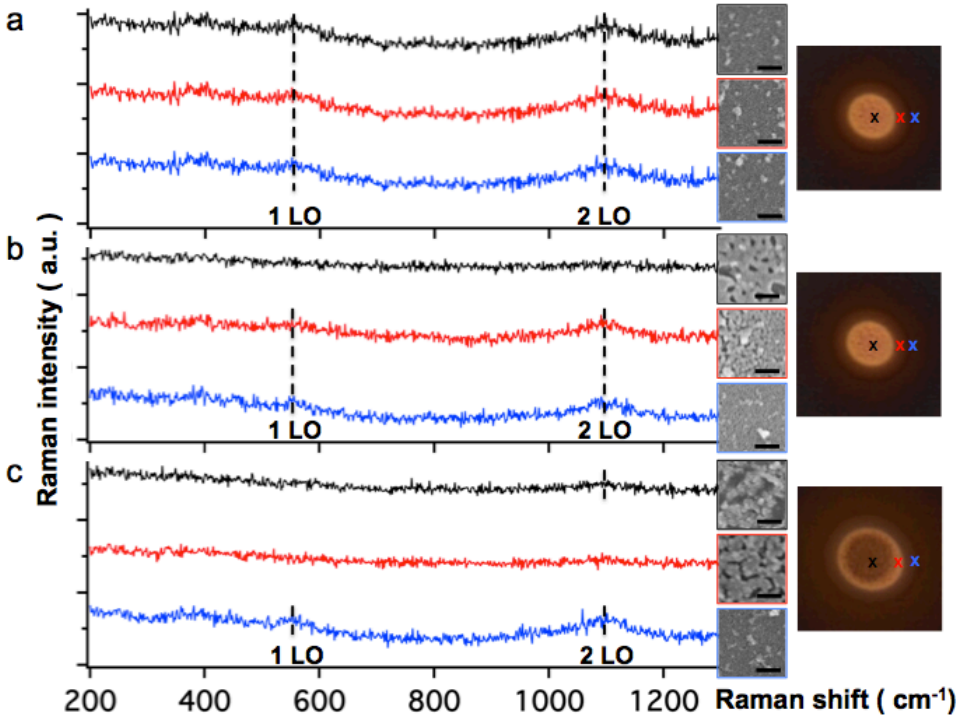

Figure 4.11 Raman spectra for edge (×, −), rim (×, −), and center (×, −) regions of dot structures with corresponding optical and SEM images shown on the right, for laser power densities (a) 47 kW/cm^2, (b) 53 kW/cm^2, and (c) 65 kW/cm^2 (Scale bar 200 nm). The laser beam was non-moving.

4.5 Characteristic time scales of laser reductive sintering of NiO nanoparticle

Table 4.2 summarizes the optical and electrical characteristics of NiO NP thin films irradiated using different laser powers for a fixed exposure time. The subscripts *low*, *th*, *opt*, and *high* denote laser power densities lower than the reduction threshold, at threshold, at optimum (where maximum electrical conductivity is attained) and higher than optimum, respectively. The upward and downward facing arrows represent increasing or decreasing values, respectively. As

mentioned, the reductive sintering of NiO NPs encompasses the sequential reduction and sintering processes. Therefore, *in-situ* measurement of the transient electrical conductance, normal reflectance and transmittance can determine the timescales of the reductive sintering process. **Figure 4.12(a)** shows the time-resolved normal reflectance for different laser powers. The normal reflectance and transmittance traces were normalized with respect to their initial values before laser irradiation. The probing laser used for the measurements is 633 nm He-Ne laser. The laser was turned on at $t = 0$. At the low laser power density of 26 kW/cm^2, well below P_{th}, the reflectance decreased by half in ~1.4 ms. At this laser power density, no reductive sintering occurred. The NiO NP film is densified due to desorption of trapped solvents and other residual organics, and oxidized slightly. At laser power densities above P_{th}, the reflectance increased rapidly to a maximum at 1.4 ms (even though in the early stage of irradiation until about 410 μs the reflectance decreased). At 47 kW/cm^2, the reflectance initially decreased again, but does not appear to fully recover to its initial value. Considering that sintering was evident at 47 kW/cm^2 for an exposure time of 500 ms (**Figure 4.9(a)-(b)**), it is expected that the reductive sintering threshold, P_{th}, should fall between 47 kW/cm^2 and 53 kW/cm^2, with the process being highly sensitive to laser power density. In this parametric study, maximum reflectance was recorded at 53 kW/cm^2, which should be close to P_{opt}. Further increase in the laser power density up to 65 kW/cm^2 induces re-oxidation that is marked by a drop in reflectance. The temporal evolution of the transmittance is illustrated in **Figure 4.12(b)**. In the early stage of laser irradiation, the transmittance increases until about 330 μs after which it starts to decrease rapidly reaching a minimum at 1.4 ms that is maintained thereafter. The same timescale is extracted from the electrical conductance data shown in **Figure 4.12(c)**. For the low laser power density of 26 kW/cm^2, electrical conductance does not change and remains near zero, which implies no effective reductive sintering. At 53 kW/cm^2, the electrical conductance increases and then plateaus at a constant value. It is worth noting that the rise time to the maximum electrical conductance depends on the laser power. Since the reduction rate at 53 kW/cm^2, which is near P_{th} is much slower than that at P_{high}, it takes a longer time to reach the electrical conductance maximum. At the higher laser power density of 65 kW/cm^2, even though electrical conductance increases abruptly at the early stage, it then decreases due to re-oxidation and the dewetting-induced morphological change ('fingered' structure). The temporal evolution of the normal reflectance, transmittance and electrical conductance at the optimum laser power density of 53 kW/cm^2 is illustrated in **Figure 4.12(d)**. Starting at 90 μs, the transmittance increases to the peak at 310 μs, marking densification and slight oxidation. The transmittance then decreases rapidly while the electrical conductance starts to slowly increase due to the toluene decomposition and the reduction of NiO NPs. However, the normal incidence reflectance keeps decreasing until 410 μs, after which the reflectance starts to increase, the electrical conductance also increasing rapidly due to sintering. The reflectance peaks at 1.4 ms. **Table 4.3** summarizes the timescales for the reductive sintering process for a laser power density of 53 kW/cm^2.

Table 4.3 Timescales for the reductive sintering reaction of NiO NP thin films at 53 kW/cm^2

Reaction	Densification + Oxidation	Reduction	Sintering	Re-oxidation
Time (μs)	220	100	~ 990	-

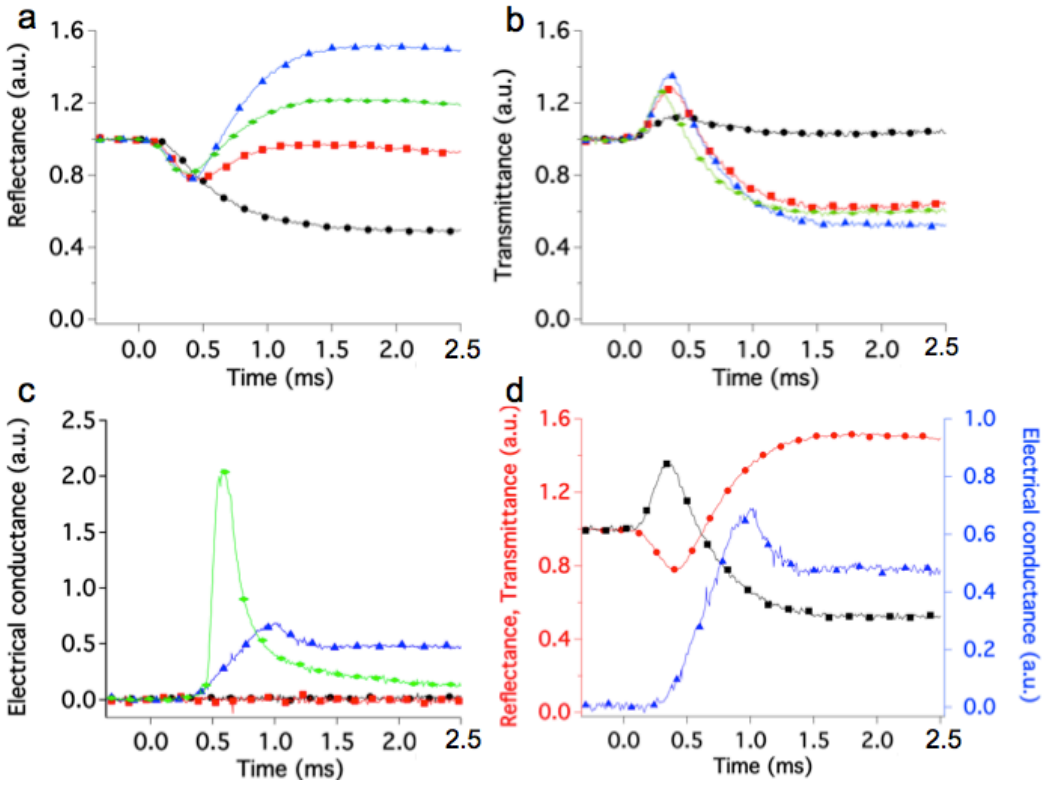

Figure 4.12 (a) Time-resolved normal reflectance, (b), transmittance, and (c) electrical conductance data for different laser power densities: 26 kW/cm^2 ( ), 47 kW/cm^2 ( ), 53 kW/cm^2 ( ) and 65 kW/cm^2 ( ). (d) Temporal evolution of normal reflectance ( ), transmittance ( ), and electrical conductance ( ) signals for a laser power density of 53 kW/cm^2.

4.6 Fabrication of transparent conductor by laser reductive sintering of NiO nanoparticle

Figure 4.13(a) shows a scanning electron microscopy (SEM) image of an electrode line defined by a single scan of the laser beam at power of around 159 kW/cm^2. The line width of the electrode is measured to be approximately 6.5 μm, which is related to temperature distribution induced by the laser irradiation. The maximum temperature increases at higher laser power and slower scan speed, hence enlarging the electrode width. **Figure 4.13(b)-(c)** shows top view SEM images of the mesh-type electro- des with different magnifications. It is worth noting that the edges of the laser-sintered electrode lines are sharp, suggesting that this LDW reductive sintering process can be applied to a high-resolution electrode fabrication. Insets in **Figure 4.13(b)** are the elemental mapping images for Ni and O acquired from energy-dispersive X-ray spectroscopy (EDX) analysis of the mesh-type electrodes on a glass substrate. EDX analysis was carried out at an accelerating voltage of 2 keV.

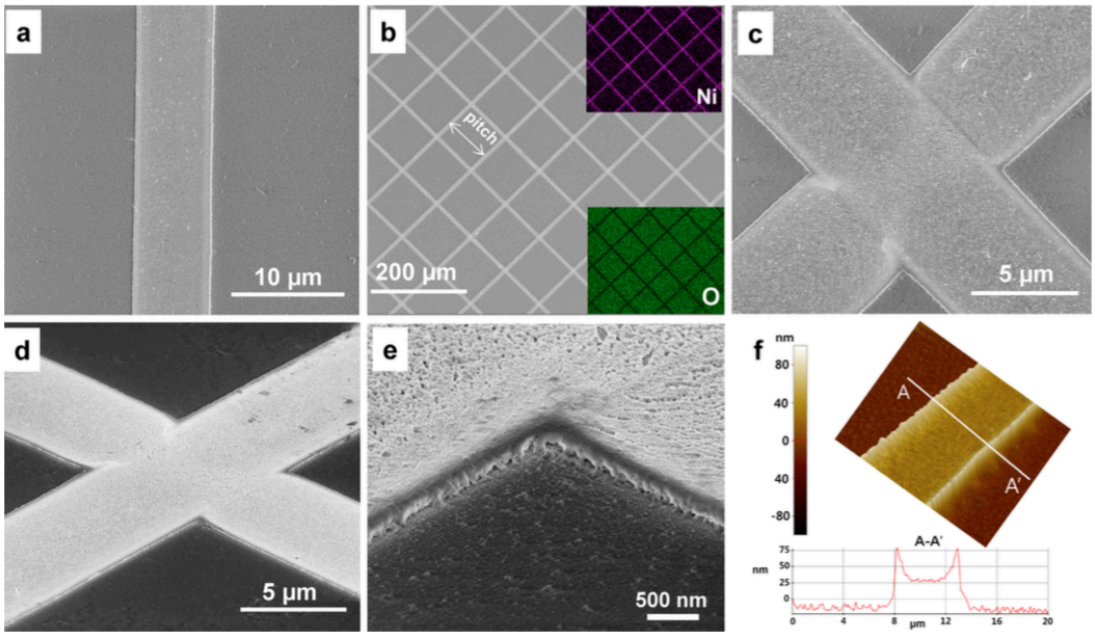

Figure 4.13 (a) Top view SEM image of a single Ni electrode. The line width is around 6.5 μm. (b,c) Top view SEM images of mesh-type electrodes with different magnifications. The mesh-type Ni grids are generated by two-time laser scanning – one time per each direction. (d,e) Tilted view images of the intersection area of the mesh patterns. (f) AFM image of a single electrode. The cross-sectional shape is plotted on different axis scales.

The images show a clear contrast between Ni and O elements in the electrodes, suggesting that laser irradiation effectively removes oxygen from the NiO NP film while the washing process cleanly removes the nonirradiated parts. The tilted view images of the intersection area of the mesh patterns in **Figure 4.13(d)-(e)** further show the feature quality. The electrode is thicker near the edge than at the center due to thermocapillarity, and the nominal thickness of the electrode measured by atomic force microscopy (AFM) is around 35 40 nm, as shown in **Figure 4.13(f)**. The rms (root mean square) value of the surface roughness at the center area of the electrode is around 2.6 nm. It is noted that the contrast of the thickness in the cross-sectional shape is amplified by the different axis scales (x-axis, μm; y-axis, nm). We expect that a flatter shape of the electrodes can be achieved by employing a top-hat laser beam or the two- beam configuration, which reduces the temperature gradient on the laser-irradiated area. As a device demonstration, mesh-type Ni grids on a glass substrate were applied for a transparent 4-wire resistive touch screen panel, as shown in **Figure 4.14(a)-(b)**. A 3.8 cm 4.8 cm mesh grid of 80 μm pitch was generated by the LDW process, and an ITO-PET film (60 Ω/sq, transmittance ~79% at 550 nm, Sigma- Aldrich) was used as a counter electrode. Two slips of copper tape were attached to the top and bottom sides of the ITO-PET film, with another two slips to the left and right sides of the Ni grids. The active area was 3 cm 3.7 cm. A commercial USB-interface touch screen controller was connected to the four copper electrodes with electric wires through which the voltage was applied and converted the voltage drop signals into the letters on a PC screen. No protective coating layer was required for the Ni electrodes due to strong adhesion on the substrate. The performance of the Ni touch screen pad was evaluated as displayed in **Figure 4.14(c)**.

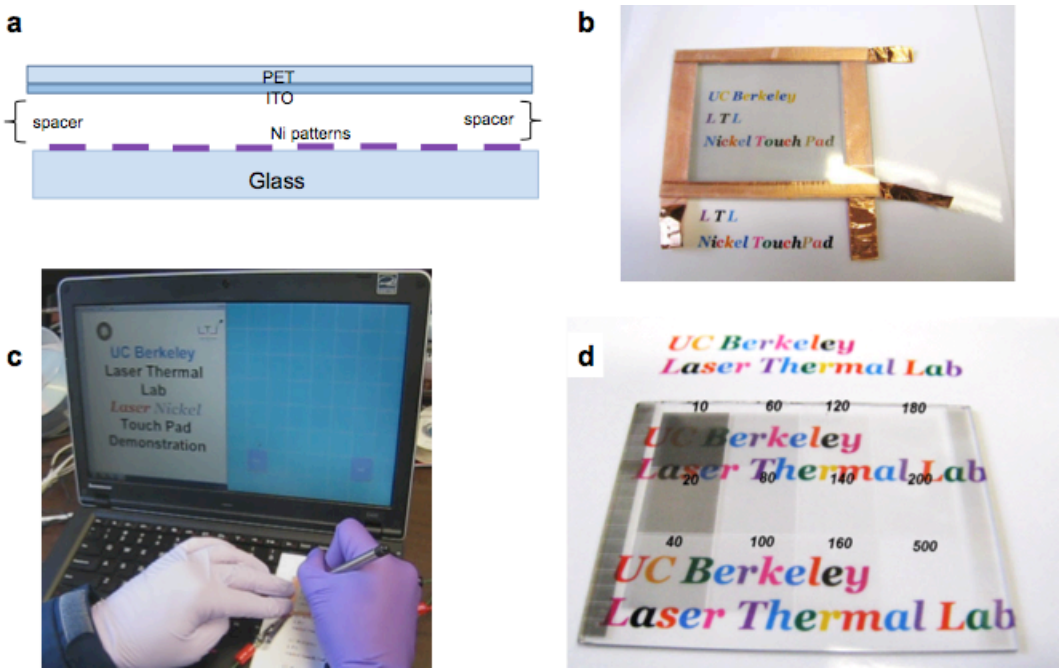

Figure 4.14 (a) Schematic diagram of a touchscreen panel. (b) Photoimage of a 4-wire resistive touchscreen panel. (c) Demonstration of operating Ni touchscreen panel (active area: 3 cm × 3.7 cm) by writing "UCB LTL" with a stylus pen. (d) Photoimage of several 1cm × 1cm mesh patterns. The number indicates the corresponding pitches of the mesh patterns.

Chapter 5. Fabrication of flexible transparent electrodes by nanosecond laser ablation

5.1 Overview

Flexible transparent conducting electrodes (FTCEs) are indispensable components in optoelectronic devices, including touch screen panels (TSPs),[17] organic photovoltaics (OPVs),[102] and organic light-emitting diodes (OLEDs).[103, 104] For such devices, indium tin oxide (ITO) has been the most widely used transparent conducting material, since it offers relatively high transmittance (> 80 %) with low sheet resistance (~15 Ω sq^{-1}) on a flexible substrate. However, great demand for alternative solutions has arisen due to ITO's several intrinsic drawbacks.[105] ITO is not suitable for flexible electronics, since its brittleness causes cracks upon bending. Also, indium is a rare earth material, resulting in the relatively high material cost of ITO. Furthermore, the conventional ITO sputtering is a slow deposition rate process of large material waste.[106]

In view of the above mentioned shortcomings of ITO, many researchers have investigated alternative materials such as carbon nanotubes (CNTs),[107, 108] graphene,[109, 110] doped zinc oxide (ZnO) based transparent conductive oxides (TCOs),[111-113] metal (Ag, Cu) nanowires (NWs),[114, 115] metal microgrids,[116] and graphene-silver nanowire hybrid materials[117] for FTCEs. However, carbon-based nanomaterials such as CNTs or graphene exhibit relatively poor optoelectronic performance compared to ITO.[118] Doped ZnO based TCOs are attractive alternatives for the replacement of ITO. Various materials such as Ga, In, Al, and F can be doped to enhance the mobility of ZnO. Especially, *Papadopoulou et al.* reported an Al- doped ZnO (AZO) film on a glass substrate with the transparency of 85 % and the sheet resistance of ~15.2 Ω sq^{-1} For AZO on a flexible polymer substrate, *Girtan et al.* reported the similar optoelectronic properties of the transparency of 85 % with ~34.9 Ω sq^{-1} sheet resistance, which is comparable to ITO without inherent drawbacks of ITO.[111] Recently, Ag NWs achieved transparency of 95 % with sheet resistance of 20 Ω sq^{-1} which surpasses the ITO performance.[119] Ag NWs can be deposited on a flexible substrate by spin-coating or vacuum transfer. Due to the satisfactory performance and easy processing, industry has already commercialized Ag NW based touch sensors. However, the high material cost of silver presents a challenge to the mass production of optoelectronic devices. Copper is an attractive material for FTCEs, 90 times cheaper than Ag with similar electrical conductivity (Ag: 6.3×10^7 S/m, Cu: 5.96×10^7 S/m) with interband transition of d-orbital electrons in visible wavelength for Cu as shown in the **Figure 5.1**.

The best performance of Cu NWs was reported as 95 % transparency with 100 Ω sq^{-1} In order to further improve the performance by minimizing oxidation during the Cu NW annealing process, fast plasmonic nanowelding of Cu NWs, as well as application of Cu (core) - Ni (shell) NWs,[120] and surface-embedded Cu NW network structures for oxygen passivation were proposed. However, the metal NW based approach requires material synthesis and post processing annealing steps. Another route would be utilizing metal films compatible with conventional semiconductor fabrication processes. Since metal films thinner than the light absorption depth become transparent though still conductive, metal grid fabrication methods via nanoparticle sintering and sphere lithography[121] have been demonstrated for transparent electrodes. In order to realize FTCEs, metal grids should be established on flexible substrates that are sensitive to heat and have restrictions in terms of chemical treatment. In this regard, *Kwon et al.* demonstrated Ag nanoparticle (NP) sintering combined with sphere lithography to obtain metallic honeycomb structures on a PET substrate, achieving transparency of 83 % with

sheet resistance of 20 Ω sq^{-1}. However, there is a strong need for a new technology applicable to cheaper materials such as Cu.

Cu FTCEs were produced by nanosecond (ns) laser ablation under ambient conditions, achieving substantially better performance (sheet resistance: 17.48 Ω sq^{-1}, transmittance at 550 nm: 83 %) than commercial ITO film. The ns laser ablation of ultrathin copper films enabled material removal without inflicting thermal damage on the underlying flexible polymer substrates. As a result, metallic honeycomb structures were directly produced on various heat sensitive flexible substrates such as polyethylene naphthalate (PEN), polycarbonate (PC), and polyimide (PI). The electrical performance of Cu FTCEs was maintained even after bending, squeezing, and twisting tests. In addition, a touch-screen panel was demonstrated.

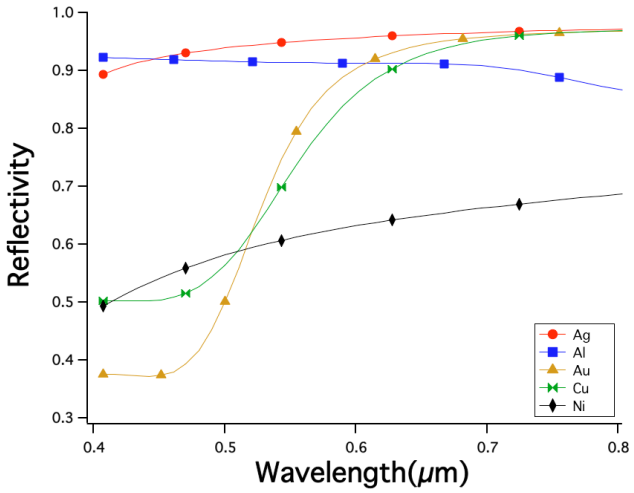

Figure 5.1 Reflectivity of various metals in the visible wavelength range

5.2 Ablation of ultra-thin copper film

Figure 5.2(a) shows schematics of the fabrication process of Cu FTCEs. Upon irradiation of ns laser pulses (532 nm), a circular hole array was produced in a 19 nm thick copper film on a flexible polymer substrate, resulting in higher transparency while maintaining the good electrical conductivity of copper. On a flexible polymer substrate, 19 nm-thick Cu film and 0.2 nm thick chromium (Cr) adhesion layer were deposited by electron beam evaporation. Commercially available various polymer substrates were examined as-received. PEN (Teonex Q65FA, Teijin Dupont, thickness: 125 μm) substrate was used throughout this study as received without any treatment. The direct laser writing process enables simultaneous patterning of the Cu FTCE. The deposited Cu film was irradiated with a diode pumped Nd: YVO_4 laser at the wavelength of 532 nm that was generated by a second harmonic crystal. The pulse repetition rate was 1 kHz and the full-width-half-maximum (FWHM) pulse duration was 22.7 ns. The Gaussian laser beam was focused with a 10× infinity corrected objective lens, and the $1/e^2$ beam diameter was 4.7 μm. Furthermore, laser fluence was controlled by adjusting the half-wave plate in front of the polarized beam splitter, and the average laser power after the objective lens was measured by a

power meter. A single laser pulse was irradiated on each ablation spot by controlling the translation speed of the motorized stages.

Figure 5.2(b) shows the light emitting diodes (LEDs) attached on a Cu FTCE. Since the Cu FTCE was simultaneously patterned during the laser ablation, the LEDs serially interconnected across the patterned regions (presented with orange color as illustrated in the inset) were turned on, indicating the patterned region was electrically isolated. In addition, **Figure 5.2(c)** shows a photograph of a simultaneously patterned Cu FTCE by taking advantage of high-resolution direct laser writing. Optical microscope and scanning electron microscope (SEM) images are shown in **Figure 5.2(d)-(e)**. Interestingly, no structural deformation and damage that are detrimental to the optical characteristics were observed, even though the temperature field induced during the melting and ablation process should have exceeded the glass transition temperature of the flexible polymer substrate. Furthermore, atomic force microscopy (AFM) image shows that the height difference between the film and the ablated spot center is 25 nm, indicating that a 6 nm deep trench was formed in the substrate upon laser pulse irradiation. In addition, the rim edge of the ablated hole is around two times thicker than the original film, suggesting outward radial mass transfer of molten metal.

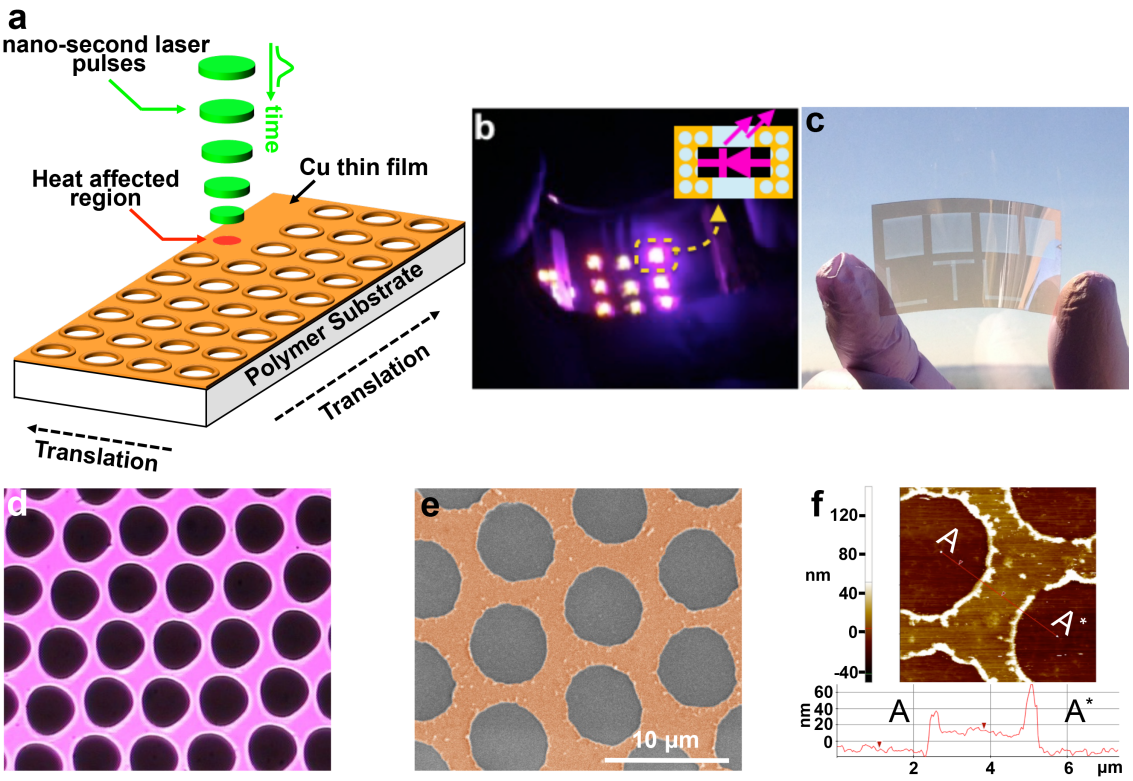

Figure 5.2 (a) Fabrication schematics of Cu FTCEs. (b) Optical image of a 3×3 LED array on fabricated Cu FTCEs (c) Optical image of fabricated rectangular patterns on ultrathin Cu films with different areal densities of 0.68, 0.62, 0.52 and 0.4, respectively, from left to right. A word "LTL" shows the patternability of Cu FTCEs. (d)-(e) Optical, SEM and AFM images of the Cu FTCEs.

Since the electron-phonon relaxation time for metals is in the order of a few picoseconds, the ns laser ablation is fundamentally a thermal process that goes through the melting phase transition. Ablation of several μm-thick metal layers typically produces abundant debris and rough surface morphology due to melt surface instability and expulsion. Excessive roughness may result in poor contacts and electrical shorts in optoelectronic devices. In contrast, ns laser ablation of very thin (19 nm) Cu film suppresses the surface roughness and produces clean features. The optical penetration depth, l_α, of copper (532 nm) is 17 nm, while the estimated transverse heat diffusion length in the copper layer, $l_{T,Cu} \sim 2\sqrt{\alpha_{Cu}\tau_l}$, is 3.17 μm (α_{Cu}: 1.11×10^{-4} m^2/s (thermal diffusivity of bulk Cu at 25 °C), τ_l: 22.7 ns (FWHM pulse duration)). The vertical heat diffusion depth into the substrate, $l_{T,Sb} \sim 2\sqrt{\alpha_{sb}\tau_l}$, is about 0.1 μm for the PC (α_{sb}: $1.44\text{x}10^{-7}$ m^2/s (thermal diffusivity of PC at 25 °C)). Since the thickness of the Cu film was slightly thicker than the optical penetration depth (l_α), the laser light energy was efficiently absorbed in the Cu film. In addition, the limited heat dissipation into the thermally poor conductive substrate lowered the laser ablation threshold fluence. Utilizing a simple thermal model, *Matthias et al.* suggested that the laser ablation threshold fluence varies linearly with the film thickness, d, when d is in the range $l_\alpha < d < l_{T,Cu}$.[122]

F**igure 5.3(a)** displays the relationship between the measured ablated spot radius, r_a, and the laser fluence, F. For a Gaussian laser beam profile, the relationship can be expressed as

Equation 5.1 Ablation threshold

$$r_a^2 = r_f^2\left[\ln(F) - \ln(F_{th})\right]$$

where r_f is the beam radius, and F_{th} is laser ablation threshold. The ablation threshold (F_{th}) was estimated as 59.8 mJ/cm^2, which is 10 times smaller than the ablation threshold of thick copper. **Figure 5.3(b)-(d)** show SEM pictures of ablated holes at different laser fluences. Even though the melting temperature of Cu (1085 °C) is much higher than the melting temperature of the polymer substrate (i.e. 155 °C for PEN) negligible substrate damage was observed in these images, due to the shallow heat-affected zone into the substrate and the fast heat removal by ejection of the molten Cu. At the low laser fluence of 190 mJ/cm^2 (**Figure 5.3(b)**), condensed and re-solidified Cu nanoparticle clusters were found within the hole, as the weak momentum of the ejecta could not overcome the ablation plume confinement by the ambient air background. However, at higher laser fluences (**Figure 5.3(c)-(d)**), nanoparticle clusters were found only near the peripheries of the holes due to the stronger melt expulsion and ablation. The hole rim height is ~ 50 nm at the laser fluence of 1.35 J/cm^2, which is two times thicker than the original thickness of the film, indicating capillarity driven radial flow of dewetted molten Cu.

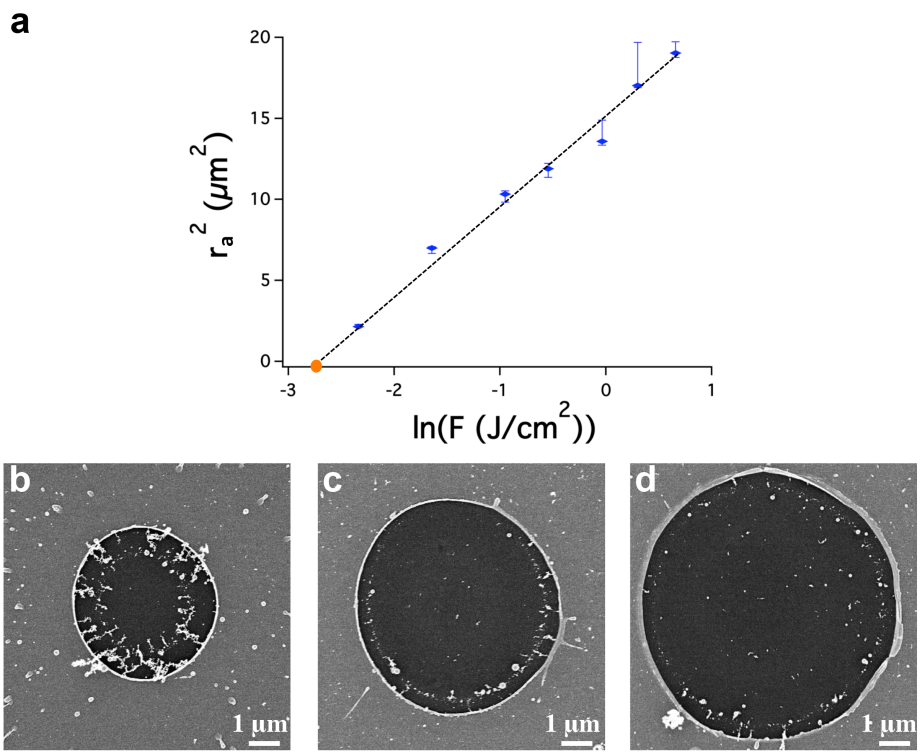

Figure 5.3 (a) Square of ablation radius *versus* logarithm of laser fluence (● denotes the logarithm of the ablation threshold). (b)-(d) High magnification SEM images of ablated holes (laser fluence: 190 mJ/cm^2 (b), 580 mJ/cm^2 (c), 1930 mJ/cm^2 (d))

5.3 Opto-electronic performance analysis

The transmittance of the Cu FTCEs can be controlled by synchronizing the pulse repetition rate and the translational speed of the motorized stages. **Figure 5.4(a)** shows the transmittance at different areal densities. Areal density is defined by the ratio of the residual area after ablation to the total area. As-prepared Cu film (areal density = 1) yielded transmittance of 62 % at the wavelength of 550 nm, while the maximum transmittance of 83 % was achieved when the areal density was 0.4. **Figure 5.4(b)** displays a plot of transmittance at 550 nm (T) *versus* sheet resistance (R_s) for Cu FTCEs, where reference data sets are taken from the recently reported Cu NW based TCEs. These Cu FTCEs exhibited superior opto-electrical performance of T = 83 % and R_s = 17.48 Ω sq^{-1} compared to other Cu NW based TCEs. This improvement is attributed to the structural integrity of the Cu films, which eliminates the need for post-annealing steps that were for example required in the Cu NW based TCEs. The FTCE performance can be quantified by the bulk and percolative figures of merit (FoM), Π_{bulk} and $\Pi_{percolative}$, respectively. Recently, *De et al*. proposed a simple model that correlates the transmittance, T, and the sheet resistance, R_s, in the bulk and percolative regimes:[123]

Equation 5.2 opto-electronic figure of merit (bulk)

$$T = \left(1 + \frac{Z_0}{\Pi_{bulk} 2R_s}\right)^{-2}$$

Equation 5.3 opto-electronic figure of merit (percolative)

$$T = \left(1 + \frac{1}{\Pi_{percolative}} \left[\frac{Z_0}{R_s}\right]^{1/(n+1)}\right)^{-2}$$

where Z_0 is the impedance of free space (377 Ω) and n is the percolation exponent. **Figure 5.4(c)** displays corresponding R_s and T data at different areal densities. By fitting the data to **Equation 5.2**, we confirmed that our Cu FTCEs operate in the bulk regime. The Π_{bulk} of our Cu FTCEs (T = 83 %, R_s = 17.48 Ω sq^{-1}) is calculated as 109.74, which is *higher* than other reported Π_{bulk} values of Cu NW based transparent conductors. Laser beam shaping can be implemented to further decrease the areal density and push the Cu FTCEs well into the percolative regime, where optimal performance is often sought. In **Figure 5.4(c)**, we estimated the opto-electrical behavior of Cu FTCEs in the percolative regime. Transparency of 90 % with low sheet resistance of 42.1 Ω/□, was estimated with $\Pi_{percolative}$ = 48, n = 1.3, used as parameters. It is worthy to note the opto-electrical performance at two different regimes - i) the obtained in the bulk regime (T = 83 %, R_s = 17.48 Ω sq^{-1}, Π_{bulk} = 109.74) and ii) the estimated in the percolative regime (T = 90 %, R_s = 42.1 Ω sq^{-1}, $\Pi_{percolative}$ = 48, n = 1.3) - is comparable to or even better than the state-of-the-art Cu NW based transparent conductors.

5.4 Durability test

We subjected the Cu FTCEs to bending (bending radius (r_b): 3 mm), folding and squeezing tests. For the bending tests, tensile and compressive stresses were induced. In both cases, the bending strain, ε = 2.1 %, by $\varepsilon = t_s/(2r_b)$, where t_s is the substrate thickness (125 μm), was induced.[124] **Figure 5.5(a)** shows cyclic bending test on our Cu FTCEs. The relative resistance variation ($\Delta R/R_o$) was maintained within 1 % and mechanical failure was not observed even after 1600 bending cycles, which signifies the mechanical reliability of Cu FTCE and its excellent strength to bending fatigue. $\Delta R/R_o$ under 1% when $\varepsilon \approx$ 2.1 % during cyclic bending is comparable to that of a-ITO/PI film, which is reported by *Jung et al.* recently. **Figure 5.5(b)** compared the $\Delta R/R_o$ of commercial ITO-PEN films (~15 Ω sq^{-1}, T: 80% at 550 nm) versus Cu FTCEs at varied curvatures, κ (= $1/r_b$). At the curvature of 0.33 mm^{-1} (r_b = 3 mm, ε = 2.1 %), the resistance was 12 times higher compared to the initial resistance of the ITO-PEN film and abundant cracks were found on the surface, although the resistance change of the Cu FTCEs was negligible. **Figure 5.5(c)** shows stable electrical performance upon extreme bending, folding and squeezing events, implying robust structural integrity of these Cu FTCEs. **Figure 5.5(d)** shows that the sheet resistance was 19.35 Ω sq^{-1} after 14 hours of thermal aging test on a hot plate at 80 °C (7.5 % increase from the initial 18 Ω sq^{-1}). We expect Cu FTCEs can maintain good electrical performance without immediate degradation, even at elevated temperatures. Furthermore, a long-term oxidation stability test at ambient conditions revealed no drastic change in electrical performance after about one month (inset of **Figure 5.5(d)**).

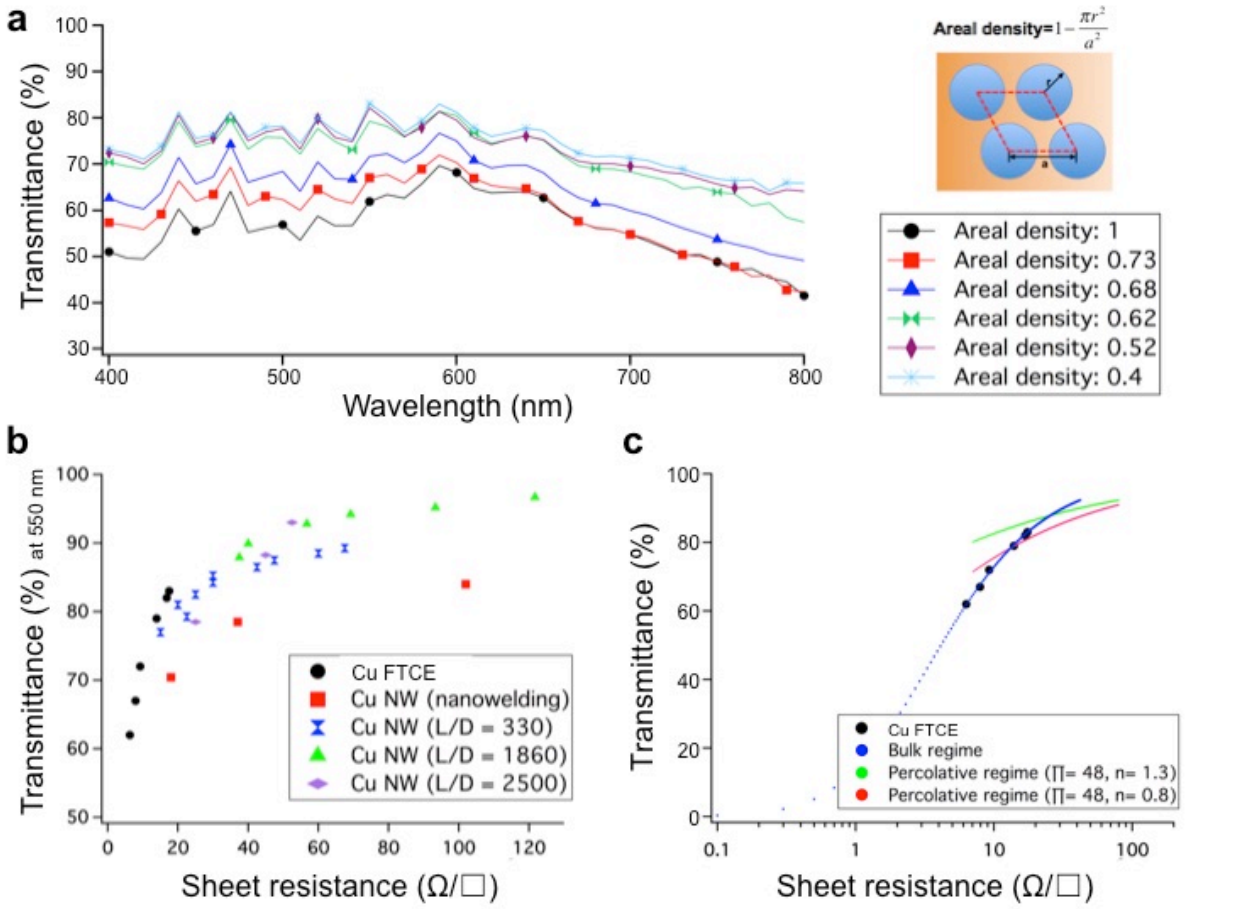

Figure 5.4 (a) The transmittance spectra of Cu FTCEs with different areal density. (b) Plot of sheet resistance *versus* transmittance at 550 nm wavelength of Cu FTCEs and other Cu NWs based transparent conductors. (c) Transmittance at 550 nm wavelength *versus* sheet resistance and fit to the bulk regime using **Equation 5.2** (●), while green and red dots represent the simulated opto-electrical behaviors at percolative regime using **Equation 5.3** (●: $\Pi_{percolative} = 48$, $n = 1.3$, ●: $\Pi_{percolative} = 48$, $n = 0.8$).

5.5 Touch screen panel application

We demonstrated a touch-screen panel (TSP) using the Cu FTCEs in **Figure 5.6**. By the same approach, a transparent conducting Cu electrode of 40 mm × 35 mm size on a glass substrate (45 mm × 45 mm) was produced for the 4-wire resistive touch-screen panel with ITO-PEN film used as a counter electrode. No protective coating layer such as PEDOT: PSS was required for the transparent Cu electrode, due to strong adhesion on the substrate. Due to the transparency of the electrodes, the colored letters on the LCD screen are visible. The functionality of the TSP is confirmed by writing the letters "UCB LTL" on the TSP, as shown in **Figure 5.6(b)-(c)**. It is noted that this demonstration used just a 1kHz laser and pulse energies in the range of just 10 µJ. The speed of the process could be substantially increased by adopting higher pulse repetition lasers and multiple focusing lenses. A 5.44 in×4.64 in touch screen panel can be fabricated within 2s using an array of 100 micro-lenses, a laser at 1 MHz pulse repetition and 10 m/s sample translation speed to write the 10 µm pitch patterns.

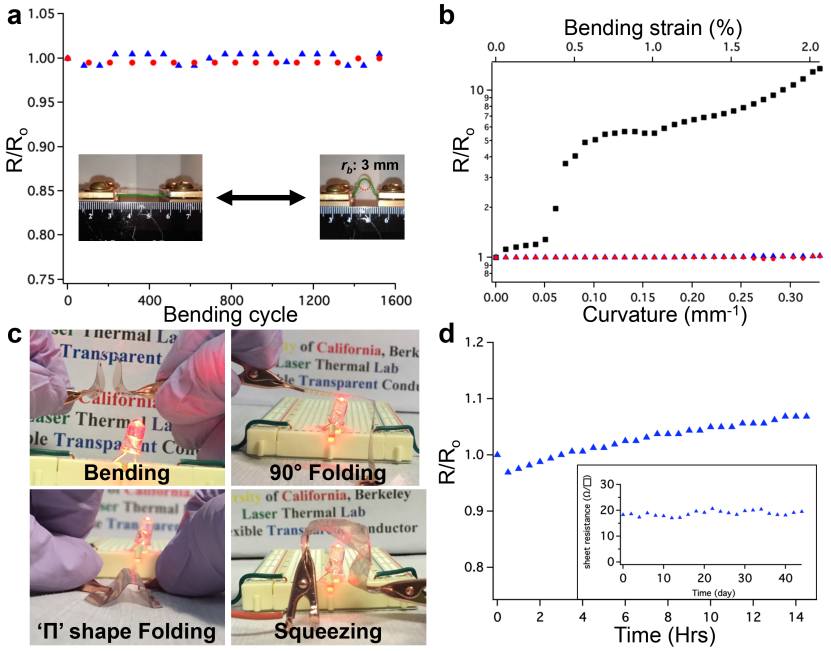

Figure 5.5 (a) Measured relative resistance variation (R/R_o) during the cyclic bending test. (b) Comparison of R/R_o between ITO-PEN film (■) and Cu FTCEs (tensile bending: ▲, compressive bending: ●) with the different curvature. (c) Mechanical durability test with bending, folding and squeezing with bare hands. (d) Thermal oxidation stability of electrical performance of Cu FTCEs at elevated temperature of 80 °C (Inset shows the long-term oxidation stability at ambient conditions).

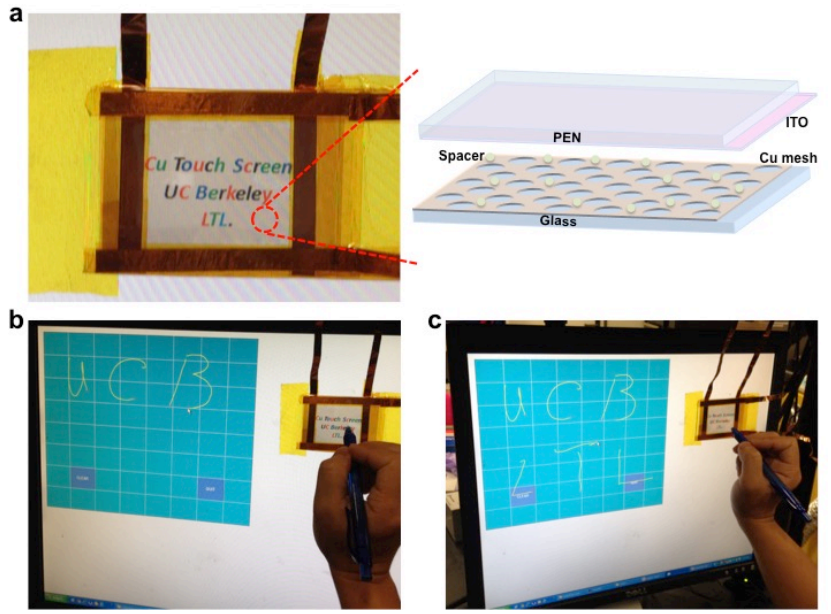

Figure 5.6 (a) Touch screen panel (TSP) attached on a LCD monitor and the schematics of a TSP (Green spheres are spacers). (b)-(c) Demonstration of the TSP operation fabricated by Cu FTCEs and ITO-PEN film. "UCB LTL" was written on the TSP

Chapter 6. Time resolved imaging of laser induced dewetting

6.1 Overview

Arrays of micron- or nano-sized holes in metallic films exhibit local field enhancement, strong plasmonic response, and high electron emission.[125, 126] During the last decade, such structures have attracted growing interest, owing to promising applications in optoelectronics[127] as well as other fields.[128] Direct laser ablation and dewetting is an interesting method for machining holes in thin and ultrathin metallic specimens. Compared to conventional photolithography that is combined with reactive ion etching or chemical etching, nanosecond laser[129] irradiation has showed advantages in terms of its non-contact and one-step characteristics, low cost, and flexibility with respect to the target material. By tuning the incident laser power, it is possible to machine holes of different dimensions and shapes on metallic surfaces.[130]

Fundamental understanding of laser-induced dewetting and ablation processes is important in order to enable improved prediction and optimization of laser processes.[131] Several optical probing techniques have been developed for studying laser-material interactions.[132, 133] For example, time resolved shadowgraphy has been utilized to directly observe the ablation process in the nanosecond time regime,[134-136] capturing the ejected plume and shockwave emission at certain delay times.[137] Nevertheless, even in the simplest case of metal films, the induced phase change and the ensuing dewetting and ablation processes have not yet been fully investigated.

6.2 Experiments

We selected silver as the sample of interest because of its well-known and stable properties as well as its use as electrode material in electronics. Silver thin films of different thicknesses (50, 80, and 350 nm) were prepared by electron beam evaporation on quartz substrate. The time-resolved imaging system was set up as shown in **Figure 6.1(a)**. Nd:YAG laser pulses of 532 nm wavelength and 5 ns temporal width impinged on silver film targets. The laser beam was focused by a 2× infinity corrected, non-achromatic long working distance objective lens at normal incidence. Nanosecond flashlamp (NANOLITE KL-K flash lamp, flash duration = 7 ns) was employed as an illumination source to provide temporally resolved images. These images were captured by a charge coupled device (CCD) camera via a 20× infinity objective lens. A digital delay generator was used to control the delay time between the processing laser and the image acquisition. The oscilloscope was used to record the actual delay time of the processing laser signal and the flash lamp signal. To ensure true representation, at least six images were examined at each delay setting. We estimated the ablation threshold fluences of each film by linear curve fitting as shown in **Figure 6.2**. Above the ablation threshold fluence, F_{th}, the relationship between the ablated spot radius, r_a, and the laser fluence, F, is well characterized by a Gaussian beam profile, as shown in **Equation 5.1**. For different thickness silver films (50, 80 and 350 nm), the ablation thresholds were estimated as 0.92, 2.59, 8.45 J/cm^2, respectively.

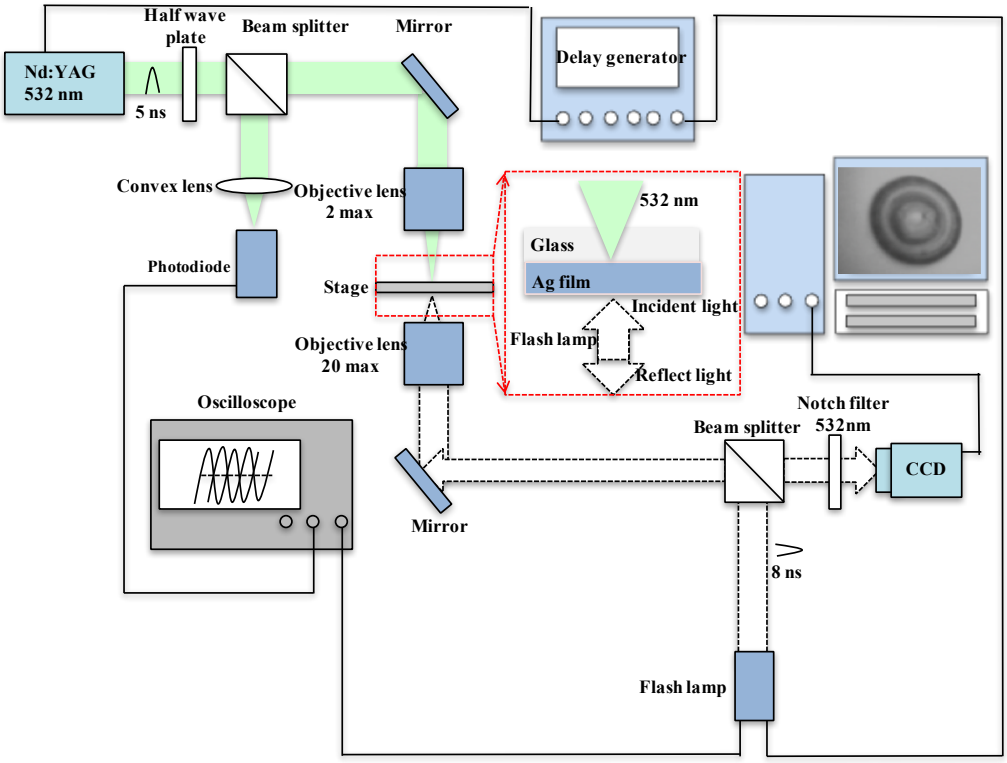

Figure 6.1 Time-resolved image setup of dewetting/ablation induced in silver by a Nd:YAG laser pulse with 5 ns duration, and the red frame is the magnified optical set-up image near the stage.

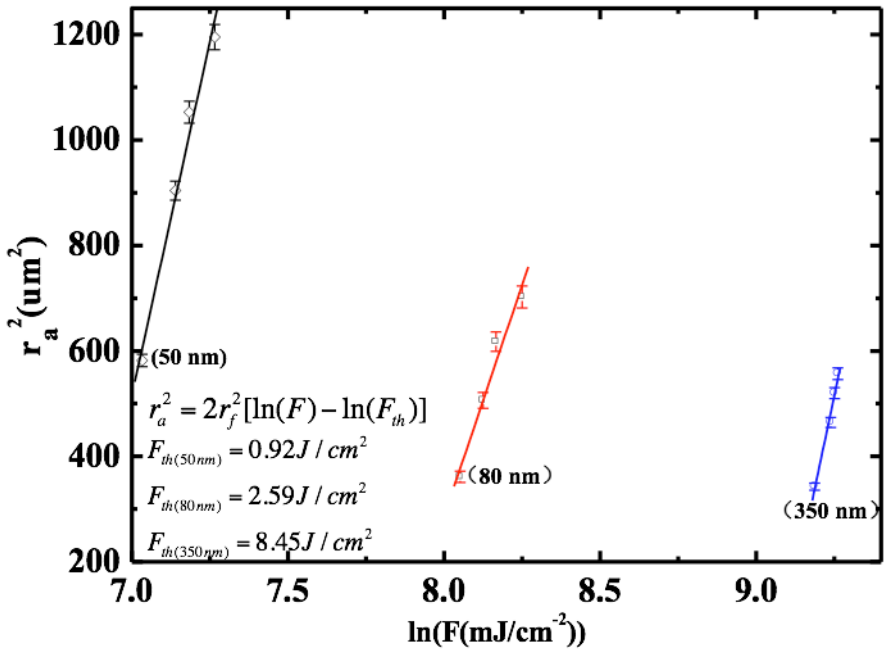

Figure 6.2 Squared radius of the ablation areas, with different thickness versus natural logarithm of the pulse fluence

6.3 Surface morphologies and time resolved imaging analysis

Next, we focus on investigating the surface morphologies produced by the exposure of the Ag films to near ablation threshold fluences. **Figure 6.3(a)** presents optical dark-field images, SEM images, and time-resolved images of the 50 nm Ag film surface. For low laser fluence below 0.89 J/cm^2, droplet-like structures are formed in the central area, implying melting and dewetting. As the fluence increases, the central droplet-like structures disappear, and melted material is dewetted radially outward. For the thicker samples (80 nm and 350 nm), as shown in **Figure 6.3(b)-(c)**, droplet-like structures can also be formed upon irradiation at fluences of 2.31 J/cm^2 and 7.71 J/cm^2, respectively. At higher laser fluences, peripheral rims and droplet fingers appear in the outskirts of the holes.

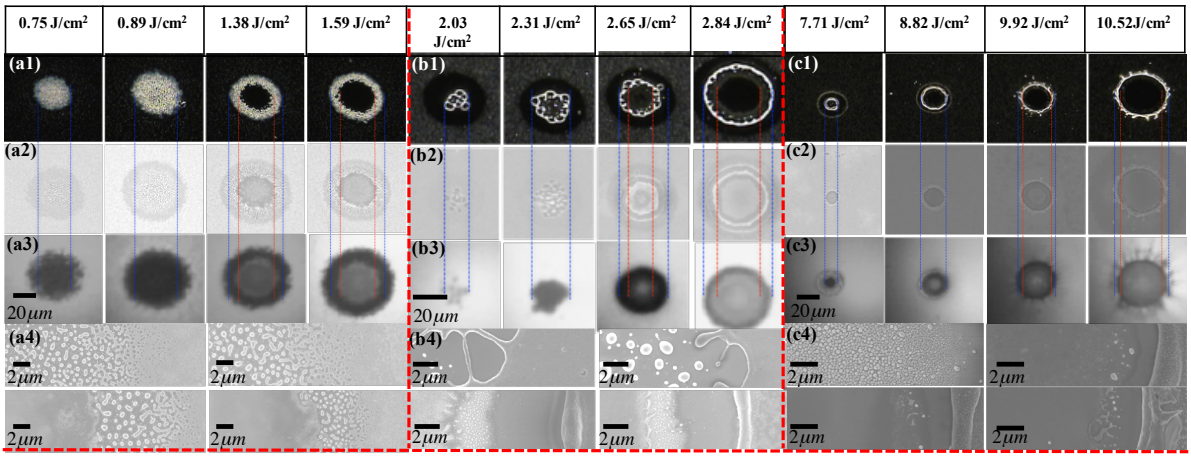

Figure 6.3 Optical dark-field images (a1)-(c1), scanning electron microscopy (a2)-(c2), time-resolved images with 600 ns delayed (a3)-(c3), and the magnified SEM images (a4)-(c4) are corresponding magnified SEM images of figures (a2)-(c2) and give detailed information of edges between ablation and dewetting zones. (a) 50 nm, (b) 80 nm, (c) 350 nm thickness Ag film. The red dashed lines mark the ablation edges and the blue dashed lines the dewetting edges of each sample.

The transient evolution of the film surface morphologies at selected laser fluences are recorded using the time resolved imaging setup and presented in **Figure 6.4**. As previously mentioned, micron-sized droplet-like particles are formed at lower laser fluences, i.e., around 0.89 J/cm^2 for the 50 nm film and 2.31 J/cm^2 for the 80 nm film. The time resolved images at the corresponding laser fluences in **Figures 6.4(a)** and **6.4(b)** indicate that shiny small particles appeared in the central area of the irradiated zone at times of 200 ns and 500 ns after the laser irradiation, presumably formed by Ostwald ripening.[138] Furthermore, since micron-sized metallic particles of size parameter ($\chi=\pi D/\lambda$), where D is the particle diameter and λ the probing wavelength, scatter radiation strongly in the forward direction and yield much weaker back-scattering, the central area appears dark in reflection images beyond an elapsed time of 630 ns, signifying aggregation to bigger micron-sized particles. At slightly increased laser fluence, holes with droplet-like or cylindrical rim structures around these edges are formed on the silver film surface, respectively. At higher fluences, i.e., at and above 1.38 J/cm^2 for the 50 nm thickness specimen, the dewetted material is pulled toward the edges of the holes forming peripheral

droplet-like structures after an elapsed time of 700 ns. For the 80nm thick sample, rim structures can also be formed if the laser fluence is at or above 2.31 J/cm2. For the 350 nm thick sample, several distinct stages in **Figure 6.4(c)** is observed at different laser fluences. Evidence of ablation in the center and dewetting in the edge area is observed at the laser fluence of 8.82 J/cm^2 that is slightly higher than the ablation threshold of 8.45 J/cm^2. At the higher laser fluences of 9.92 J/cm^2 and 10.52 J/cm^2, radially outward droplet fingers are observed.

Figures **6.5(a)–(c)** depict the SEM images of Ag thin films for different laser fluences, where the dewetting and ablation edges are distinct. **Figure 6.5(d)** gives the schematic diagram of ablation and dewetting distribution for 50 nm thickness sample under different laser fluences. If the laser fluence (red curve) exceeds the ablation threshold, the central ablation area (blue line) surrounded by the dewetting zone (green line) appears. The dewetting regime (green line) solely appears in the spot center if the laser fluence (blackcurve) is below the ablation threshold.

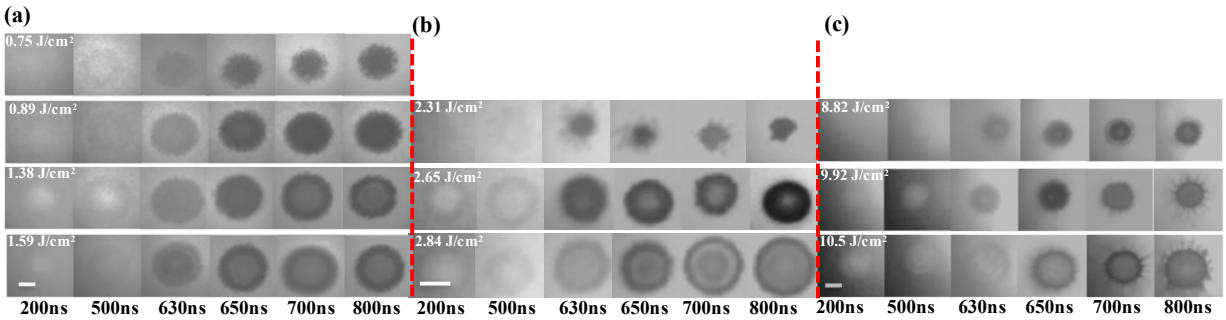

Figure 6.4 Time resolved image series of ns laser dewetting/ablation of silver films with different thickness: (a) 50 nm, (b) 80 nm, and (c) 350 nm. Each frame was taken at a certain flash lamp delay time. The scale bars in these images are all 20 μm.

Figure 6.6 depicts distinct stages of the thin film modification process and the corresponding ablation and dewetting threshold, respectively. If the laser intensity in the spot center is below the ablation threshold, in the dashed line region, the nanosecond laser pulse causes local dewetting of the Ag layer in the spot center.[139, 140] In this case, nanoparticles grow larger through Ostwald ripening, wherein the larger particles scavenge smaller ones, broadening the size distribution in the dewetting area after an elapsed time of 650 ns for all the samples (**Figure 6.5(a)**). If the laser fluence exceeds the respective ablation threshold of each sample, the SEM and time-resolved images of 50 nm sample show ablative material removal in the spot center and the formation of droplet-like particles in the peripheral dewetting zone after an elapsed time of 700 ns (**Figure 6.5(b)**). Rim structures are then formed in the 80 nm and 350 nm thick samples after laser irradiation (**Figure 6.5(c)**). It is recalled that the surface temperature is higher at the center of the melt pool, and the absorbed energy induces surface tension driven flow due to the high temperature gradient.[141] Consequently, due to the diminishing surface tension with increasing temperature for liquid metals, material should be transported radially outward by the positive surface tension gradient. However, the 50 nm film cannot supply significant mass transfer and only droplet-like particles are formed. Order of magnitude estimates for the 50 nm film and melt pool diameter of 60μm yield O(0.1 m/s) thermocapillary driven melt velocity that in turn corresponds to O(10^{-5} N) inertia force on the liquid pool.[54] On the other hand, estimates of the recoil force exerted on the melt pool for laser fluence in the

range of 1 J/cm2 yield O(10^{-1} N) values. Although the inertia force scales approximately with the square of the film thickness, it is still much smaller than the recoil force even for the 350 nm film. One may therefore expect that the thermal gradient driven surface flow is of minor consequence.[142-144] For the 350 nm thickness sample, as shown in **Figure 6.5(d)**, the ablated splashed droplets shoot off the surface at higher laser fluence (above 9.92 J/cm^2), exerting strong recoil force and producing droplet fingers (**Figure 6.5(d)**). For higher laser fluence, the liquid Ag materials are squeezed out of the pool very quickly by the diminishing surface tension and pushed around the peripheral rim structure. Droplet fingers occur due to the recoil force induced acceleration around the rim. The same experimental trends would be observed in thin films of different inorganic materials and comparable thickness. The effect of the wavelength is not particularly significant for the present experiments, as it affects merely the magnitude of the energy input into the film. However, the laser interaction with the ejected matter would depend on the laser wavelength. This is likely to be important at the higher fluences where the ablation is accompanied by the plasma effects and the problem becomes more strongly coupled due to the fluid dynamics and radiative transport in the ejected plume.

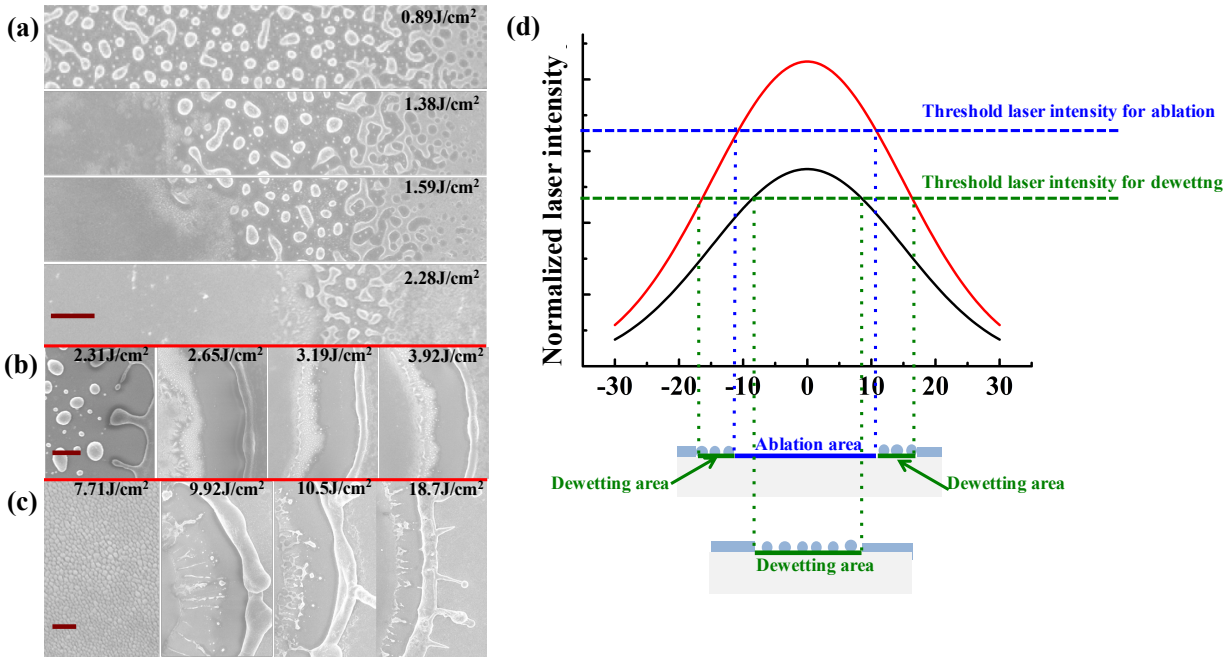

Figure 6.5 Different surface morphologies of the Ag thin films with different laser fluences ((a) 50 nm, (b) 80 nm, and (c) 350 nm). (d) Normalized laser intensities of the ablation and dewetting threshold on the Ag thin film (50 nm) and corresponding ablation and dewetting line widths. Absorbed laser light intensities are normalized by the peak intensities of red curve. The scale bars in the SEM images are all 20 μm.

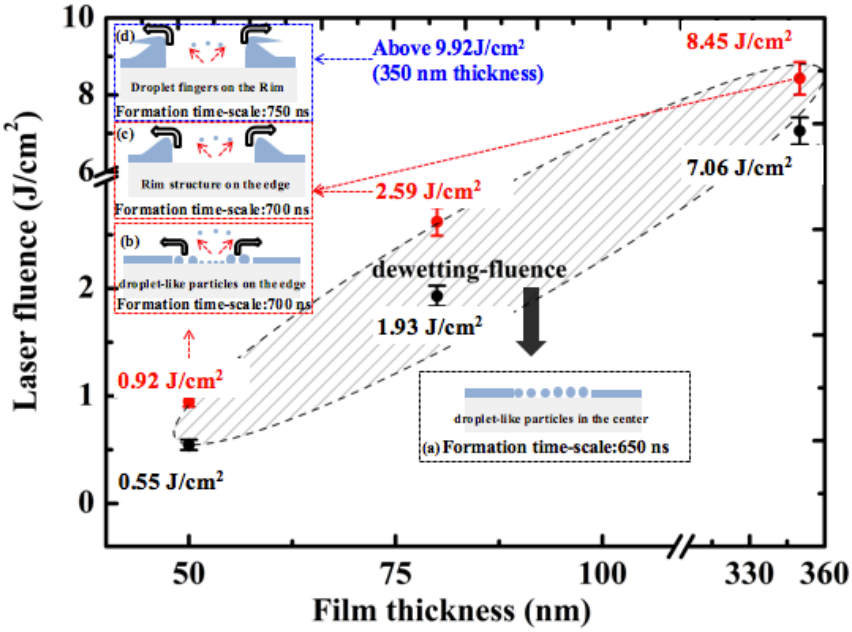

Figure 6.6 The black and red labeled numbers are the dewetting and ablation thresholds, respectively. The insets (a)-(d) give a schematic illustration of mechanisms responsible for nanosecond laser-induced formation of surface structures on thin silver films. The dashed line region marks the dewetting fluences. Ablative material removal occurs for laser fluence exceeding the shaded area range. On the other hand, dewetting happens when the laser fluence is in the shade area. If the laser fluence is lower than the dewetting threshold, no surface morphology changes are observed.

Chapter 7. Conclusions and Suggestions for Future Work

7.1 Concluding remarks

Recently, much progress has been made in flexible electronics field. FTCEs are crucial among many other key components in flexible devices. Conventional materials, including as-mentioned ITO and processes that are currently used in the flat panel display fabrication are not compatible with flexible electronics layouts. These limitations pose significant challenges in developing new facile fabrication schemes compatible with flexible platforms, such as low thermal budget (< 100 °C) and lightweight. Therefore, developing facile fabrication route of FTCEs with high opto-electronic performance will be a key technology for the future opto-electronic devices. Nanoparticle and laser are promising candidates in the fabrication of flexible electronics components.

In **Chapter 2**, the laser wavelength effect on the electrical properties and surface morphology of laser-sintered silver nanoparticle thin film was investigated. Fundamental optical and thermal properties of these films are examined since the laser sintering is in essence a photo-thermal process. From the TGA and DSC data, the onset temperature of sintering was deduced and thermal conductivities of pristine and sintered Ag NP thin films were estimated by applying the MG-EMA and W-F laws. The absorption coefficient and surface reflectivity were calculated from the measured complex dielectric functions. In addition, *ex-situ* resistivity measurements and scanning electron microscopy images were taken. Minimum resistivities of 5.7, 5.28 and 8.9 μΩ•cm were obtained for the NUV, green and NIR lasers, respectively. For the NUV and green lasers, which have the shallower optical penetration depths, surface melting morphologies were observed. Films processed by the NIR laser did not exhibit such features for the applied laser power range. In this case, the respective optical penetration depth is comparable to the thickness of the Ag NP thin film. Formation of large pores at the scanning speed of 40 mm/s could be explained by the lagged evaporation of trapped solvent and ligand release. Threshold laser powers for sintering were obtained as 8, 25 and 34 mW for the green, NUV and NIR laser, respectively. At given laser power, lines sintered with NUV laser were of the largest width while those sintered by the NIR laser had the smallest. This trend could be explained by considering the laser energy absorption within the Ag NP thin film and postulating the heat transport mechanism that drives the sintering process. Furthermore, the line width did not depend on the scanning speed in the range applied in the experiments, possibly due to the heat dissipation through the sintered Ag NP line, which should have thermal conductivity higher by three orders of magnitude compared to the pristine Ag NP thin film.

In **Chapter 3**, I quantitatively analyzed the characteristic coalescence times of Ag-PVA NC and Ag-PVP NPs by using optical probing techniques. Probing beams with two different wavelengths (405 nm and 633 nm) were employed to monitor the optical transmission response during CW laser irradiation. In the case of Ag-PVA NCs, three regimes are recognized: 1) particle formation, 2) diffusion and 3) coalescence. The particle formation time scale is ~1 ms. For the coalescence time, both Ag-PVA NC and Ag-PVP NPs thin films show similar timescale around 10 ms. Unlike these regimes, diffusion is the most time-consuming process and highly dependent upon the laser power density. Furthermore, the processing laser power densities for the Ag-PVA NCs are much higher than for the Ag-PVP NPs. For the Ag-PVA NCs, generated

silver nanoparticles should diffuse through the PVA matrix to be agglomerated while the host polymer matrix acts as an energy barrier for the diffusion of the nanoparticles.

In **Chapter 4**, the kinetics of laser-induced reductive sintering of non-stoichiometric NiO NPs was investigated. Laser irradiation offered a highly localized and fast heat source for the decomposition of the residual toluene solvent in the thin films that cannot be realized by conventional, slow thermal annealing. In addition, it facilitated the excitation of electrons from the valence band to the conduction band of the NiO_{1-x} NP. Protons produced as a result of the decomposition of toluene and electrons donated by the NiO NPs promoted the reduction process. Sintering of the Ni NPs thus formed was then initiated. The reductive sintering reaction was therefore identified as a sequential process comprising reduction and subsequent sintering. The NiO NPs in toluene, which served as the reducing agent in our study, constituted an efficient configuration for the reductive sintering process when combined with the selective heating enabled by the laser. Since the Ni NPs acted as absorption centers due to increased absorption, the reductive sintering reaction was accelerated for laser power densities exceeding the threshold P_{th}. Moreover, by exploiting optical and electrical property changes during the reductive sintering reaction, the reaction timescales could be measured in real time. *In-situ* measurement of the temporal evolution of transmittance, reflectance and electrical conductance unveiled four distinct regimes: oxidation, reduction, sintering and re-oxidation. Timescales were quantified for each regime. These diagnostics can be applied to reveal the kinetics of reductive sintering of other metal oxide NP systems. This study also showed that deliberate and precise manipulation of the light-material interaction was essential in order to achieve the desired electrical functionality. Furthermore, Ni electrode patterning and its application as a TSP is demonstrated by selective laser reductive sintering of NiO NP thin films. All procedures, from materials synthesis to the laser processing, were performed under ambient conditions without involving photolithographic steps. The resistivity of the Ni electrode is less than an order of magnitude higher compared to that of the bulk Ni. Cyclic bending, adhesion tests confirm robustness of the Ni electrodes on both plastic and glass substrates. By adjusting the pitch of the mesh-type thin electrode grids yields a transparent conductive panel showing a transmittance higher than 87 % and a sheet resistance of around 655 $\Omega\ sq^{-1}$.

In **Chapter 5**, Cu FTCEs were fabricated by a new laser direct writing approach incorporating simultaneous patterning. The ns laser ablation of an ultrathin metal film on a substrate of low thermal conductivity produced clean ablated spots. No damage or structural deformation of the flexible polymer substrate was observed. By optimizing the areal density, or producing monolithically interconnected percolation network of ultrathin Cu film, superior opto-electrical performance (T = 83 %, R_s = 17.48 $\Omega\ sq^{-1}$) was achieved with excellent mechanical durability, which is comparable to state-of-the-art Cu NW based flexible transparent conductors. We conclude that there is room for further improvement in opto-electrical performance based on the figure of merit estimation. Finally, a touch screen panel was demonstrated to confirm potential applicability of Cu FTCEs as a flexible optoelectronics platform. We believe that low-cost and relative easy to fabricate Cu FTCEs offer a realistic substitute for the replacement of ITO and Ag NWs in flexible optoelectronic devices.

Lastly in **Chapter 6**, I have provided visual evidence for time scale by which nanosecond laser-induced dewetting and ablation processes in silver film. Due to the high temporal resolution

of the imaging setup, time-scale for the generation of the droplet-like particles, cylindrical rim and plume structures are studied in detail. This time-resolved image setup is a powerful tool for the study of fundamental laser-materials processing mechanisms, and for making time-scale and morphology measurements of the effects of laser conditions and materials on the laser-materials process.

7.2 Suggestions for future studies

7.2.1 Beam Shaping for high transmittance FTCEs

In **Chapter 5**, I introduced a novel nanosecond laser-assisted fabrication of flexible transparent conductors. Even though it shows a very high optoelectronic figure of merit(FoM) in the bulk regime, the maximum transmittance achieved was 83%, which is lower than that of the state-of-art NW-based transparent conductor. Its electrical conductivity was much higher than that required for commercial touchscreen panels. The FoM analysis in **Chapter 6** revealed that most NW-based transparent conductors work in the percolative regime. Thus, it is expected that our FTCE can work in the percolative regime by lowering the fill factor using beam modulation. To enable percolative regime operation, we employed diffractive optics. The overall process is shown in **Figure 7.1**.

As-received PEN (Teonex Q65FA, Teijin Dupont, thickness: 125 μm) substrate was used in this study. A 25-nm thick silver film and a 0.2-nm thick chromium (Cr) adhesion layer were deposited to the flexible polymer substrate by electron beam evaporation. The deposited Ag film was irradiated with a diode that pumped an Nd: YVO_4 laser at a 532-nm wavelength generated by a second harmonic crystal. The pulse repetition rate was 1 kHz, and the duration of the full width at half maximum pulse was 22.7 ns. The laser fluence was controlled by adjusting the half-wave plate in front of the polarized beam splitter, and the average laser power was measured by a power meter. The diameter of the Gaussian laser beam was then expanded by two singlet lenses with different focal lengths. After passing the beam expander, the Gaussian beam was modulated to a flat-top square beam and focused to 30 × 30 μm. A single laser pulse was irradiated on each ablation spot by controlling the translation speed of the motorized stages. The inset in **Figure 7.1** shows an optical image of the Sather Tower at the University of California, Berkeley through the bare PEN (1), silver film before the laser (2), and laser-processed silver film (inside the 2).

Interestingly, flat-top square-beam laser processing was proven to be able to suppress the dewetting region and thus minimize the difference in the thickness at the rim. **Figure 7.2** shows a comparison between the Gaussian beam and the flat-top square beam in laser processing. As shown in **Figure 7.2 (a)**, a dewetting region always exists. The molten material at this dewetting region moves outward due to thermocapillary; as a result, the thickness of the film is increased, and a bump forms at the rim. However, the flat-top square beam can minimize the dewetting region. **Figure 7.2 (c) and (d)** show the SEM images and the AFM measurement results. The SEM images clearly show the difference in the morphologies at the rim. The AFM results also confirm our observations of the SEM images. For the Gaussian beam, the difference in the thickness at the rim is ~80 nm; however, we cannot observe the difference in the thickness for the flat-top square beam. This difference is hugely advantageous for the future fabrication of flexible OLEDs, as surface smoothness is critical to the fabrication of electrodes.

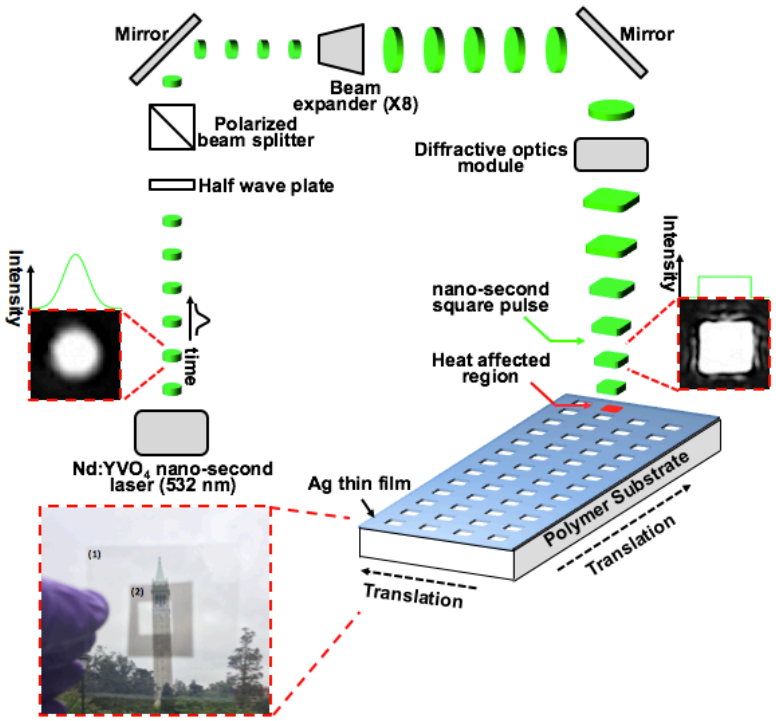

Figure 7.1 Fabrication schematics of Ag FTCEs. Optical image of the sather tower is to compare the transmittance.

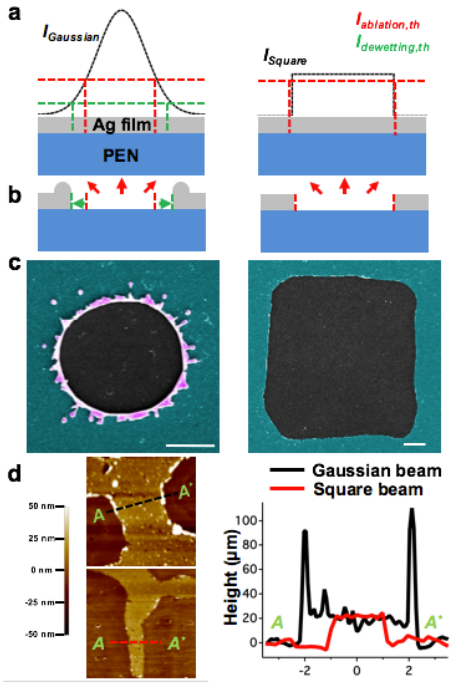

Figure 7.2 Schematic comparision of (a) laser beam profile (b) ablation and dewetting regions. (c) False color SEM images (scales?) and (d) AFM images of Gaussian beam processed and Square beam processed Ag FTCEs.

As shown in **Figure 7.2 (a)**, the laser beam intensity profiles of the Gaussian beam and the flat-top square beam are different. Thus, for the flat-top square beam, the temperature field inside the laser-irradiated spot is much different from that of the Gaussian beam, and the temperature gradient is much smaller for the flat-top square beam. Consequently, a thermocapillary mass transfer of molten Ag outward will be suppressed. In addition, below the laser ablation threshold for the flat-top square beam, dewetted molten Ag forms an island. As shown in **Figure 7.3**, the two regions are distinct based on the different slopes of the square beam. By extrapolating two linear lines, we can estimate the laser ablation threshold of the flat-top square beam. The laser ablation threshold of the Gaussian beam can be easily calculated using **Equation 5.1**.

Figure 7.4 (a) displays a plot of transmittance at 532 nm (T) compared to the sheet resistance (R_s) for Ag FTCEs. We can clearly observe the behavior of the percolative regime in 10-nm and 25-nm thick Ag film. These Ag FTCEs exhibited a superior optoelectrical performance of T = 85.1% and R_s = 130 Ω sq^{-1} when the Ag film thickness was 10 nm. These improvements in transmittance and in the characteristics of percolative regime operation are attributed to the beam shaping of the Gaussian beam profile to the flat-top square beam; thus, the areal density was reduced.

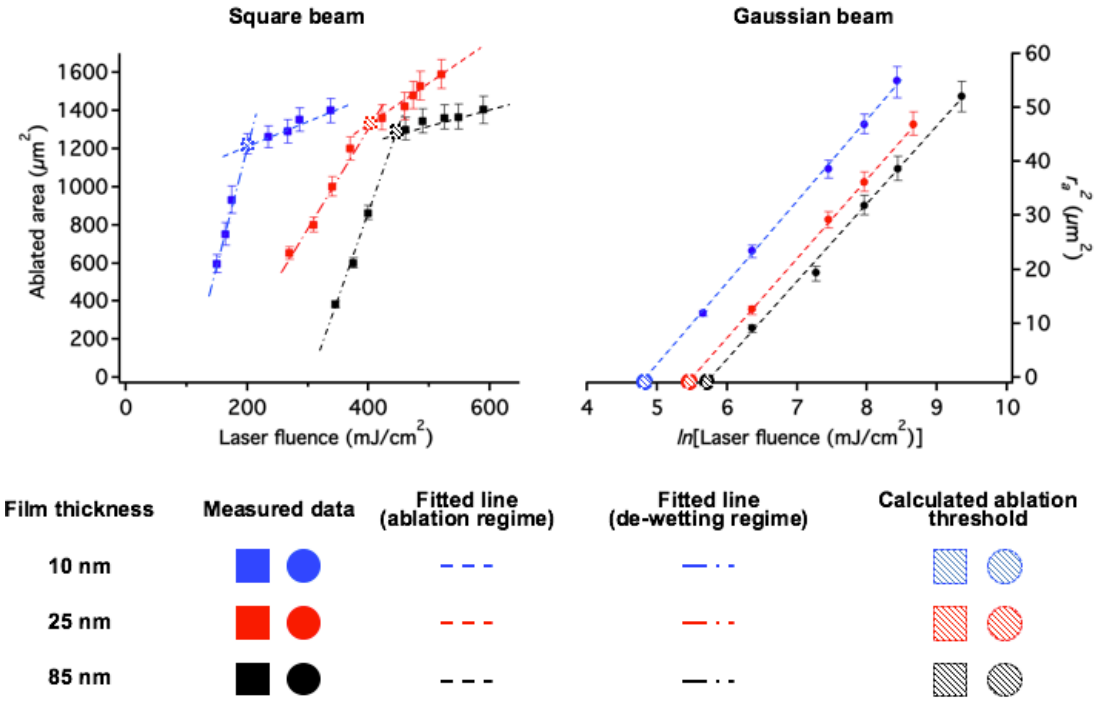

Figure 7.3 laser ablation thereshold of flat top square beam and Gaussian beam

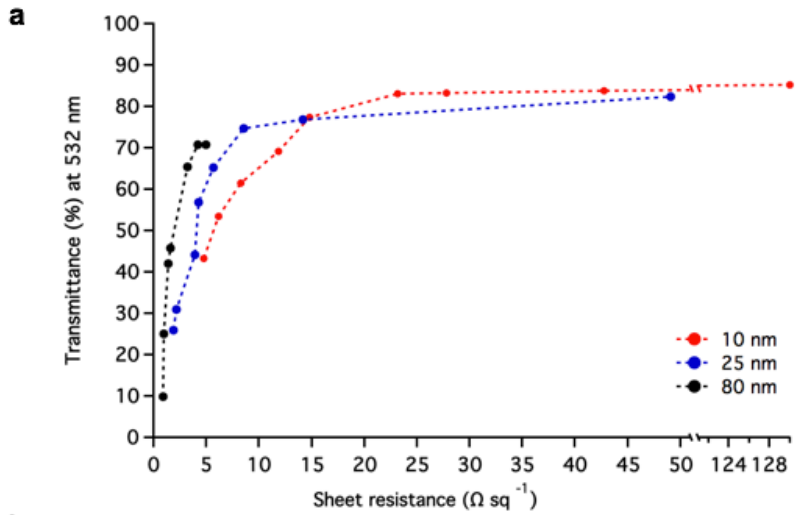

c

Thickness (nm)	Bulk FoM (Π_{bulk})	Percolative FoM ($\Pi_{percolative}$)	Percolation exponent (n)
10	81.1	16.5	3.7
25	116.4	16.3	3
80	210.4	-	

Figure 7.4 (a) Plot of sheet resistance versus transmittance at 532 nm wavelength of Ag FTCEs with different thickness. (b) Plot of Bulk FoM versus film thickness. (c) FoM at bulk and percolateive regime with 3 different thickness (10 nm, 25 nm, 80 nm)

7.2.2 Optical temperature measurement

We must still overcome several challenges in order to accurately control the laser–matter interaction. Among these challenges, the precise regulation of the time-transient temperature field is important for ultimately maximizing the electrical performance. To quantitatively understand the kinetics of the laser sintering, in principle we have to solve the following heat conduction equation:

Equation 7.1 Time transient heat conduction equation

$$\nabla\cdot(-k(T)\nabla(T(\xi,y,z,t))+(1-R(\lambda,T))\cdot I(\xi,y,t)\cdot\alpha(\lambda,T)\cdot e^{-\alpha(\lambda,T)z}=-\rho(T)c(T)\vec{v}\cdot\nabla(T(\xi,y,z,t))$$

where k, R, I, α, ρ, c, and v represent thermal conductivity, reflectivity, laser power density, the absorption coefficient, density, specific heat capacity, and velocity, respectively. All these parameters change drastically during sintering due to the phase change from dielectric to metallic as sintering progresses. In particular, thermal conductivity, reflectivity, and the absorption coefficient are very complex functions of temperature that drastically change during sintering. The thermal conductivity of pristine Ag NP thin film, as estimated by Maxwell-Garnett effective medium approximation, is 0.1-0.7 W/m•K, while the thermal conductivity of laser-sintered Ag

NP thin film, as estimated by W-F law, is ~130 W/m•K, which is three orders of magnitude higher than that of pristine Ag NP thin film. Furthermore, their optical properties, such as reflectivity and the absorption coefficient, also change drastically. Therefore, the analytical approach is not feasible.

To overcome these drawbacks, several direct measurement techniques are proposed. Among them is using an infrared camera or thermocouple, as shown in **Figure 7.5**. Since the size of the laser spot is so small, inserting thermocouples was not feasible. Infrared cameras have similar problems (i.e., limited spatial and temporal resolutions); more importantly, since we do not know the emissivity of the material, the accuracy of the measured temperature cannot be guaranteed.

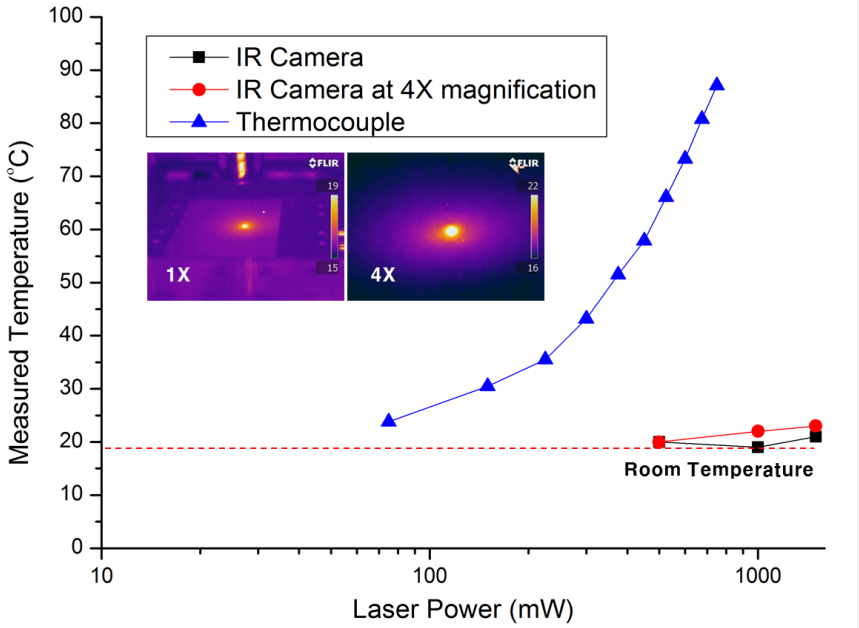

Figure 7.5 Temperature measurement results using IR camera (1 × and 4 × magnification) and thermocouple

Park et al[145] showed the temperature measurement schemes for pulsed laser-induced transient processes in their paper. They used an optical probing technique. By using 633 nm HeNe laser as a probe beam. They measured reflectivity change upon laser irradiation. In this optical temperature sensor, poly-crystalline silicon was used as a sensor.

References

1. Li, J.; Zhao, W.; Huang, F.; Manivannan, A.; Wu, N. *Nanoscale* **2011,** 3, (12), 5103-5109.
2. Dong, L.; Chu, Y.; Sun, W. *Chem. Eur. J.* **2008,** 14, (16), 5064-5072.
3. Su, D.; Kim, H. S.; Kim, W. S.; Wang, G. *Chem. Eur. J.* **2012,** 18, (26), 8224-8229.
4. Xia, X.; Tu, J.; Zhang, Y.; Wang, X.; Gu, C.; Zhao, X.-b.; Fan, H. J. *Acs Nano* **2012,** 6, (6), 5531-5538.
5. Ren, Y.; Gao, L. *J. Am. Ceram. Soc.* **2010,** 93, (11), 3560-3564.
6. Zhan, Y.; Yin, C.; Zheng, C.; Wang, W.; Wang, G. *J. Solid State Chem.* **2004,** 177, (7), 2281-2284.
7. Kumari, L.; Li, W.; Vannoy, C.; Leblanc, R.; Wang, D. *Cryst. Res. Technol.* **2009,** 44, (5), 495-499.
8. Lee, D.; Pan, H.; Ko, S. H.; Park, H. K.; Kim, E.; Grigoropoulos, C. P. *Appl. Phys. A* **2012,** 107, (1), 161-171.
9. Kang, B.; Han, S.; Kim, J.; Ko, S.; Yang, M. *J. Phys. Chem. C* **2011,** 115, (48), 23664-23670.
10. Joo, M.; Lee, B.; Jeong, S.; Lee, M. *Appl. Surf. Sci.* **2011,** 258, (1), 521-524.
11. Ryu, J.; Kim, H.-S.; Hahn, H. T. *J. Electron. Mater.* **2011,** 40, (1), 42-50.
12. Kim, H.-S.; Dhage, S. R.; Shim, D.-E.; Hahn, H. T. *Appl. Phys. A* **2009,** 97, (4), 791-798.
13. An, K.; Hong, S.; Han, S.; Lee, H.; Yeo, J.; Ko, S. H. *Acs Appl Mater Inter* **2014,** 6, (4), 2786-2790.
14. Hong, S.; Yeo, J.; Kim, G.; Kim, D.; Lee, H.; Kwon, J.; Lee, H.; Lee, P.; Ko, S. H. *Acs Nano* **2013,** 7, (6), 5204-5031.
15. Zenou, M.; Ermak, O.; Saar, A.; Kotler, Z. *Journal of Physics D: Applied Physics* **2014,** 47, (2), 025501.
16. Chung, J.; Bieri, N.; Ko, S.; Grigoropoulos, C.; Poulikakos, D. *Appl. Phys. A* **2004,** 79, (4-6), 1259-1261.
17. Lee, D.; Paeng, D.; Park, H. K.; Grigoropoulos, C. P. *Acs Nano* **2014**.
18. Buffat, P.; Borel, J. P. *Phys. Rev. A* **1976,** 13, (6), 2287-2298.
19. Kelly, K. L.; Coronado, E.; Zhao, L. L.; Schatz, G. C. *J. Phys. Chem. B* **2003,** 107, (3), 668-677.
20. Yeo, J.; Hong, S.; Lee, D.; Hotz, N.; Lee, M.-T.; Grigoropoulos, C. P.; Ko, S. H. *Plos One* **2012,** 7, (8), e42315.
21. Son, Y.; Yeo, J.; Moon, H.; Lim, T. W.; Hong, S.; Nam, K. H.; Yoo, S.; Grigoropoulos, C. P.; Yang, D.-Y.; Ko, S. H. *Adv. Mater.* **2011,** 23, (28), 3176-3181.
22. Shaheen, S. E.; Radspinner, R.; Peyghambarian, N.; Jabbour, G. E. *Appl. Phys. Lett.* **2001,** 79, (18), 2996-2998.
23. Pardo, D. A.; Jabbour, G. E.; Peyghambarian, N. *Adv. Mater.* **2000,** 12, (17), 1249-1252.
24. Ko, S. H.; Chung, J.; Hotz, N.; Nam, K. H.; Grigoropoulos, C. P. *Journal of Micromechanics and Microengineering* **2010,** 20, (12), 125010.
25. Ko, S. H.; Lee, D.; Hotz, N.; Yeo, J.; Hong, S.; Nam, K. H.; Grigoropoulos, C. P. *Langmuir* **2011,** 28, (10), 4787-4792.
26. Secor, E. B.; Prabhumirashi, P. L.; Puntambekar, K.; Geier, M. L.; Hersam, M. C. *The journal of physical chemistry letters* **2013,** 4, (8), 1347-1351.
27. Ko, S. H.; Park, I.; Pan, H.; Grigoropoulos, C. P.; Pisano, A. P.; Luscombe, C. K.; Fréchet, J. M. *Nano letters* **2007,** 7, (7), 1869-1877.

28. Lee, D.; Pan, H.; Sherry, A.; Ko, S. H.; Lee, M.-T.; Kim, E.; Grigoropoulos, C. P. *Nanotechnology* **2012,** 23, (34), 344012.
29. Maekawa, K.; Yamasaki, K.; Niizeki, T.; Mita, M.; Matsuba, Y.; Terada, N.; Saito, H. In *Laser sintering of silver nanoparticles for electronic use*, Materials Science Forum, 2010; Trans Tech Publ: pp 2085-2090.
30. Smith, B. L.; Hutchison, J. E. *The Journal of Physical Chemistry C* **2013,** 117, (47), 25127-25137.
31. Moon, K.-S.; Dong, H.; Maric, R.; Pothukuchi, S.; Hunt, A.; Li, Y.; Wong, C. *J. Electron. Mater.* **2005,** 34, (2), 168-175.
32. Carotenuto, G.; Marletta, G.; Nicolais, L. *Journal of materials science letters* **2001,** 20, (7), 663-665.
33. Volkman, S. K.; Yin, S.; Bakhishev, T.; Puntambekar, K.; Subramanian, V.; Toney, M. F. *Chemistry of Materials* **2011,** 23, (20), 4634-4640.
34. Kang, J.; Ryu, J.; Kim, H.; Hahn, H. *J. Electron. Mater.* **2011,** 40, (11), 2268-2277.
35. Warrier, P.; Yuan, Y.; Beck, M. P.; Teja, A. S. *AIChE Journal* **2010,** 56, (12), 3243-3256.
36. Warrier, P.; Teja, A. *Nanoscale research letters* **2011,** 6, (1), 247.
37. Putnam, S. A.; Cahill, D. G.; Braun, P. V.; Ge, Z.; Shimmin, R. G. *J. Appl. Phys.* **2006,** 99, (8), 084308.
38. Nan, C.-W.; Birringer, R.; Clarke, D. R.; Gleiter, H. *J. Appl. Phys.* **1997,** 81, (10), 6692-6699.
39. Chung, J.; Han, S.; Lee, D.; Ahn, S.; Grigoropoulos, C. P.; Moon, J.; Ko, S. H. *Optical Engineering* **2013,** 52, (2), 024302-024302.
40. Eastman, J. A.; Phillpot, S.; Choi, S.; Keblinski, P. *Annu. Rev. Mater. Res.* **2004,** 34, 219-246.
41. Choi, J. H.; Ryu, K.; Park, K.; Moon, S.-J. *Int J Heat Mass Tran* **2015,** 85, 904-909.
42. de Vries, A. J.; Kooij, E. S.; Wormeester, H.; Mewe, A. A.; Poelsema, B. *J. Appl. Phys.* **2007,** 101, (5), 053703.
43. Kooij, E. S.; Poelsema, B. *Physical Chemistry Chemical Physics* **2006,** 8, (28), 3349-3357.
44. Wormeester, H.; Henry, A.-I.; Kooij, E. S.; Poelsema, B.; Pileni, M.-P. *The Journal of chemical physics* **2006,** 124, (20), 204713.
45. Little, S.; Collins, R.; Marsillac, S. *Appl. Phys. Lett.* **2011,** 98, (10), 101910.
46. Fox, A. M.; Fox, M., *Optical properties of solids*. Oxford university press New York: 2001; Vol. 2010.
47. Heavens, O. S., *Optical properties of thin solid films*. Courier Corporation: 1991.
48. Grigoropoulos, C. P., *Transport in laser microfabrication: fundamentals and applications*. Cambridge University Press: 2009.
49. Magdassi, S.; Grouchko, M.; Berezin, O.; Kamyshny, A. *Acs Nano* **2010,** 4, (4), 1943-1948.
50. Pan, H.; Ko, S. H.; Grigoropoulos, C. P. *Journal of Heat Transfer* **2008,** 130, (9), 092404.
51. Brueck, S.; Ehrlich, D. *Physical Review Letters* **1982,** 48, (24), 1678.
52. Liu, C. S.; Tripathi, V. K. *Quantum Electronics, IEEE Journal of* **1998,** 34, (8), 1503-1507.
53. Mayadas, A.; Shatzkes, M. *Phys. Rev. B* **1970,** 1, (4), 1382.
54. Bäuerle, D., *Laser processing and chemistry*. Springer: 2000; Vol. 3.
55. Greer, J. R.; Street, R. A. *Acta Materialia* **2007,** 55, (18), 6345-6349.

56. Ko, S. H.; Grigoropoulos, C. P. *Journal of Heat Transfer* **2008,** 130, 092404-1.
57. Luo, L.-B.; Yu, S.-H.; Qian, H.-S.; Zhou, T. *J. Am. Chem. Soc.* **2005,** 127, (9), 2822-2823.
58. Link, S.; Burda, C.; Nikoobakht, B.; El-Sayed, M. A. *Chemical Physics Letters* **1999,** 315, (1–2), 12-18.
59. Plech, A.; Kotaidis, V.; Lorenc, M.; Wulff, M. *Chemical Physics Letters* **2005,** 401, (4–6), 565-569.
60. Inasawa, S.; Sugiyama, M.; Noda, S.; Yamaguchi, Y. *J. Phys. Chem. B* **2006,** 110, (7), 3114-3119.
61. Stellacci, F.; Bauer, C. A.; Meyer-Friedrichsen, T.; Wenseleers, W.; Alain, V.; Kuebler, S. M.; Pond, S. J. K.; Zhang, Y.; Marder, S. R.; Perry, J. W. *Adv. Mater.* **2002,** 14, (3), 194-198.
62. Abargues, R.; Marques-Hueso, J.; Canet-Ferrer, J.; Pedrueza, E.; Valdes, J. L.; Jimenez, E.; Martinez-Pastor, J. P. *Nanotechnology* **2008,** 19, (35).
63. Lee, M.-T.; Lee, D.; Sherry, A.; Grigoropoulos, C. P. *Journal of Micromechanics and Microengineering* **2011,** 21, (9), 095018.
64. Dongjo, K.; Sunho, J.; Jooho, M. *Nanotechnology* **2006,** 17, (16), 4019.
65. Zidan, H. M. *Polym Test* **1999,** 18, (6), 449-461.
66. Wuithschick, M.; Paul, B.; Bienert, R.; Sarfraz, A.; Vainio, U.; Sztucki, M.; Kraehnert, R.; Strasser, P.; Rademann, K.; Emmerling, F. *Chemistry of Materials* **2013**.
67. Lim, T. H.; McCarthy, D.; Hendy, S. C.; Stevens, K. J.; Brown, S. A.; Tilley, R. D. *Acs Nano* **2009,** 3, (11), 3809-3813.
68. Wu, J.; Cao, J.; Han, W.-Q.; Janotti, A.; Kim, H.-C., *Functional metal oxide nanostructures*. Springer: 2012.
69. Pan, Z. W.; Dai, Z. R.; Wang, Z. L. *Science* **2001,** 291, (5510), 1947-1949.
70. Fergus, J. W. *J. Eur. Ceram. Soc.* **2012,** 32, (3), 525-540.
71. Wei, T. Y.; Chen, C. H.; Chien, H. C.; Lu, S. Y.; Hu, C. C. *Adv. Mater.* **2010,** 22, (3), 347-351.
72. Wang, D.-W.; Li, F.; Cheng, H.-M. *J. Power Sources* **2008,** 185, (2), 1563-1568.
73. Fominykh, K.; Feckl, J. M.; Sicklinger, J.; Döblinger, M.; Böcklein, S.; Ziegler, J.; Peter, L.; Rathousky, J.; Scheidt, E.-W.; Bein, T.; Fattakhova-Rohlfing, D. *Adv. Funct. Mater.* **2014,** 24, (21), 3123-3129.
74. Zhang, F.-b.; Zhou, Y.-k.; Li, H.-l. *Mater. Chem. Phys.* **2004,** 83, (2), 260-264.
75. Liu, B.; Yang, H.; Zhao, H.; An, L.; Zhang, L.; Shi, R.; Wang, L.; Bao, L.; Chen, Y. *Sens. Actuators, B* **2011,** 156, (1), 251-262.
76. Wang, X.; Yang, Z.; Sun, X.; Li, X.; Wang, D.; Wang, P.; He, D. *J. Mater. Chem.* **2011,** 21, (27), 9988-9990.
77. Zhao, B.; Ke, X.-K.; Bao, J.-H.; Wang, C.-L.; Dong, L.; Chen, Y.-W.; Chen, H.-L. *J. Phys. Chem. C* **2009,** 113, (32), 14440-14447.
78. Kim, T. W.; Hwang, S. J.; Jhung, S. H.; Chang, J. S.; Park, H.; Choi, W.; Choy, J.-H. *Adv. Mater.* **2008,** 20, (3), 539-542.
79. Gillaspie, D. T.; Tenent, R. C.; Dillon, A. C. *J. Mater. Chem.* **2010,** 20, (43), 9585-9592.
80. Svensson, J.; Granqvist, C. *Appl. Phys. Lett.* **1986,** 49, (23), 1566-1568.
81. Yuan, Y.; Xia, X.; Wu, J.; Chen, Y.; Yang, J.; Guo, S. *Electrochim. Acta* **2011,** 56, (3), 1208-1212.
82. Ohta, H.; Hirano, M.; Nakahara, K.; Maruta, H.; Tanabe, T.; Kamiya, M.; Kamiya, T.; Hosono, H. *Appl. Phys. Lett.* **2003,** 83, (5), 1029-1031.

83. Seo, S.; Lee, M.; Seo, D.; Jeoung, E.; Suh, D.-S.; Joung, Y.; Yoo, I.; Hwang, I.; Kim, S.; Byun, I. *Appl. Phys. Lett.* **2004,** 85, (23), 5655-5657.
84. Hotovy, I.; Huran, J.; Spiess, L.; Hascik, S.; Rehacek, V. *Sens. Actuators, B* **1999,** 57, (1), 147-152.
85. Hotovy, I.; Rehacek, V.; Siciliano, P.; Capone, S.; Spiess, L. *Thin Solid Films* **2002,** 418, (1), 9-15.
86. Hoa, N. D.; El‐Safty, S. A. *Chem. Eur. J.* **2011,** 17, (46), 12896-12901.
87. Sun, J.; Jing, Y.; Jia, Y.; Tillard, M.; Belin, C. *Mater. Lett.* **2005,** 59, (29), 3933-3936.
88. Cho, M.; Choi, W.; Kim, S.; Kim, I.; Lee, Y. *J. Nanosci. Nanotechno.* **2010,** 10, (10), 6888-6891.
89. Park, S.-H.; Kim, H.-S. *Thin Solid Films* **2014,** 550, 575-581.
90. Jeangros, Q.; Hansen, T. W.; Wagner, J. B.; Damsgaard, C. D.; Dunin-Borkowski, R. E.; Hébert, C.; Hessler-Wyser, A. *J. Mater. Sci.* **2013,** 48, (7), 2893-2907.
91. Richardson, J. T.; Scates, R.; Twigg, M. V. *Appl. Catal., A* **2003,** 246, (1), 137-150.
92. Rodriguez, J. A.; Hanson, J. C.; Frenkel, A. I.; Kim, J. Y.; Pérez, M. *J. Am. Chem. Soc.* **2002,** 124, (2), 346-354.
93. Wood, D.; Tauc, J. *Phys. Rev. B* **1972,** 5, (8), 3144.
94. Hüfner, S. *Adv. Phys.* **1994,** 43, (2), 183-356.
95. Patil, P.; Kadam, L. *Appl. Surf. Sci.* **2002,** 199, (1), 211-221.
96. Ansari, S. A.; Khan, M. M.; Kalathil, S.; Khan, A. N.; Lee, J.; Cho, M. H. *Nanoscale* **2013**.
97. Fan, H.; Ramdas, A. *J. Appl. Phys.* **1959,** 30, (8), 1127-1134.
98. Gandhi, A. C.; Pant, J.; Pandit, S. D.; Dalimbkar, S. K.; Chan, T.-S.; Cheng, C.-L.; Ma, Y.-R.; Wu, S. Y. *J. Phys. Chem. C* **2013,** 117, (36), 18666-18674.
99. Duan, W.; Lu, S.; Wu, Z.; Wang, Y. *J. Phys. Chem. C* **2012,** 116, (49), 26043-26051.
100. Kremenovic, A.; Antic, B.; Vucinic-Vasic, M.; Colomban, P.; Jovalekic, C.; Bibic, N.; Kahlenberg, V.; Leoni, M. *J. Appl. Crystallogr.* **2010,** 43, (4), 699-709.
101. Hulst, H. C.; Van De Hulst, H., *Light scattering by small particles*. Courier Dover Publications: 1957.
102. Gomez De Arco, L.; Zhang, Y.; Schlenker, C. W.; Ryu, K.; Thompson, M. E.; Zhou, C. *Acs Nano* **2010,** 4, (5), 2865-2873.
103. Ho, Y.-H.; Chen, K.-Y.; Liu, S.-W.; Chang, Y.-T.; Huang, D.-W.; Wei, P.-K. *Org Electron* **2011,** 12, (6), 961-965.
104. Yu, Z.; Zhang, Q.; Li, L.; Chen, Q.; Niu, X.; Liu, J.; Pei, Q. *Adv. Mater.* **2011,** 23, (5), 664-668.
105. Hecht, D. S.; Hu, L.; Irvin, G. *Adv. Mater.* **2011,** 23, (13), 1482-1513.
106. Rathmell, A. R.; Bergin, S. M.; Hua, Y. L.; Li, Z. Y.; Wiley, B. J. *Adv. Mater.* **2010,** 22, (32), 3558-3563.
107. Zhang, D.; Ryu, K.; Liu, X.; Polikarpov, E.; Ly, J.; Tompson, M. E.; Zhou, C. *Nano letters* **2006,** 6, (9), 1880-1886.
108. Hu, L.; Hecht, D.; Grüner, G. *Nano letters* **2004,** 4, (12), 2513-2517.
109. Eda, G.; Fanchini, G.; Chhowalla, M. *Nat Nanotechnol* **2008,** 3, (5), 270-274.
110. Kim, K. S.; Zhao, Y.; Jang, H.; Lee, S. Y.; Kim, J. M.; Kim, K. S.; Ahn, J.-H.; Kim, P.; Choi, J.-Y.; Hong, B. H. *Nature* **2009,** 457, (7230), 706-710.

111. Girtan, M.; Vlad, A.; Mallet, R.; Bodea, M.; Pedarnig, J.; Stanculescu, A.; Mardare, D.; Leontie, L.; Antohe, S. *Appl. Surf. Sci.* **2013,** 274, 306-313.
112. Kevin, M.; Tho, W. H.; Ho, G. W. *J. Mater. Chem.* **2012,** 22, (32), 16442-16447.
113. Hagendorfer, H.; Lienau, K.; Nishiwaki, S.; Fella, C. M.; Kranz, L.; Uhl, A. R.; Jaeger, D.; Luo, L.; Gretener, C.; Buecheler, S. *Adv. Mater.* **2014,** 26, (4), 632-636.
114. Lee, J.-Y.; Connor, S. T.; Cui, Y.; Peumans, P. *Nano letters* **2008,** 8, (2), 689-692.
115. Ye, S.; Rathmell, A. R.; Stewart, I. E.; Ha, Y.-C.; Wilson, A. R.; Chen, Z.; Wiley, B. J. *Chem Commun* **2014,** 50, (20), 2562-2564.
116. Catrysse, P. B.; Fan, S. *Nano letters* **2010,** 10, (8), 2944-9.
117. Lee, M.-S.; Lee, K.; Kim, S.-Y.; Lee, H.; Park, J.; Choi, K.-H.; Kim, H.-K.; Kim, D.-G.; Lee, D.-Y.; Nam, S.; Park, J.-U. *Nano letters* **2013,** 13, (6), 2814-2821.
118. Ye, S.; Rathmell, A. R.; Chen, Z.; Stewart, I. E.; Wiley, B. J. *Adv. Mater.* **2014,** 26, (39), 6670-6687.
119. Song, M.; You, D. S.; Lim, K.; Park, S.; Jung, S.; Kim, C. S.; Kim, D. H.; Kim, D. G.; Kim, J. K.; Park, J. *Adv. Funct. Mater.* **2013,** 23, (34), 4177-4184.
120. Song, J.; Li, J.; Xu, J.; Zeng, H. *Nano letters* **2014**.
121. Kwon, N.; Kim, K.; Sung, S.; Yi, I.; Chung, I. *Nanotechnology* **2013,** 24, (23), 235205.
122. Matthias, E.; Reichling, M.; Siegel, J.; Käding, O.; Petzoldt, S.; Skurk, H.; Bizenberger, P.; Neske, E. *Appl. Phys. A* **1994,** 58, (2), 129-136.
123. De, S.; King, P. J.; Lyons, P. E.; Khan, U.; Coleman, J. N. *Acs Nano* **2010,** 4, (12), 7064-7072.
124. Park, S. I.; Ahn, J. H.; Feng, X.; Wang, S.; Huang, Y.; Rogers, J. A. *Adv. Funct. Mater.* **2008,** 18, (18), 2673-2684.
125. Schuller, J. A.; Barnard, E. S.; Cai, W.; Jun, Y. C.; White, J. S.; Brongersma, M. L. *Nature materials* **2010,** 9, (3), 193-204.
126. Chang, C.-C.; Sharma, Y. D.; Kim, Y.-S.; Bur, J. A.; Shenoi, R. V.; Krishna, S.; Huang, D.; Lin, S.-Y. *Nano letters* **2010,** 10, (5), 1704-1709.
127. Genet, C.; Ebbesen, T. *Nature* **2007,** 445, (7123), 39-46.
128. Wang, A.; Jiang, L.; Li, X.; Liu, Y.; Dong, X.; Qu, L.; Duan, X.; Lu, Y. *Adv. Mater.* **2015,** 27, (40), 6238-6243.
129. Siegel, J.; Puerto, D.; Gawelda, W.; Bachelier, G.; Solís Céspedes, J.; Ehrentraut, L.; Bonse, J. **2007**.
130. Qi, D.; Liu, H.; Gao, W.; Chen, S.; Li, C.; Lai, H.; Huang, W.; Li, J. *Optics express* **2013,** 21, (8), 9923-9930.
131. Hwang, D. J.; Jeon, H.; Grigoropoulos, C. P.; Yoo, J.; Russo, R. E. *Appl. Phys. Lett.* **2007,** 91, (25), 251118.
132. Paeng, D.; Lee, D.; Yeo, J.; Yoo, J.-H.; Allen, F. I.; Kim, E.; So, H.; Park, H. K.; Minor, A. M.; Grigoropoulos, C. P. *The Journal of Physical Chemistry C* **2015,** 119, (11), 6363-6372.
133. Paeng, D.; Lee, D.; Grigoropoulos, C. P. *Appl. Phys. Lett.* **2014,** 105, (7), 073110.
134. Yoo, J. H.; Jeong, S.; Greif, R.; Russo, R. *J. Appl. Phys.* **2000,** 88, (3), 1638-1649.
135. De Giacomo, A.; Dell'Aglio, M.; Santagata, A.; Gaudiuso, R.; De Pascale, O.; Wagener, P.; Messina, G.; Compagnini, G.; Barcikowski, S. *Physical Chemistry Chemical Physics* **2013,** 15, (9), 3083-3092.
136. Papazoglou, D.; Karaiskou, A.; Zergioti, I.; Fotakis, C. *Appl. Phys. Lett.* **2002,** 81, (9), 1594-1596.
137. Porneala, C.; Willis, D. A. *Appl. Phys. Lett.* **2006,** 89, (21), 211121.

138. Redmond, P. L.; Hallock, A. J.; Brus, L. E. *Nano letters* **2005,** 5, (1), 131-135.
139. Wu, Y.; Fowlkes, J. D.; Rack, P. D. *J Mater Res* **2011,** 26, (02), 277-287.
140. Kulchin, Y. N.; Vitrik, O.; Kuchmizhak, A.; Emel'yanov, V.; Ionin, A.; Kudryashov, S.; Makarov, S. *Phys. Rev. E* **2014,** 90, (2), 023017.
141. Hergenröder, R. *Spectrochimica Acta Part B: Atomic Spectroscopy* **2006,** 61, (3), 284-300.
142. Egry, I.; Ricci, E.; Novakovic, R.; Ozawa, S. *Advances in colloid and interface science* **2010,** 159, (2), 198-212.
143. Tsibidis, G. D.; Barberoglou, M.; Loukakos, P. A.; Stratakis, E.; Fotakis, C. *Phys. Rev. B* **2012,** 86, (11), 115316.
144. Mazumder, J. *Optical engineering* **1991,** 30, (8), 1208-1219.
145. Park, H.; Poon, C.; Tam, A.; Zhang, X.; Grigoropoulos, C. *Journal of heat transfer* **1996,** 118, (3), 702-708.